Charge and exciton transport in organic semiconductors

Charge and exciton transport in organic semiconductors: The role of molecular vibrations

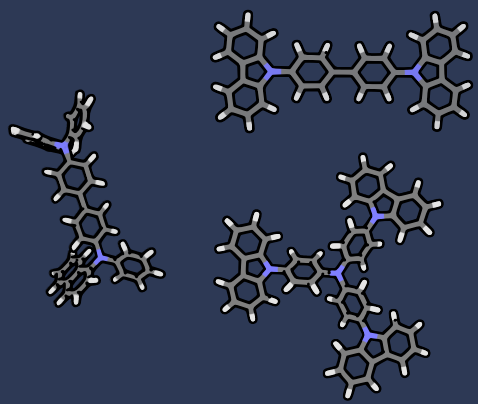

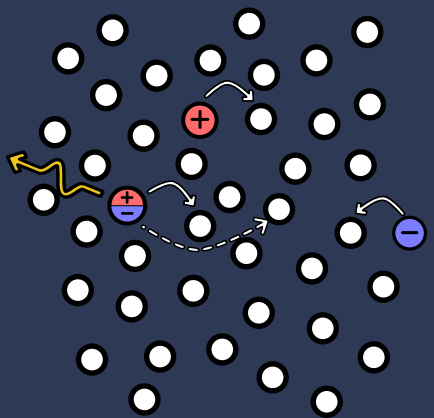

Xander de Vries

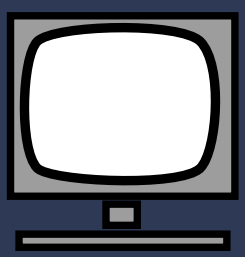

Charge and exciton transport in organic semiconductors: The role of molecular vibrations

PROEFSCHRIFT

ter verkrijging van de graad van doctor aan de Technische Universiteit Eindhoven, op gezag van de rector magnificus prof.dr.ir. F.P.T. Baaijens, voor een commissie aangewezen door het College voor Promoties, in het openbaar te verdedigen op donderdag 18 september 2019 om 11:00 uur

door

Xander de Vries

geboren te Tilburg

Dit is goedgekeurd door de promotoren en de samenstelling van de promotiecommissie is als volgt:

voorzitter:	prof.dr.ir. G.M.W. Kroesen
1e promotor:	prof.dr. P.A. Bobbert
2e promotor:	prof.dr. R. Coehoorn
leden:	prof.dr. A.B. Walker (University of Bath)
	prof.dr. J. Gómez Rivas
	dr.ir. S.J.J.M.F. Kokkelmans
	Prof.Dr. W. Wenzel (Karlsruhe Institute of Technology)

Het onderzoek of ontwerp dat in dit proefschrift wordt beschreven is uitgevoerd in overeenstemming met de TU/e Gedragscode Wetenschapsbeoefening.

Charge and exciton transport in organic semiconductors: The role of molecular vibrations

Xander de Vries

"Study hard what interests you the most in the most undisciplined, irreverent and original manner possible."

- Richard Feynmann

A catalogue record is available from the Eindhoven
University of Technology Library
ISBN: 978-90-386-4851-4

Contents

1 Introduction **1**
1.1 Organic electronics . . . 2
1.1.1 Applications . . . 3
1.2 OLEDs . . . 3
1.2.1 Working princple . . . 3
1.2.2 Light emission . . . 4
1.3 Computational modelling of OLEDs . . . 6
1.3.1 Hopping transport . . . 6
1.3.2 Computational modelling . . . 7
1.4 Theory of charge and exciton transfer . . . 9
1.4.1 Marcus theory . . . 10
1.4.2 Miller-Abrahams theory . . . 11
1.4.3 Marcus-Levich-Jortner theory . . . 11
1.4.4 Franck-Condon weighted density of states . . . 12
1.4.5 Charge transfer integrals . . . 12
1.4.6 Förster transfer . . . 13
1.4.7 Dexter transfer . . . 14
1.4.8 Fermi's Golden Rule . . . 14
1.5 Modelling transport in organic semiconductors . . . 15
1.5.1 Modelling charge transport . . . 15
1.5.2 Modelling exciton transport . . . 16
1.6 OLED device models . . . 17
1.7 Scope of this thesis . . . 17

2 Computational methods **27**
2.1 Introduction . . . 28
2.2 First-principles methods . . . 28
2.2.1 Transfer integrals . . . 29
1) Charge transfer integrals . . . 29
2) Exciton transfer integrals . . . 29
3) Transfer integrals for multiple acceptor states . . . 31
2.2.2 Reorganization energy and vibronic couplings . . . 31
1) Reorganization energy . . . 31

2) Vibronic couplings . . . 32
2.3 Calculation of the transfer rate . . . 33
2.4 Simulating the disorder . . . 37
2.4.1 Spatial disorder . . . 37
1) Dominance competition point placement . . . 38
2) Disordered lattice Monte Carlo . . . 39
2.4.2 Transfer integral disorder . . . 41
2.4.3 Energetic disorder . . . 41
2.5 Transport simulations . . . 42
2.5.1 Charge transport . . . 42
2.5.2 Exciton transport . . . 44

3 Full quantum treatment of charge dynamics in amorphous molecular semiconductors 47
3.1 Introduction . . . 48
3.2 Full quantum charge transfer rate . . . 49
3.3 Electron and hole transfer rates: Application to α-NPD, TCTA, and spiro-DPVBi . . . 51
3.4 Mobilities and energetic relaxation of electrons and holes: Application to α-NPD, TCTA, and spiro-DPVBi . . . 54
3.5 Summary and conclusion . . . 55
Appendix . . . 57
A.1 Relation and comparison to the Marcus-Levich-Jortner rate . . . 57
A.2 Calculation of the vibron energies and coupling in embedded environments . . . 59
A.3 Influence of λ_{cl} on charge transfer rates and mobilities . . . 62

4 Triplet exciton diffusion in metal-organic phosphorescent host-guest systems 67
4.1 Introduction . . . 68
4.2 Theoretical methods . . . 71
4.2.1 Triplet transfer integrals . . . 71
4.2.2 Vibronic coupling . . . 72
4.2.3 Calculation of the morphology and energetic disorder . . . 74
4.2.4 Transition dipole moments and lifetimes . . . 75
4.2.5 Calculation of the diffusion length . . . 77
4.3 Results . . . 77
4.3.1 Transfer integrals . . . 77
4.3.2 Vibronic coupling and energy dependence of the transfer rate . . . 80
4.3.3 Förster radius . . . 83
4.3.4 Dexter rate . . . 84
4.4 Diffusion length − concentration and temperature dependence . . . 85
4.4.1 KMC simulations for a realistic morphology . . . 85

4.4.2 Diffusion on a simple cubic lattice . . . 88
4.5 Summary and conclusion . . . 89
Appendix . . . 91
A.1 Morphology expansion . . . 91
A.2 Triplet energies and energetic disorder . . . 95
A.3 Dexter transfer integrals for 10 mol% emitters in CBP and TCTA 96
A.4 Triplet wave functions . . . 97
A.5 Energy dependence of the triplet transfer rate at 150 K . . . 99
A.6 Diffusion length – 10 mol% emitters in TCTA . . . 100

5 Exciton transfer between metal-organic phosphorescent dyes 109
5.1 Introduction . . . 110
5.2 Theoretical method . . . 113
5.2.1 Förster transfer rate . . . 113
5.2.2 DFT calculations . . . 115
5.2.3 Vibronic coupling . . . 115
5.2.4 Excited state energies and transition dipole spectra . . . 116
5.3 Results . . . 118
5.3.1 Triplet energies and lifetimes . . . 118
5.3.2 Förster radii . . . 118
5.4 Summary and outlook . . . 125
Appendix . . . 126
A.1 Calculation of vibronic couplings . . . 126
A.2 Donor and acceptor spectra . . . 127
A.3 Numerical and graphical Förster radii overview . . . 127
A.4 The effect of energetic disorder . . . 129

6 Conclusions and Outlook 137
6.1 Main conclusions . . . 138
6.2 Outlook . . . 139
6.2.1 Host-guest charge transfer and exciton formation . . . 139
6.2.2 Exciton polaron quenching . . . 143
1) Device physics . . . 143
2) Exciton polaron quenching rate . . . 143

List of publications 148

Summary 149

Curriculum Vitae 151

Dankwoord 153

Chapter 1

Introduction

In this chapter we will introduce the scope of this thesis, which aims at improving our ability of predictively modelling the functioning of organic opto-electronic devices. For that purpose we will first introduce the organic material classes used for different devices. Then we look at the functioning of organic light emitting diodes (OLEDs) with specific focus on light generation in these devices. We introduce the multi-scale modelling approach for simulating the device physics, and highlight the role of transfer theories in the modelling. This brings us at the end of this chapter to the aim of this thesis, namely to incorporate all the important molecular properties correctly in the transfer equation in order to predictively model the physics in organic opto-electronic devices.

1.1 Organic electronics

The main promise of using organic materials in opto-electronic devices is the ability to almost limitlessly adapt the molecular and device structure, leading to enhanced and even novel device functionality. For realizing such ambitious goals, the development of predictive models, starting from first-principle theories, is essential: it is simply impossible to experimentally test all molecules and their combinations in devices. So far, models have relied upon transfer theories which include the vibrational and excited state properties of the molecules in a simplified way. In this thesis, we take the field of predictive modelling further by including many more of the molecular details in the transfer theories, enabling predictive modelling of charge and exciton transfer. Before we fully explain the scope of this thesis we first introduce the various classes of organic materials (section 1.1) and introduce organic light emitting diodes (OLEDs) specifically (section 1.2). We then explain the computational modelling of organic electronics (section 1.3) starting with the fundamental transfer theories (section 1.4). Then we discuss how these transfer theories are applied in the work on charge and exciton transport modelling of organic devices (section 1.5 and 1.6). Finally, we explain the scope of the thesis (section 1.7).

Organic materials are a class of materials mostly made up out of carbon and hydrogen atoms with in some cases a few other atoms like nitrogen, oxygen or sulfur. The electronic properties that these materials can exhibit are, for example, absorption and emission of light and conduction of electrons and holes. The organic materials that show these properties are also called organic semiconductors. The organic conducting materials can be roughly divided into three groups:

(i) **Amorphous molecular materials**. These consist of small organic molecules evaporated or spin-coated onto a substrate. They show little to no structural order. They can be deposited in a layer by layer fashion which is well suited for the fabrication of OLEDs. Therefore, most OLED devices are made from amorphous molecular materials.

(ii) **Molecular crystals**. These also consist of small molecules, but have significant order. The order is imposed by van-der-Waals interactions. The charge mobilities in these materials are often higher than in the amorphous materials. Therefore, these materials have potential in the field of Organic Field Effect Transistors (OFETs), where high charge mobilities are desired.

(iii) **Polymers**. Polymers consist of a chain of covalently bonded molecular repeat units. They can be processed from solution, which allows for potentially cheaper manufacturing methods like spin-coating, ink-jet printing or industrial roll-to-roll manufacturing. Potential electronic application for these materials are Organic PhotoVoltaic (OPV) devices and Polymer Light Emitting Diodes (PLEDs).

In this thesis we focus on the amorphous molecular materials for OLED applications. However, many of the theories and models studied in this work will also be applicable to molecular crystals and polymer systems.

1.1.1 Applications

In the last few years, organic electronic components have been introduced into smartphones and televisions. Due to the superior contrast ratio and instantaneous response of organic light emitting diodes (OLEDs), the market for these devices is developing rapidly. OLED displays can for example be found in the Galaxy smartphone series of Samsung. OLED-based lighting panels, aimed at the designer market, are produced by Osram. This is a realization of a promise of more than 60 years. Studies of conductivity and electroluminescence of organic solids were already done in the 1950s and 1960s [10, 3, 41]. The field has developed holding promise for OFETs, OPV and OLEDs. This development would be impossible without an understanding of the basic device physics, starting with charge and exciton transport.

1.2 OLEDs

1.2.1 Working princple

In an OLED, one or multiple organic layers are sandwiched between two electrodes. The OLED often consists of an electron transport layer (ETL), a hole transport layer (HTL) and an emissive layer (EML). In general, the HTL and ETL consist of a single organic material while the EML is a blend of a host material that conducts the electrons and holes and a guest material that emits the light. The electrons and holes flow from the ETL/HTL to the EML, where they meet to form excitons. The excitons are either formed on the emissive material in the EML or are transfered to the emissive material. This means that the energy levels of the host and guest in the EML need to be chosen in such way that the excitons are efficiently transfered to the guest material. More elaborate OLED architectures involving multiple emissive layers, often with different colors, are also possible. Additionally, often electron, hole or exciton blocking layers are used to make sure that the carriers are efficiently confined to the EML, ensuring that they recombine.

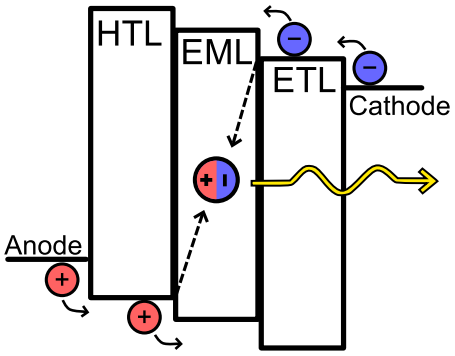

Figure 1.1: Schematic depiction of the working principle of a basic OLED. The holes flow from the HTL to the EML and the electrons from the ETL to the EML. In the EML the electrons and holes recombine to form excitons, which then radiatively decay to emit light.

1.2.2 Light emission

The electrons and holes that recombine in the EML can form eigher singlet or triplet excitons. Due to the spin statistics, 3 out of 4 exciton formations will result in a triplet exciton and 1 out of 4 in a singlet exciton. Unfortunately, the triplet excitons are non-emissive on most organic emitter molecules because the transition to the ground state, which has a singlet spin character, is optically forbidden. In the first generation of OLEDs, this "triplet loss" was taken for granted, which meant that the maximum quantum efficiency of OLEDs was around 25% [56].

In the second generation of OLEDs, depicted in Fig 1.2, the concept of *triplet harvesting* was introduced [6]. OLEDs with phosphorescent emitter molecules were used, which allowed the triplets to emit light and therefore achieved internal quantum efficiencies (IQE) of 100 % [1, 28]. The phosphorescent emitters are metal-organic molecules, which have a heavy metal atom incorporated in the core of the molecule. The heavy metal atom has strong spin-orbit coupling, which mixes the singlet and triplet states sufficiently to allow a radiative transition of the excited triplet state to the singlet ground state. Still, emission is not as fast in these phosphorescent emitters ($\sim \mu$s) as in the fluorescent molecules used in the first generation ($\sim$1 ns). The long exciton lifetimes poses certain challenges. Due to the strong spin orbit coupling all 25% singlets generated in the device are rapidly turned into triplets via Intersystem Crossing (ISC). This means that the device is now filled with triplets that are relatively long-lived. Within their radiative lifetime they can diffuse through the device and take part in different quenching processes. The most common of these processes are triplet polaron quenching (TPQ) and triplet-triplet annihilation (TTA). These processes reduce the device efficiency at high luminance levels, when the

exciton, hole and electron densities in the device becomes large. This effect is called the *roll-off*. Additionally, quenching events like TTA and TPQ are also believed to be involved in the degradation of OLEDs. As the molecules are energetically highly excited during TTA and TPQ events, the molecular bonds are prone to breaking, which can lead to non-emissive molecules or even trap sites for carriers. Preventing roll-off and device degradation due to quenching is one of the major challenges for the OLED field today. Another challenge regarding phosphorescent emitters is finding blue phosphorescent molecules that are stable enough for device application. Because of this, fluorescent molecules are still used for blue emission. In recent years some potential blue phosphorescent molecules have been discovered [32, 23]. However, the research into thermally activated delayed fluorescence, a concept which will be discussed next, has reduced the significance of those discoveries.

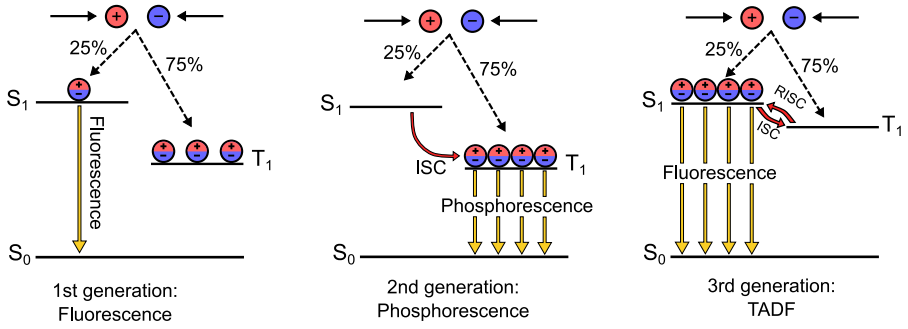

Figure 1.2: In this figure, the three generations of OLED emitters are depicted. In the first generation, fluorescent emitters were used. In the second generation, phosphorescent emitters were introduced in order to use the triplets generated in the device to emit light, a process called *triplet harvesting*. In the third generation, thermally activated delayed fluorescence is used. In this process, triplets are promoted to singlets, which can radiatively decay.

In the last few years in OLED research, there is an increased interest in thermally activated delayed fluorescence (TADF). The principle of TADF is depicted in Fig. 1.2. TADF OLEDs are sometimes also called the third generation of OLEDs, and provide a different way of triplet harvesting. The idea of TADF is to engineer the emitter molecule in such a way that the energy difference between the singlet and triplet excited states becomes very small. This is usually done by using a molecule that has donor-acceptor structure, which means that the excited states have a charge transfer (CT) character. A CT excitation has almost degenerate spin states because of the small overlap of the electron and hole wavefunction. In the TADF process, the triplet can become a singlet due to the near degeneracy of the two states. This process is called Reverse InterSystem Crossing (RISC). Thermal activation is able to promote

a triplet to a singlet, after which the singlet can emit radiatively. In such devices 100% IQE is possible [57, 27, 31]. A common disadvantage of the TADF donor-acceptor type molecules is that their emission spectrum is rather broad. This is tied to the CT character of the excited state. A CT state is often strongly polarized and its energy is therefore strongly influenced by its local environment. This leads a broadened spectrum. One of the ways to narrow the spectral width in TADF devices is to decouple the functions of the TADF emitter. First, the triplets in the device are promoted to singlets using a TADF sensitizer. This can be a regular TADF molecule with a broad emission spectrum. Consecutively, the singlets are transfered to a regular fluorescent emitter from which the emission of light takes place. Such strategies for narrowing the spectra of TADF OLEDs have been successfully demonstrated [19, 2].

The above examples of the complex device physics of phosphorescent and TADF type OLEDs illustrate quite well both the difficulties but also the potential of working with organic materials. Smart molecular and device design strategies can boost the device performance and lead to the use of more processable, cheaper and environmentally friendly materials. However, in every step of the development the combination of molecular materials needs to be tested and devices have to be optimized. It is therefore very desirable to employ an *in silico* design strategy to this problem. This means that we use reliable computer models to test the new molecules and device designs in order to better understand what works and how it works. In the next section we will discuss the nature of transport in organic semiconductors and arrive at the multi-scale modelling strategy that is used to approach the simulation of devices.

1.3 Computational modelling of OLEDs

1.3.1 Hopping transport

The localization of charge carriers in disordered organic semiconductors leads to transport via hopping. Hopping transport was first introduced in impurity conduction in inorganic solids by Conwell and Mott [36, 47] in 1956. They found that in these systems the conductivity increases with temperature, which is opposite to the behavior found in regular (semi)-conductors. This led to the realization that charge transport can be described by a series discrete hops that are thermally activated. The same behavior is found in molecular semiconductors. In 1959, Holstein developed a model for charge transport in molecular crystals based on the localization of charges on molecular sites [25]. On a molecule the electron is localized in the lowest unoccupied molecular orbital (LUMO) and will hop to the LUMO of an adjacent molecule. The hole is localized in the highest occupied molecular orbital (HOMO) and will hop to the HOMO of an adjacent molecule. The HOMO and LUMO energies vary from one molecule to the next. Often these variations originate from many uncorrelated sources. Using the central limit theorem the energies can then be well described by a Gaussian distribution (see Fig. 1.3) also called a Gaussian Density Of States (DOS).

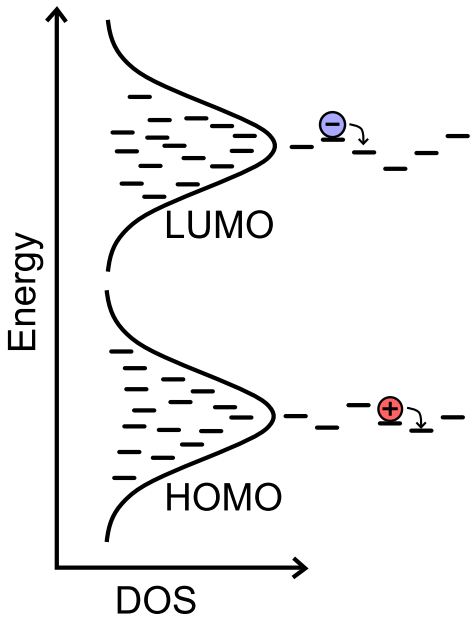

Figure 1.3: Schematic depiction of a Gaussian density of states in disordered organic semiconductors. The electrons occupy the LUMO energy levels of the molecules, while the holes occupy the HOMO levels.

The thermally activated nature of transport has also been observed for excitons [43]. The exciton levels in organic semiconductors are, similar to the HOMO and LUMO levels, energetically disordered. The strength of the energetic disorder for exciton levels is often smaller. This is because the exciton is neutral, and therefore less influenced by the polarization of the local environment.

1.3.2 Computational modelling

The fact that transport in disordered organic semiconductor occurs via hopping can be exploited in computational modelling. The rate of hopping can be calculated using a model that includes the molecular details to describe the transfer of a carrier on a molecular scale. This rate can then be used as input in a model with less molecular details to describe the transport on larger length and time scales. Such a modelling approach is commonly referred to as *multi-scale modelling*. The approach starts by calculating the molecular properties using first-principles techniques. The next step is to use a method to simulate a microscopic morphology material consisting of molecules. Such methods often neglect some of the quantum mechanical nature of

the problem. From this morphology, the spatial, orientational and energetic disorder of the materials is extracted. This disorder is then upscaled using stochastic methods and a complete morphology on the device scale is generated with unique positions, energies and orientations for all the molecules. The molecules are then no longer represented in their full detail, but they are merely point sites in a 3 dimensional space. Then, the charge or exciton transfer rates between the sites are calculated. Using these rates we can simulate the transport process using stochastic simulation techniques like Kinetic Monte Carlo (KMC) or by setting up a system of equations for all the transfer rates, called the Master Equation (ME), and solving this numerically.

and the transport equation can be solved to yield the macroscopic mobility or diffusivity. The length scales in the multi-scale approach are depicted in figure 1.4.

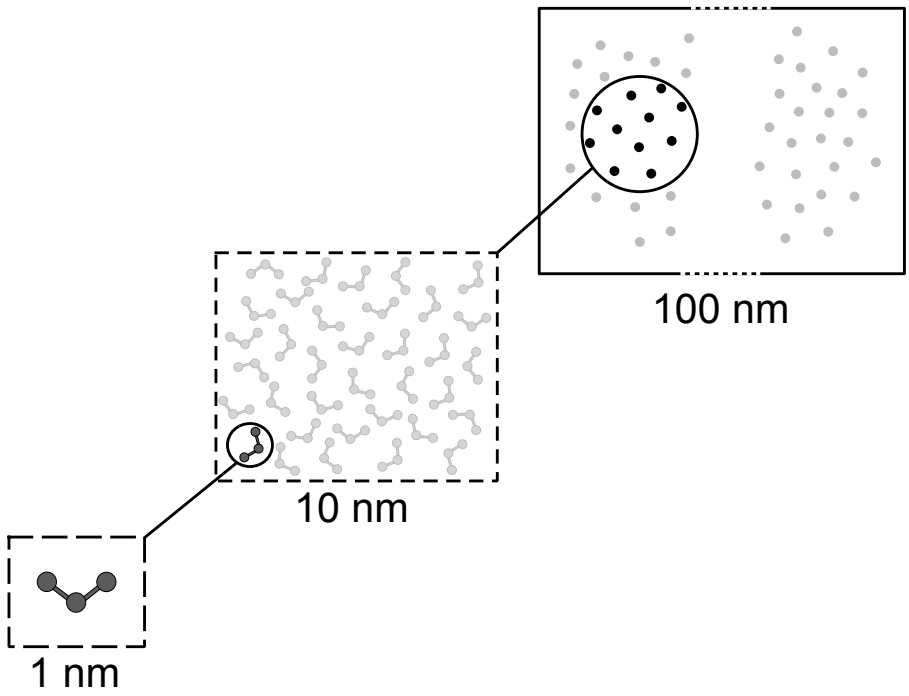

Figure 1.4: Schematic representation of the different length scales treated by the multi-scale modelling approach. The device scale is on the order of 100 nm, while the simulated microscopic morphologies have lateral dimensions of roughly 10 nm. Finally, the molecular size is on the order of 1 nm.

The multi-scale modelling approach for charge and exciton transport relies on the

fact that the macroscopic transport phenomena arise from a series of transfer events. Once we physically describe the transfer events between the molecular sites, all the remaining physics comes from the stochastic simulation methods like the KMC and ME. This is only possible because the electronic coupling between molecular sites is weak with respect to the energetic disorder and the electron-vibrational coupling. In the next section we will introduce the transfer theories which lie at the foundation of setting up the transport models in this work.

1.4 Theory of charge and exciton transfer

The general picture of hopping transport in organic semiconductors is that carriers are transported through a molecular material by hopping from one molecule or molecular site to the next. Within this view the fundamental time step in the transport process is the carrier transfer from one site to the next. Quantum-mechanically, the rate for a transfer process between two states is described by Fermi's Golden Rule (FGR)

$$k = \frac{2\pi}{\hbar} \sum_{i,f} p_i |\langle \psi_i | H' | \psi_f \rangle|^2 \, \delta(\Delta E). \tag{1.1}$$

In Fermi's Golden Rule, the molecular sites are weakly coupled by a perturbation term in the Hamiltonian $|\langle \psi_i | H' | \psi_f \rangle|$. The δ-function with $\Delta E = E_f - E_i$ ensures energetic resonance between the initial (E_i) and final (E_f) states. The sum in Eq. 1.1 then runs over all the initial i and final f states where the initial states are weighted by their occupational probabilities p_i. In molecular systems we can use the Born-Oppenheimer approximation to separate the electronic and nuclear parts of the wavefunction

$$\psi = \phi(r)\chi(R). \tag{1.2}$$

We now express the motion of the nuclei along the normal mode coordinates which describe the intramolecular vibrations also called vibrons. Assuming that the transfer involves only one initial electronic state ϕ_i and one final electronic state ϕ_f we can rewrite Eq. 1.1 as

$$k = \frac{2\pi}{\hbar} J^2 \, \rho_{\mathrm{FC}}(\Delta E). \tag{1.3}$$

Here

$$J = |\langle \phi_i | H' | \phi_f \rangle|, \tag{1.4}$$

is called the *transfer integral* and

$$\rho_{\mathrm{FC}} = \sum_{i,f} p_i |\langle \chi_i | \chi_f \rangle|^2 \delta(\Delta E), \tag{1.5}$$

is called the *Franck-Condon Weighted Density of states* (FCWD). The FCWD sums over the transitions from any of the Boltzmann weighted (p_i) initial vibron states (χ_i) to any of the final vibron states (χ_f) weighted by the squared Franck-Condon factors, which are the overlap integrals of the vibron wavefunctions. The Franck-Condon weighted density of states should not be confused with the Gaussian density of states introduced before for the molecular materials. The latter is determined by the variation in energy between the molecules, while the FCWD is a purely intramolecular density of states. The exact expression for the FCWD will be developed in the next chapter. In the next subsections we will discuss the different approximations to the transfer integral and the FCWD.

1.4.1 Marcus theory

In the high temperature limit, when the quantized nature of the intramolecular vibrations dissapears, the FCWD is well approximated by the semi-classical Marcus theory [37]. Marcus showed that if the molecular vibrations are treated classically the transfer can be described by a harmonic potential crossing. This crossing is depicted by the red arrow in Fig. 1.5.

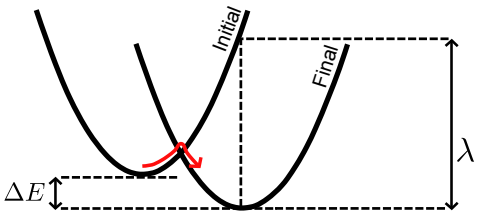

Figure 1.5: Schematic representation of Marcus transfer theory, with λ the reorganization energy and ΔE the energy difference between the initial and final state.

Here, the energy required to cross from the initial state to the final state is given by $E_{\mathrm{A}} = \frac{(\Delta E+\lambda)^2}{4\lambda}$. The λ term is called the reorganization energy and is induced by the displacement of the initial and final state harmonic potentials. This displacement is due to the coupling of the charge to the molecular vibrations. From the activation energy E_{A} the FCWD then becomes

$$\rho_{\mathrm{Marcus}} = \frac{1}{\sqrt{4\pi\lambda k_{\mathrm{B}}T}} \exp\left(-\frac{(\Delta E+\lambda)^2}{4\lambda k_{\mathrm{B}}T}\right). \tag{1.6}$$

Though the theory was initially developed for charge transfer it can also be applied to exciton transfer, by simply using the coupling of the vibrations to the exciton instead of the charge [12].

As can be seen from Eq. 1.6, if the reorganization energy reaches the value $\lambda = -\Delta E$, the Marcus rate reaches a maximum. When ΔE decreases further the rate enters the *inverted* region where it decreases again. The *inverted* region was an important element of Marcus theory, which explained the experimentally found decrease of the transfer rate at large excess transfer energy [45].

1.4.2 Miller-Abrahams theory

In 1960 Allen Miller and Elihu Abrahams formulated an expression for impurity hopping in an n-type semiconductor [44]. In their work they assume a constant density of final states for the transfer. This leads to a rate that is constant when $\Delta E < 0$ and is weighted by a Boltzmann factor for $\Delta E > 0$ leading to the expression

$$\rho_{\mathrm{MA}} = \nu_0 \exp\left(-\frac{\Delta E}{2k_B T} - \frac{|\Delta E|}{2k_B T}\right). \tag{1.7}$$

The theory involves a prefactor, called the hopping attempt frequency (ν_0), which is often fit to reproduce experiments. The theory is only physically correct for molecular systems if the transfer at $\Delta E \neq 0$ is activated by the absorption or emission of a single vibration on the molecule [15]. The theory should be interpreted as semi-emperical because the activation realistically never occurs by just one vibration. With the fitted prefactor, the theory often performs well in describing the temperature dependence of charge and exciton transport and the field dependence of charge transport. In Chapter 3 we will show that the Miller-Abrahams theory sometimes gives more satisfying results for molecular systems than the Marcus theory.

1.4.3 Marcus-Levich-Jortner theory

A first quantum mechanical model for the coupling of molecular vibrations to electron transfer that goes beyond the semi-classical Marcus model has been developed by Marcus, Levich, Jortner and Bixon [38, 26, 11]. In this model, the Franck-Condon factors are used to derive an expression for the ρ_{FC} based on a single quantum mechanical mode and an additional reorganization energy induced by the environment of the molecules. The expression that in literature is commonly known as the Marcus-Levich-Jortner (MLJ) expression is

$$\rho_{\mathrm{MLJ}} = \frac{1}{\sqrt{4\pi\lambda_{\mathrm{cl}} k_{\mathrm{B}} T}} \exp\left(-\frac{\lambda_{\mathrm{qm}}}{\hbar\omega}\right) \sum_n \frac{\left(\frac{\lambda_{\mathrm{qm}}}{\hbar\omega}\right)^n}{n!} \exp\left(-\frac{(\Delta E + \lambda_{\mathrm{cl}} + n\hbar\omega)^2}{4\lambda_{\mathrm{cl}} k_{\mathrm{B}} T}\right). \tag{1.8}$$

Here, the reorganization energy is separated into a quantum mechanical (intramolecular) λ_{qm} and a classical (external) λ_{cl} part as depicted in Fig. 1.6. The coupling of the quantum mechanical reorganization energy is then described by a single harmonic quantum oscillator with frequency ω.

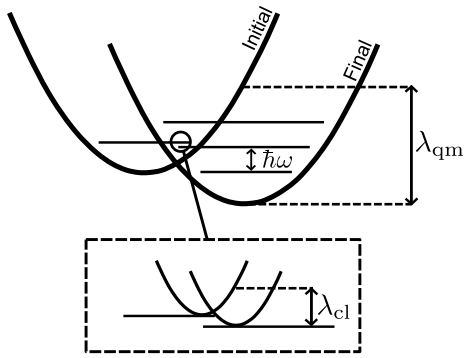

Figure 1.6: Schematic representation of MLJ transfer theory. With λ_{qm} the quantum mechanical reorganization energy, $\hbar\omega$ the vibration energy of the quantum mechanical mode, and λ_{cl} the classical reorganization energy.

In the theory it is assumed that the quantum mechanical mode in the initial state is not vibrationally excited. For the vibrational energies of the quantum-mechanical mode this is usually a good assumption since $\hbar\omega \gg k_{\mathrm{B}}T$. However, due to the neglect of thermal occupation of the vibrational mode the theory technically does not obey detailed balance. It was noted in the original paper that this form of the theory is only applicable to the low temperature regime [26]. However, in literature it is commonly applied to all temperatures [17, 54, 13, 61].

1.4.4 Franck-Condon weighted density of states

In this thesis we have developed the *full* Franck-Condon weighted density of states [52, 12]. This model extends on the Marcus-Levich-Jortner model in two ways. First, it includes all the vibrons (molecular vibrations) quantum mechanically instead of just one effective mode. Second, it takes into account the thermal occupation of the quantum mechanical modes, whereas in the MLJ theory the initial vibron mode is always unnocupied. In Chapter 2 we will introduce the expression for this rate as a function of ΔE and the molecular vibron mode energies ($\hbar\omega_i$) and vibron couplings (λ_i).

1.4.5 Charge transfer integrals

While we discussed the Marcus, Miller-Abrahams and Jortner approximations for the FCWD we did not discuss the perturbation term J in Eq. (1.3), which allows the carrier transfer to occur. Early theories of electron and hole transfer have usually taken this term to be proportional to the wavefunction overlap. Since the wavefunction falls

off exponentially, the transfer integral is often chosen to be

$$J^2 \propto \exp\left(-\frac{2R}{L}\right). \tag{1.9}$$

Where L is the wavefunction decay length [16].

In the last 20 years, the feasability of performing *ab-initio* calculations for organic molecules has led to the introduction of multiple methods to calculate the transfer integrals for electrons and holes in organic semiconductors [58, 33, 8]. Most of these methods are based on a two-state description of a molecular dimer where both monomer electron states (LUMO) or hole states (HOMO) are weakly coupled. In a symmetric dimer system the splitting of the HOMO or LUMO energies in the dimer state can be used to find the transfer integral. The reasoning for this goes as follows. If the HOMO or LUMO energies of the monomers are given by E_{M} and the transfer integral is given by $J^2 = J_{\mathrm{DA}}^2$ then the Hamiltonian for the dimer system can be written as

$$H = \begin{pmatrix} E_{\mathrm{M}} & J_{\mathrm{DA}} \\ J_{\mathrm{DA}} & E_{\mathrm{M}} \end{pmatrix}. \tag{1.10}$$

The diagonalization of the Hamiltonian leads to

$$E_{1,2} = E_{\mathrm{M}} \pm |J_{\mathrm{DA}}|. \tag{1.11}$$

So the transfer integral is found by

$$2|J_{\mathrm{DA}}| = E_2 - E_1. \tag{1.12}$$

Where $E_{1,2}$ are the energies of the molecular dimer, which are split from the single molecule levels E_{M}. The dimer energies can be found from an *ab-initio* calculation for the molecular dimer system. In the Chapter 2 we will show how to extend this simple model to systems that are not symmetric.

1.4.6 Förster transfer

The phenomenon of excitation transfer in fluorescent molecules was already described in 1948 by Theodor Förster [55]. Förster described the excitation transfer within first order perturbation theory, where the transfer integral is described by the transition dipole coupling of the donor and acceptor molecules [51]

$$J^2_{\mathrm{Förster}} \propto \frac{\mu_{\mathrm{D}}^2 \mu_{\mathrm{A}}^2}{R^6}. \tag{1.13}$$

In Förster theory, the squared transition dipole moment of the donor (μ_{D}^2) is obtained from the donor lifetime τ_{D}. The squared transition dipole moment of the acceptor (μ_{A}^2) is obtained from the donor-acceptor spectral overlap, which then also contains

the FCWD. The donor-acceptor spectral overlap is included in one parameter called the Förster radius (R_0), which then yields the Förster transfer rate

$$k_{\text{Förster}} = \frac{1}{\tau_{\text{D}}}\left(\frac{R_0}{R}\right)^6. \tag{1.14}$$

It is important to note that for Förster transfer to occur, the transition from the excited state to the ground state has to be allowed. This means that in fluorescent molecules the Förster transfer of triplets is forbidden. In phosphorescent molecules Förster transfer is allowed because of the strong spin-orbit coupling, which allows the transition from the triplet excited state to the singlet ground state. In Chapter 2 we will show how to derive the Förster rate from Fermi's Golden Rule Eq. (1.1).

1.4.7 Dexter transfer

In 1953 Dexter developed a more general theory for excitation transfer in inorganic solids [16]. He describes the dipole-dipole interactions (earlier described by Förster), dipole-quadrupole interactions and the exchange interaction. From those three factors the last one, the exchange interaction, is commonly refered to as the Dexter interaction in literature [51]. In his work, Dexter mentiones that the interaction is exponentially dependent on the wavefunction overlap and therefore

$$J^2_{\text{Dexter}} \propto \exp\left(-\frac{2R}{L}\right). \tag{1.15}$$

Where L is the wavefunction decay length. We note that this formula is equivalent to the approximation for the charge transfer integrals in Eq. (1.9). In Chapter 2 we will discuss how to calculate the Dexter exchange interaction from *ab-initio* calculations.

1.4.8 Fermi's Golden Rule

In this section we have seen that the historically developed theories for charge and exciton transfer can all be linked to certain approximations of the transfer integral and FCWD in Fermi's Golden Rule Eq. 1.3. This general trend is schematically depicted in Fig. 1.7.

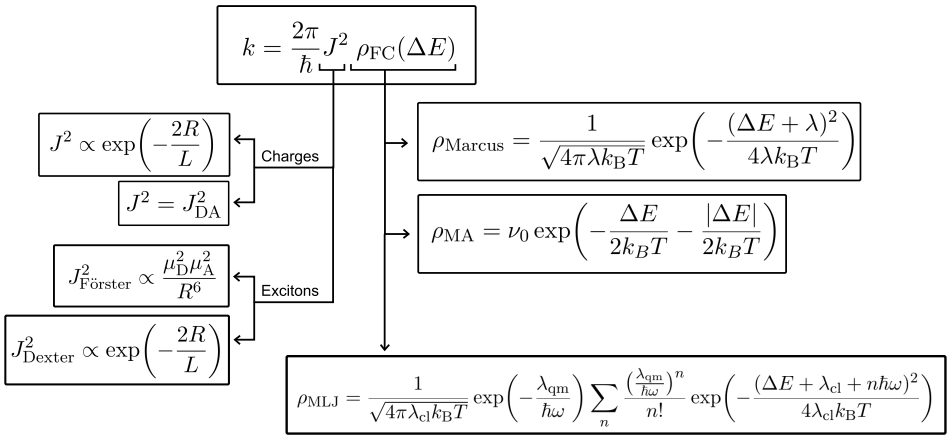

Figure 1.7: Schematic which links the different charge and exciton transfer theories to the transfer integral and density of states in Fermi's Golden Rule.

From this scheme it is clear that for example the Marcus theory for charge transfer might just as well be applied to exciton transfer, as long as the reorganization energy of the exciton is used instead of the charge reorganization energy.

The next section will introduce the transport simulation tools that use the previously discussed transfer theories to simulate charge and exciton transport in OLED materials.

1.5 Modelling transport in organic semiconductors

Now that we have introduced the different charge and exciton transfer theories we will discuss how to simulate the transport on the scale of the device. After that, we will give an overview of what a complete simulation, starting from the *ab-initio* calculations, looks like.

1.5.1 Modelling charge transport

In 1993 Bässler performed the first 3D simulations of charge transport in organic semiconductors [7]. Bässler used Kinetic Monte Carlo (KMC) to describe hopping of a single carrier on a cubic lattice. The hopping rates between the different sites were calculated by Miller-Abrahams theory, where the energies of the lattice sites were drawn from a Gaussian distribution. This has led to the development of the Gaussian Disorder Model (GDM). From this work, the field and temperature dependence of the charge-carrier mobility in the zero-carrier-concentration limit was obtained.

The carrier concentration dependence of the mobility was later studied by Yu *et al.* [62], using 3D Master Equation (ME) simulation by . The 3D-ME simulation is more efficient at high carrier concentrations than KMC because it does not simulate the individual carriers explicitely but rather simulates their occupation probabilities.

In the past years both the Master Equation and Kinetic Monte Carlo methods have been extensively developed to study transport in organic semiconductors. The simulations are including an increasing amount of molecular detail, approaching charge mobility prediction from molecular structure. In recent years, off-lattice transport simulations have been performed by simulating the actual morphologies of the molecular materials. Such morphologies are generated by either molecular dynamics simulations [50, 9, 40, 4] or even more elaborate methods simulating the deposition process of molecular films [48]. In simulations with realistic morphologies the transfer integrals between the molecular pairs are often calculated explicitely [8, 50, 4, 18] instead of using the wavefunction decay length from Eq. (1.9). In this way, the calculated transfer integrals include the orientational disorder in the molecular film and the detailed shape of the molecular wavefunction. Other improvements to the transport simulations include the application of Marcus theory with reorganization energies calculated from *ab-initio* methods [8, 50, 4, 18], and energetic disorder calculated from either atomistic polarizability models [50, 40, 4] or *ab-initio* models [18]. There are now succesfull demonstrations of models that combine the molecular properties (energy levels, reorganization energies and transfer integrals) and the different types of disorder (energetic, spatial and orientational) to predict charge carrier mobilities that match experimental values [34, 39, 18, 30].

1.5.2 Modelling exciton transport

Exciton transport in organic semiconductors has been studied in the 1980s by Gochanour [20], Godzik and Jortner [21] using Master Equation methods. One of the first uses of Kinetic Monte Carlo was by Schönherr [53]. More recently, models for equilibrium and non-equilibrium hopping of excitons have been developed by Athanasopoulos [5]. In that work, the exciton transfer integrals were already calculated using quantum-chemical calculations. The differences between the Miller-Abrahams and Marcus theory for exciton diffusion were studied by Hoffmann *et al.* [24], who found a significantly different temperature dependence of the diffusion for both theories. Many of the exciton transport studies are focused on polymer systems or molecular crystals. Models for exciton transport in OLEDs are often analytical or do not include the important molecular details that are present in the state of the art charge transport models discussed in the last subsection.

In this section we have introduced charge and exciton transport models. Generalizing, we can see that a successful predictive model can be built starting from *ab-initio* calculations introducing the molecular properties into the transfer equations and evolving the transfer equations for energetic, spatial and orientational disorder. The general outline of this framework is depicted in Fig. 1.8. In this framework the

microscopic parameters represent the molecular and disorder information that enter the Master Equation or Kinetic Monte Carlo model. The translation from the microscopic to the mesoscopic scale is made by the transfer theory.

1.6 OLED device models

The transport models introduced in the last section can be adapted to simulate not only transfer events, but also exciton generation, radiative and non-radiative decay and even more complicated processes like TTA and TPQ. Simulations including these processes have already been demonstrated using Kinetic Monte Carlo [42, 59, 14, 60] and Master Equation methods [35, 63]. Within the framework of Kinetic Monte Carlo, the incorporation of additional processes is rather straightforward. In principle, the only information needed are the rates for the different processes that can occur in the device. First-principles calculations of radiative and non-radiative rates for molecules relevant to OLED applications have already been reported [46, 22, 49]. To our knowledge, such rate calculations have not yet been performed for the TTA and TPQ processes. In the outlook in Chapter 6 we will present ideas on calculating rates for these processes.

1.7 Scope of this thesis

In this chapter we have discussed the importance of device transport simulations for OLED research and development. We outlined the multi-scale modelling approach, the charge and exciton transfer theories and transport simulation work that has been performed in the last years. Figure 1.8 schematically depicts the multi-scale modelling approach.

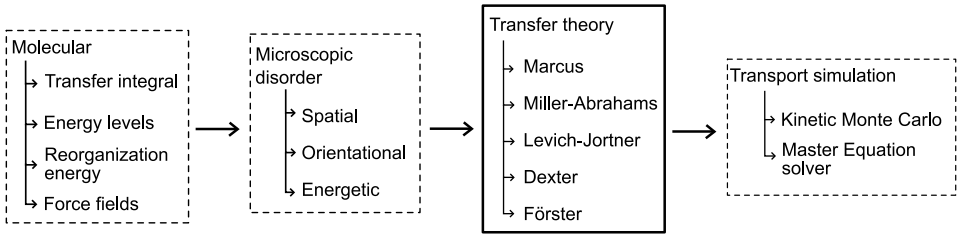

Figure 1.8: Scheme of the multi-scale modelling. Molecular calculations serve as input for microscopic disorder calculations, which then serves as input for the transfer theories. The transport in the system is modelled using the transfer theories with, for example, Kinetic Monte Carlo or a Master Equation solver. The dashed boxes indicate that we do not focus on the development of those steps in the multi-scale modelling process. The transfer theory is highlighted because that is the main focus of this thesis.

This schematic represents the workflow that is often followed in multi-scale modelling for transport in organic semiconductors [34, 39, 29, 18, 30]. The methods start with the calculations on the molecular scale, either single molecule or dimer calculations. Then, the disorder is introduced in a classical or semi-classical way. The force field parametrization of the classical simulations are derived from the molecular calculations. This will yield a distribution of the molecular energies, orientations and positions. These distributions are then often approximated stochastically. The stochastic models are used to generate a transport network on the device scale. Such a network consists of connected molecular sites. For this network, all the transfer rates between the molecules are calculated and the transport is simulated. This underlines the critical role that the transfer theory plays in the charge and exciton transport. Even if we can calculate all the molecular parameters and their disorder correctly, the dynamics/outcome of the simulation will still be determined by the transfer theories.

In literature there is much focus on the development of disorder calculations which correctly include the quantum mechanics. However, the vibronic coupling in the transfer is often treated classically with Marcus theory [8, 50, 4, 18]. The use of the Marcus theory for charge transport in organic semiconductors will be evaluated in **Chapter 3** of this thesis. We will use a FGR rate that includes all the detailed molecular vibrations to calculate charge mobilities in common OLED materials. We compare the results to the application of the Miller-Abrahams and semi-classical Marcus rates. We find that the charge mobilities of the full FGR rate differ from the Marcus theory results especially at low temperatures, where the classical approximation breaks down.

A multi-scale modelling approach for exciton transport has not been demonstrated up to now. In **Chapter 4** we will develop such a mode. Using the same principles

from the charge transport multi-scale approach, we develop a model for triplet exciton diffusion in phosphorescent emitters commonly used in OLEDs. For the exciton transfer we also use the full FGR rate and compare it to the Marcus rate. We find that Marcus theory dramatically underestimates the transfer rate for triplet excitons in these systems. Additionally, we look at the contribution of the short-range Dexter and long-range Förster contribution to the triplet transfer for realistic host-guest systems. We find that for guest concentrations often used in OLEDs the Förster contribution solely dominates the transfer rate.

Chapter 5 focuses on exothermic energy transfer, for example the transfer of an exciton from a green donor emitter to a red acceptor emitter. Such transfers play an important role in the development of White OLEDs (WOLEDs). We investigate the energy transfer between 14 different phosphorescent emitters ranging in emission color from the near infrared to the deep blue. We apply a Förster theory type transfer integral combined with the full vibrational coupling to the triplet exciton transfer. We find that for transfers with large excess energy, multiple excited states of the acceptor molecule have to be included in calculating the transfer. This leads to a general framework for calculating Förster transfer from first-principles between different donor and acceptor emitters.

The multi-scale methods employed in this thesis are introduced in **Chapter 2**. The focus in this chapter is on the development of the FGR rate. However, we will also briefly discuss first-principles methods, the calculation of the transfer integrals and vibronic couplings, the calculation of the energetic, spatial and orientational disorder, and finally, the transport simulations used in this thesis.

We end the thesis with an outlook in **Chapter 6**, were we show how the FGR expression might be important to describe the host to guest charge transfer which plays a role in the formation of excitons in the OLED emissive layer. We also propose methods to calculate the triplet-polaron quenching rate.

Bibliography

[1] C. Adachi, M. A. Baldo, M. E. Thompson, and S. R. Forrest. Nearly 100% internal phosphorescence efficiency in an organic light emitting device. *J. Appl. Phys.*, 90(10):5048–5051, 2001. ISSN 00218979. doi: 10.1063/1.1409582.

[2] D. H. Ahn, J. H. Jeong, J. Song, J. Y. Lee, and J. H. Kwon. Highly Efficient Deep Blue Fluorescent Organic Light-Emitting Diodes Boosted by Thermally Activated Delayed Fluorescence Sensitization. *ACS Appl. Mater. Interfaces*, 10 (12):10246–10253, 2018. ISSN 19448252. doi: 10.1021/acsami.7b19030.

[3] H. Akamuta, H. Inokuchi, and Y. Matsunaga. Electrical Conductivity of the Perylene–Bromine Complex. *Nature*, 173(4395):168–169, 1954. ISSN 1476-4687. doi: 10.1038/173168a0. URL `https://doi.org/10.1038/173168a0`.

[4] D. Andrienko. Modeling of organic light emitting diodes: From molecular to device properties. *Proc. Int. Conf. Numer. Simul. Optoelectron. Devices, NUSOD*, pages 101–102, 2017. ISSN 21583234. doi: 10.1109/NUSOD.2017.8010011.

[5] S. Athanasopoulos, E. V. Emelianova, A. B. Walker, and D. Beljonne. Exciton diffusion in energetically disordered organic materials. *Phys. Rev. B*, 80(19): 195209, 2009. ISSN 1098-0121. doi: 10.1103/PhysRevB.80.195209. URL `https://link.aps.org/doi/10.1103/PhysRevB.80.195209`.

[6] M. A. Baldo, D. F. O'Brien, Y. You, A. Shoustikov, S. Sibley, M. E. Thompson, and S. R. Forrest. Highly efficient phosphorescent emission from organic electroluminescent devices. *Nature*, 395(6698):151–154, 1998.

[7] H. Bässler. Charge Transport in Disordered Organic Photoconductors a Monte Carlo Simulation Study. *Phys. Status Solidi B*, 175(1):15–56, 1993. ISSN 03701972. doi: 10.1002/pssb.2221750102. URL `http://doi.wiley.com/10.1002/pssb.2221750102`.

[8] B. Baumeier, J. Kirkpatrick, and D. Andrienko. Density-functional based determination of intermolecular charge transfer properties for large-scale morphologies. *Phys. Chem. Chem. Phys.*, 12(36):11103–11113, 2010. ISSN 14639076. doi: 10.1039/c002337j.

[9] B. Baumeier, O. Stenzel, C. Poelking, D. Andrienko, and V. Schmidt. Stochastic modeling of molecular charge transport networks. *Phys. Rev. B - Condens. Matter Mater. Phys.*, 86(18):1–7, 2012. ISSN 10980121. doi: 10.1103/PhysRevB.86.184202.

[10] A. Bernanose, M. Comte, and P. Vouaux. A new method of emission of light by certain organic compounds. *J. Chim. Phys.*, 50:64, 1953.

[11] M. Bixon and J. Jortner. Quantum effects on electron-transfer processes. *Faraday Discuss. Chem. Soc.*, 74:17–29, 1982. ISSN 03017249. doi: 10.1039/DC9827400017.

[12] J. L. Brédas, D. Beljonne, V. Coropceanu, and J. Cornil. Charge-transfer and energy-transfer processes in π-conjugated oligomers and polymers: A molecular picture. *Chem. Rev.*, 104(11):4971–5003, 2004. ISSN 00092665. doi: 10.1021/cr040084k.

[13] S. Chaudhuri, S. Hedström, D. D. Méndez-Hernández, H. P. Hendrickson, K. A. Jung, J. Ho, and V. S. Batista. Electron Transfer Assisted by Vibronic Coupling from Multiple Modes. *J. Chem. Theory Comput.*, 13(12):6000–6009, 2017. ISSN 15499626. doi: 10.1021/acs.jctc.7b00513.

[14] R. Coehoorn, H. Van Eersel, P. A. Bobbert, and R. A. Janssen. Kinetic Monte Carlo Study of the Sensitivity of OLED Efficiency and Lifetime to Materials Parameters. *Adv. Funct. Mater.*, 25(13):2024–2037, 2015. ISSN 16163028. doi: 10.1002/adfm.201402532.

[15] V. Coropceanu, J. Cornil, D. A. da Silva Filho, Y. Olivier, R. Silbey, and J. L. Brédas. Charge transport in organic semiconductors. *Chem. Rev.*, 107(4):926–952, 2007. ISSN 00092665. doi: 10.1021/cr050140x.

[16] D. L. Dexter. A theory of sensitized luminescence in solids. *J. Chem. Phys.*, 21 (5):836–850, 1953. ISSN 00219606. doi: 10.1063/1.1699044.

[17] E. Di Donato, R. P. Fornari, S. Di Motta, Y. Li, Z. Wang, and F. Negri. N-type charge transport and mobility of fluorinated perylene bisimide semiconductors. *J. Phys. Chem. B*, 114(16):5327–5334, 2010. ISSN 15205207. doi: 10.1021/jp101040r.

[18] P. Friederich, V. Meded, A. Poschlad, T. Neumann, V. Rodin, V. Stehr, F. Symalla, D. Danilov, G. Lüdemann, R. F. Fink, I. Kondov, F. von Wrochem, and W. Wenzel. Molecular Origin of the Charge Carrier Mobility in Small Molecule Organic Semiconductors. *Adv. Funct. Mater.*, 26(31):5757–5763, 2016. ISSN 16163028. doi: 10.1002/adfm.201601807.

[19] T. Furukawa, H. Nakanotani, M. Inoue, and C. Adachi. Dual enhancement of electroluminescence efficiency and operational stability by rapid upconversion of triplet excitons in OLEDs. *Sci. Rep.*, 5:8429, 2015. ISSN 20452322. doi: 10.1038/srep08429.

[20] C. R. Gochanour, H. C. Andersen, and M. D. Fayer. Electronic excited state transport in solution. *J. Chem. Phys.*, 70(9):4254–4271, 1979. ISSN 00219606. doi: 10.1063/1.437999.

[21] K. Godzik and J. Jortner. Electronic energy transport in substitutionally disordered molecular crystals. *J. Chem. Phys.*, 72(8):4471–4486, 1980. ISSN 0021-9606. doi: 10.1063/1.439688.

[22] A. Heil, K. Gollnisch, M. Kleinschmidt, and C. M. Marian. On the photophysics of four heteroleptic iridium(III) phenylpyridyl complexes investigated by relativistic multi-configuration methods. *Mol. Phys.*, 114:407–422, 2016. ISSN 13623028. doi: 10.1080/00268976.2015.1076902. URL `http://dx.doi.org/10.1080/00268976.2015.1076902`.

[23] P. Heimel, A. Mondal, F. May, W. Kowalsky, C. Lennartz, D. Andrienko, and R. Lovrincic. Unicolored phosphor-sensitized fluorescence for efficient and stable blue OLEDs. *Nat. Commun.*, 9(1):1–8, 2018. ISSN 20411723. doi: 10.1038/s41467-018-07432-2.

[24] S. T. Hoffmann, S. Athanasopoulos, D. Beljonne, H. Bässler, and A. Köhler. How do triplets and charges move in disordered organic semiconductors? A Monte Carlo study comprising the equilibrium and nonequilibrium regime. *J. Phys. Chem. C*, 116(31):16371–16383, 2012. ISSN 19327447. doi: 10.1021/jp305062p.

[25] T. Holstein. Studies of polaron motion: Part I. The molecular-crystal model. *Ann. Phys. (N. Y).*, 281(1-2):706–724, 1959. ISSN 00034916. doi: 10.1006/aphy.2000.6020.

[26] J. Jortner. Temperature dependent activation energy for electron transfer between biological molecules. *J. Chem. Phys.*, 64(12):4860–4867, 1976. ISSN 00219606. doi: 10.1063/1.432142.

[27] H. Kaji, H. Suzuki, T. Fukushima, K. Shizu, K. Suzuki, S. Kubo, T. Komino, H. Oiwa, F. Suzuki, A. Wakamiya, Y. Murata, and C. Adachi. Purely organic electroluminescent material realizing 100% conversion from electricity to light. *Nat. Commun.*, 6(May):1–8, 2015. ISSN 20411723. doi: 10.1038/ncomms9476. URL `http://dx.doi.org/10.1038/ncomms9476`.

[28] Y. Kawamura, K. Goushi, J. Brooks, J. J. Brown, H. Sasabe, and C. Adachi. 100% phosphorescence quantum efficiency of Ir (III) complexes in organic semiconductor films. *Appl. Phys. Lett.*, 86:1–3, 2005. ISSN 00036951. doi: 10.1063/1.1862777.

[29] P. Kordt, J. J. M. van der Holst, M. Al Helwi, W. Kowalsky, F. May, A. Badinski, C. Lennartz, and D. Andrienko. Modeling of Organic Light Emitting Diodes: From Molecular to Device Properties. *Adv. Funct. Mater.*, 25(13):1955–1971, 2015. doi: 10.1002/adfm.201403004. URL `https://onlinelibrary.wiley.com/doi/abs/10.1002/adfm.201403004`.

[30] N. B. Kotadiya, A. Mondal, S. Xiong, P. W. Blom, D. Andrienko, and G. J. A. Wetzelaer. Rigorous Characterization and Predictive Modeling of Hole Transport in Amorphous Organic Semiconductors. *Adv. Electron. Mater.*, 4(12):1–7, 2018. ISSN 2199160X. doi: 10.1002/aelm.201800366.

[31] D. R. Lee, B. S. Kim, C. W. Lee, Y. Im, K. S. Yook, S. H. Hwang, and J. Y. Lee. Above 30% external quantum efficiency in green delayed fluorescent organic light-emitting diodes. *ACS Appl. Mater. Interfaces*, 7(18):9625–9629, 2015. ISSN 19448252. doi: 10.1021/acsami.5b01220.

[32] J. Lee, H. F. Chen, T. Batagoda, C. Coburn, P. I. Djurovich, M. E. Thompson, and S. R. Forrest. Deep blue phosphorescent organic light-emitting diodes with very high brightness and efficiency. *Nat. Mater.*, 15(1):92–98, 2016. ISSN 14764660. doi: 10.1038/nmat4446.

[33] H. Li, J. L. Bŕdas, and C. Lennartz. First-principles theoretical investigation of the electronic couplings in single crystals of phenanthroline-based organic semiconductors. *J. Chem. Phys.*, 126(16), 2007. ISSN 00219606. doi: 10.1063/1.2727480.

[34] F. Liu, A. Massé, P. Friederich, F. Symalla, R. Nitsche, W. Wenzel, R. Coehoorn, and P. A. Bobbert. Ab initio modeling of steady-state and time-dependent charge transport in hole-only α -NPD devices. *Appl. Phys. Lett.*, 109(24), 2016. ISSN 00036951. doi: 10.1063/1.4971969.

[35] F. Liu, H. Van Eersel, P. A. Bobbert, and R. Coehoorn. Three-Dimensional Modeling of Bipolar Charge-Carrier Transport and Recombination in Disordered Organic Semiconductor Devices at Low Voltages. *Phys. Rev. Appl.*, 10(5):1, 2018. ISSN 23317019. doi: 10.1103/PhysRevApplied.10.054007. URL `https://doi.org/10.1103/PhysRevApplied.10.054007`.

[36] E. M . Conwell. Impurity Band Conduction in Germanium and Silicon. *Phys. Rev.*, 103:51–61, 1956.

[37] R. A. Marcus. On the theory of oxidation-reduction reactions involving electron transfer. I. *J. Chem. Phys.*, 24(5):966–978, 1956. ISSN 00219606. doi: 10.1063/1.1742723.

[38] R. A. Marcus. Exchange Reactions and Electron Transfer Reactions Including. *Energy*, (i):21–31, 1960.

[39] A. Massé, P. Friederich, F. Symalla, F. Liu, R. Nitsche, R. Coehoorn, W. Wenzel, and P. A. Bobbert. \textit{Ab initio} charge-carrier mobility model for amorphous molecular semiconductors. *Phys. Rev. B*, 93(19):195209, 2016. doi: 10.1103/PhysRevB.93.195209. URL `http://link.aps.org/doi/10.1103/PhysRevB.93.195209`.

[40] F. May, B. Baumeier, C. Lennartz, and D. Andrienko. Can lattice models predict the density of states of amorphous organic semiconductors? *Phys. Rev. Lett.*, 109:1–5, 2012. ISSN 00319007. doi: 10.1103/PhysRevLett.109.136401.

[41] R. McNeill, R. Siudak, J. H. Wardlaw, and D. E. Weiss. Electronic conduction in polymers. I. The chemical structure of polypyrrole. *Aust. J. Chem.*, 16(6): 1056–1075, 1963. ISSN 14450038. doi: 10.1071/CH9631056.

[42] M. Mesta, M. Carvelli, R. J. de Vries, H. van Eersel, J. J. M. van der Holst, M. Schober, M. Furno, B. Lüssem, K. Leo, P. Loebl, R. Coehoorn, and P. A. Bobbert. Molecular-scale simulation of electroluminescence in a multilayer white organic light-emitting diode. *Nat. Mater.*, 12:652, 2013.

[43] O. V. Mikhnenko, F. Cordella, A. B. Sieval, J. C. Hummelen, P. W. M. Blom, and M. A. Loi. Temperature Dependence of Exciton Diffusion in Conjugated Polymers. *J. Phys. Chem. B*, 112:11601–11604, 2008. ISSN 1520-6106. doi: 10.1021/jp8042363. URL `http://pubs.acs.org/doi/abs/10.1021/jp8042363`.

[44] A. Miller and E. Abrahams. Impurity Conduction at Low Concentrations. *Phys. Rev.*, 120(3):745–755, 1960.

[45] J. R. Miller. Intramolecular Long-Distance Electron Transfer in Radical Anions. The Effects of Free Energy and Solvent on the Reaction Rates1. *J. Am. Chem. Soc.*, 106(10):3047–3049, 1984. ISSN 15205126. doi: 10.1021/ja00322a058.

[46] K. Mori, T. P. Goumans, E. Van Lenthe, and F. Wang. Predicting phosphorescent lifetimes and zero-field splitting of organometallic complexes with time-dependent density functional theory including spin-orbit coupling. *Phys. Chem. Chem. Phys.*, 16(28):14523–14530, 2014. ISSN 14639076. doi: 10.1039/c3cp55438d.

[47] N. F. Mott. On the transition to metallic conduction in semi-conductors. *Can. J. Phys.*, 34(12A):1356–1368, 1956. doi: 10.1139/p56-151. URL `https://doi.org/10.1139/p56-151`.

[48] T. Neumann, D. Danilov, C. Lennartz, and W. Wenzel. Modeling disordered morphologies in organic semiconductors. *J. Comput. Chem.*, 34(31):2716–2725, 2013. ISSN 1096-987X. doi: 10.1002/jcc.23445. URL `http://dx.doi.org/10.1002/jcc.23445`.

[49] Q. Peng, Q. Shi, Y. Niu, Y. Yi, S. Sun, W. Li, and Z. Shuai. Understanding the efficiency drooping of the deep blue organometallic phosphors: A computational study of radiative and non-radiative decay rates for triplets. *J. Mater. Chem. C*, 4(28):6829–6838, 2016. ISSN 20507526. doi: 10.1039/c6tc00858e.

[50] V. Rühle, A. Lukyanov, F. May, M. Schrader, T. Vehoff, J. Kirkpatrick, B. Baumeier, and D. Andrienko. Microscopic simulations of charge transport

in disordered organic semiconductors. *J. Chem. Theory Comput.*, 7(10):3335–3345, 2011. ISSN 15499618. doi: 10.1021/ct200388s.

[51] G. D. Scholes. Long range resonance energy transfer in molecular systems. *Annu. Rev. Phys. Chem.*, 54(1):57–87, 2003. ISSN 0066-426X. URL `http://www.annualreviews.org/doi/10.1146/annurev.physchem.54.011002.103746`.

[52] G. D. Scholes and K. P. Ghiggino. Rate expressions for excitation transfer I. Radiationless transition theory perspective. *J. Chem. Phys.*, 101(2):1251–1261, 1994. ISSN 00219606. doi: 10.1063/1.467817.

[53] G. Schönherr, R. Eiermann, H. Bässler, and M. Silver. Dispersive exciton transport in a hopping system with gaussian energy distribution. *Chem. Phys.*, 52: 287–298, 1980. ISSN 03010104. doi: 10.1016/0301-0104(80)85232-3.

[54] V. Stehr, R. F. Fink, M. Tafipolski, C. Deibel, and B. Engels. Comparison of different rate constant expressions for the prediction of charge and energy transport in oligoacenes. *Wiley Interdiscip. Rev. Comput. Mol. Sci.*, 6(6):694–720, 2016. ISSN 17590884. doi: 10.1002/wcms.1273.

[55] F. T. Zwischenmolekulare energiewanderung und fluoreszenz. *Ann. Phys.*, 437(1-2):55–75, 1948.

[56] C. W. Tang and S. A. Vanslyke. Organic electroluminescent diodes. *Appl. Phys. Lett.*, 51(12):913–915, 1987. ISSN 00036951. doi: 10.1063/1.98799.

[57] H. Uoyama, K. Goushi, K. Shizu, H. Nomura, and C. Adachi. Highly efficient organic light-emitting diodes from delayed fluorescence. *Nature*, 492(7428):234–238, 2012. ISSN 00280836. doi: 10.1038/nature11687. URL `http://dx.doi.org/10.1038/nature11687`.

[58] E. F. Valeev, V. Coropceanu, D. A. da Silva Filho, S. Salman, and J.-L. Brédas. Effect of electronic polarization on charge-transport parameters in molecular organic semiconductors. *J. Am. Chem. Soc.*, 128(30):9882–6, 2006. ISSN 0002-7863. doi: 10.1021/ja061827h. URL `http://www.ncbi.nlm.nih.gov/pubmed/16866546`.

[59] H. Van Eersel, P. A. Bobbert, R. A. Janssen, and R. Coehoorn. Monte Carlo study of efficiency roll-off of phosphorescent organic light-emitting diodes: Evidence for dominant role of triplet-polaron quenching. *Appl. Phys. Lett.*, 105(14), 2014. ISSN 00036951. doi: 10.1063/1.4897534.

[60] H. Van Eersel, P. A. Bobbert, R. A. Janssen, and R. Coehoorn. Effect of Förster-mediated triplet-polaron quenching and triplet-triplet annihilation on the efficiency roll-off of organic light-emitting diodes. *J. Appl. Phys.*, 119(16), 2016. ISSN 10897550. doi: 10.1063/1.4947457.

[61] H. Yang, Q. Zhou, J. Wang, C. Du, P. Song, and Y. Ding. Electron transfer and charge transport of photoelectric material in external electric field. *J. Lumin.*, 199(February):278–284, 2018. ISSN 00222313. doi: 10.1016/j.jlumin.2018.03.046. URL `https://doi.org/10.1016/j.jlumin.2018.03.046`.

[62] Z. G. Yu, D. L. Smith, A. Saxena, R. L. Martin, and A. R. Bishop. Molecular geometry fluctuation model for the mobility of conjugated polymers. *Phys. Rev. Lett.*, 84(4):721–724, 2000. ISSN 10797114. doi: 10.1103/PhysRevLett.84.721.

[63] W. Zhou, C. Zimmermann, and C. Jungemann. Master equation study of excitonic processes limiting the luminous efficacy in phosphorescent organic light-emitting diodes. *J. Appl. Phys.*, 125(16):165501, 2019. ISSN 0021-8979. doi: 10.1063/1.5082164. URL `http://aip.scitation.org/doi/10.1063/1.5082164`.

Chapter 2

Computational methods

In this chapter we discuss the different computational methods used in the rest of the thesis. We start from the molecular scale, by discussing the methods required to calculate the two factors in the FGR expression. These will include calculations of energies, molecular geometries, and the electronic energy Hessians and gradients using Density Functional Theory (DFT). We briefly discuss the calculation of the charge transfer integrals and the exciton transfer integrals following from Dexter and Förster theory. Then, we explain the calculation of the vibronic couplings and how they are used to calculate the Franck-Condon-weighted density of states. After this, we show how to upscale the molecular and microscopic calculations to the device scale. We introduce energetic, spatial and orientational disorder into a mescopic system at the device scale of around 10^6 molecules. Finally, we discuss the methods used to calculate the steady state and transient transport properties for both charges and excitons in a mesoscopic system.

2.1 Introduction

In this chapter we discuss the methods required to calculate charge and exciton transport properties. We start with the transfer rate between two molecules which is given by Fermi's Golden Rule

$$k = \frac{2\pi}{\hbar} J^2 \, \rho_{\mathrm{FC}}(\Delta E). \tag{2.1}$$

Both the transfer integrals J and the Franck-Condon weighted density of states ρ_{FC} in this equation will be calculated using Density Functional Theory (DFT) for charges and Time Dependent DFT (TD-DFT) for excitons. We will show how the transfer integrals for charges can be calculated from the HOMO and LUMO orbitals of the donor and acceptor molecules. The transfer integrals for excitons can be calculated from the excited state transition dipole moments within the Förster theory and from the triplet state orbitals within the Dexter theory.

In order to calculate ρ_{FC}, we need to obtain the vibronic couplings of the donor and acceptor molecules. For the electron and hole transfer the vibronic couplings are calculated using Density Functional Theory (DFT) within the spin-restricted framework in order to treat the cationic and anionic species of the molecules associated with the presence of an electron or hole, respectively, on the molecule. For the exciton transport we employ TD-DFT to find the vibronic coupling of the donor and acceptor excited states.

In the next step we find device transport properties like charge carrier mobilities and exciton diffusion lengths by taking the calculated transfer rates and applying those to a large system of molecules ($\approx 10^6$) where we introduce energetic, spatial and orientational disorder. We find the charge carrier mobilities of such systems by solving the Pauli Master Equation (ME), where we calculate the occupational probabilities of the carriers on the molecular sites. The exciton diffusion lengths are calculated using kinetic Monte Carlo (kMC), where we release excitons into the system one by one and follow their diffusion paths. We will discuss the advantages and disadvantages of both methods.

2.2 First-principles methods

In this work we use DFT as a tool to calculate the different molecular properties like LUMO, HOMO and triplet state energy levels, molecular geometries, transfer integrals, electronic energy Hessians and gradients . Though we do not develop a DFT code in this work we want to briefly introduce DFT.

The DFT method efficiently solves the time independent Schrödinger equation, yielding the molecular wave function. The molecular wave function is constructed from a set of atomic wave functions called the *basis set*, which is specified by the user. In DFT, the complex electron interactions leading to the exchange and correlation terms are included within the *functional*, which is parameterized. The TD-DFT

method allows for computation of excited states. In this work most of the DFT calculations are performed using the TURBOMOLE package [1]. The TD-DFT excited state calculations have all been performed using the ORCA package [9]. Within the ORCA package the spin-orbit coupling can be introduced into the TD-DFT method, so that the excited states are linear combinations of singlet and triplet excited states. This is important for the phosphorescent molecules studied in Chapters 4 and 5.

2.2.1 Transfer integrals

1) Charge transfer integrals

The transfer integrals for charge transfer can be calculated from the HOMO and LUMO wavefunctions of the donor and acceptor molecules. Using the method proposed by Valeev *et al.* [14] we can write the secular equation of the two state dimer system as

$$\begin{pmatrix} E_{\mathrm{D}} & J_{\mathrm{DA}} \\ J_{\mathrm{DA}} & E_{\mathrm{A}} \end{pmatrix} \begin{pmatrix} C_{\mathrm{D}} \\ C_{\mathrm{A}} \end{pmatrix} = E \begin{pmatrix} 1 & S_{\mathrm{DA}} \\ S_{\mathrm{DA}} & 1 \end{pmatrix} \begin{pmatrix} C_{\mathrm{D}} \\ C_{\mathrm{A}} \end{pmatrix}, \tag{2.2}$$

where

$$E_{\mathrm{D/A}} = \left\langle \phi_{\mathrm{D/A}} \right| H_{\mathrm{KS}} \left| \phi_{\mathrm{D/A}} \right\rangle, \quad J_{\mathrm{DA}} = \left\langle \phi_{\mathrm{D}} \right| H_{\mathrm{KS}} \left| \phi_{\mathrm{A}} \right\rangle \quad \text{and} \quad S_{\mathrm{DA}} = \left\langle \phi_{\mathrm{D}} | \phi_{\mathrm{A}} \right\rangle. \tag{2.3}$$

Here, ϕ_{D} and ϕ_{A} are the HOMO and LUMO orbitals of the donor and acceptor monomer, and H_{KS} is the DFT Kohn-Sham operator of the dimer system. One might think that we can now simply take J_{DA} as the transfer integral. However, this is the matrix element for the non-orthogonalized monomer orbitals ϕ_{D} and ϕ_{A}. The orthogonalized matrix elements can be obtained from the Löwdin orthogonalization procedure by

$$J_{\mathrm{DA}}^{\mathrm{eff}} = \frac{J_{\mathrm{DA}} - \frac{1}{2}(E_{\mathrm{D}} + E_{\mathrm{A}})S_{\mathrm{DA}}}{1 - S_{\mathrm{DA}}^2}. \tag{2.4}$$

The magnitude of the effective transfer integrals ($J_{\mathrm{DA}}^{\mathrm{eff}}$) is very dependent on the respective orientation and distance of the donor and acceptor monomers. This can be intuitively understood because the transfer integral is proportional to the wave function overlaps which have an exponential dependence on the donor acceptor distance [4]. It is therefore important to obtain the transfer integrals for a large set of donor acceptor pairs with a realistic distribution of orientations and distances. Later in this chapter we will discuss how to accurately scale the distribution of transfer integrals to mesoscopic systems at the device scale (10^6 molecules).

2) Exciton transfer integrals

Transfer integrals for excitons are more complicated to calculate because they consist of both long-range Coulomb contributions [12] and short-range exchange contributions [6]. The long-range contribution is often treated in the dipole-dipole approximation by

Förster theory, where the squared transfer integral has an R^{-6} distance dependence. The transfer integral within Förster theory is given by

$$J_{\mathrm{DA,Förster}} = \frac{1}{4\pi\epsilon_0\epsilon_\mathrm{r}} \frac{\kappa\mu_\mathrm{D}\mu_\mathrm{A}}{R^3}, \tag{2.5}$$

where μ_D and μ_A are the donor and acceptor transition dipole moments, and ϵ_r is the relative dielectric constant, which we choose to be $\epsilon_\mathrm{r} = 3$ in this thesis. The κ factor is related to the respective orientations of the dipoles and is given by [12]

$$\kappa = \vec{\mu}_\mathrm{D} \cdot \vec{\mu}_\mathrm{A} - 3(\vec{\mu}_\mathrm{D} \cdot \vec{R})(\vec{\mu}_\mathrm{A} \cdot \vec{R}). \tag{2.6}$$

For a system of molecules with random orientations the average value of κ^2 is 0.67. The only remaining parameters required for the calculation of the transfer integrals as a function of the donor-acceptor distance are the transition dipole moments. In this work these are calculated using TD-DFT.

The short-range Dexter contribution is taken to be equal to the direct exchange integral between the excited donor ($\mathrm{D}^*\mathrm{A}$) and the excited acceptor (DA^*) states [6]. We approximate this exchange integral by the overlap integral between the HOMO to HOMO and LUMO to LUMO transition densities [13]

$$\begin{aligned} J_{\mathrm{DA,Dexter}} \;=\; & \left\langle \Psi^{\mathrm{HOMO}}_{\mathrm{overlap}} \right| H \left| \Psi^{\mathrm{LUMO}}_{\mathrm{overlap}} \right\rangle \\ & \sum_{n,m} \left\langle \Psi^{\mathrm{HOMO}}_{\mathrm{D}} | n \right\rangle \left\langle \Psi^{\mathrm{HOMO}}_{\mathrm{A}} | n \right\rangle \langle n| H |m\rangle \left\langle m | \Psi^{\mathrm{LUMO}}_{\mathrm{D}} \right\rangle \left\langle m | \Psi^{\mathrm{LUMO}}_{\mathrm{A}} \right\rangle \end{aligned} \tag{2.7}$$

Here, $\Psi^{\mathrm{HOMO}}_{\mathrm{D}}$ ($\Psi^{\mathrm{LUMO}}_{\mathrm{D}}$) and $\Psi^{\mathrm{HOMO}}_{\mathrm{A}}$ ($\Psi^{\mathrm{LUMO}}_{\mathrm{A}}$) are the HOMO (LUMO) orbitals of the donor and acceptor. The indices n and m represent the excited states calculated with TD-DFT.

Previous studies have shown that contributions of intermediate charge transfer (CT) states of the type $\mathrm{D}^+\mathrm{A}^-$ or $\mathrm{D}^-\ \mathrm{A}^+$ can strongly enhance the transfer integral for Dexter coupling [16]. We add the contribution of intermediate CT states to the total transfer integral for Dexter coupling as described in Ref. [16]:

$$\begin{aligned} J_{\mathrm{DA,Dexter}} = \; & J_{\mathrm{DA,exchange,d}} \\ & + \frac{1}{2} \sum_{\mathrm{CT\ states}} J_{\mathrm{D,CT}} J_{\mathrm{CT,A}} \left[\frac{1}{E_{\mathrm{CT}} - E^{\mathrm{D}}_{\mathrm{T}}} - \frac{1}{E_{\mathrm{CT}} - E^{\mathrm{A}}_{\mathrm{T}}} \right], \end{aligned} \tag{2.8}$$

where the coupling integrals to the CT states are given by $J_{\mathrm{D,CT}}$ and $J_{\mathrm{CT,A}}$, and the energies of the donor and acceptor triplet and CT states by $E^{\mathrm{D}}_{\mathrm{T}}$, $E^{\mathrm{A}}_{\mathrm{T}}$ and E_{CT}, respectively.

3) Transfer integrals for multiple acceptor states

In Chapter 5 we will study exothermic exciton transfer. In such transfer the first excited state of the donor can be close to resonance with energetically higher excited states of the acceptor. In the introduction the assumption was made that the transfer integral only involves the coupling between one initial and one final electronic state. In the case of exothermic transfer this assumption is not valid anymore. The initial electronic state now couples to several final electronic states. Summing over all the electronically excited states, each having its own Franck-Condon-Weighted Density of stated (FCWD), yields the following rate

$$k_{\mathrm{DA}} = \sum_{i,j} p_{\mathrm{D}_i} \frac{2\pi}{\hbar} J_{ij}^2 \rho_{\mathrm{FC},ij}(\Delta E_{ij}) = \sum_{i,j} p_{\mathrm{D}_i} k_{\mathrm{D}_i\mathrm{A}_j}. \tag{2.9}$$

Here, the summation runs over all donor excited states i and acceptor excited states j. The donor excited states are occupied with a probability p_{D_i}. For most of the fluorescent molecules used in OLEDs, the first excited states will be well separated from the higher excited states with energy differences far exceeding $k_{\mathrm{B}}T$, which means that the sum can be restricted to the terms where $i = 1$. In the phosphorescent molecules studied in Chapter 5, the triplet states are split by the spin-orbit coupling with a splitting on the order of $k_{\mathrm{B}}T$. Therefore, we have to consider the first triplet manifold ($i = 1, 2, 3$) in the summation of Eq. 2.9 for these molecules. Notice that in Eq. 2.9 we have already separated the electronic and nuclear contributions similar to what was done in the Chapter 1. Each pair of electronic states then obtains its own FCWD $\rho_{\mathrm{FC},ij}$ and its own energy difference ΔE_{ij}.

2.2.2 Reorganization energy and vibronic couplings

1) Reorganization energy

In Marcus theory the vibronic activation of the transfer is described with a single molecular parameter called the reorganization energy (λ). A depiction of the classical harmonic approximation of the transfer is shown in Fig. 2.1. In this figure, the donor molecule that is charged (or excited) has a potential energy surface that is displaced with respect to the energy surface of the ground state. In a similar way, the potential energy surfaces of the acceptor ground and charged state are displaced with respect to each other. The displacement causes energy to be lost into vibrational modes of the system in every transfer process. This can be seen by the difference in length of the vertical arrows in the figure. The reorganization energy may be calculated from the potential energy surfaces using the four point procedure [10]. In the four point procedure we use DFT to calculate the energies at the four points indicated in the figure. The first point in the procedure is the relaxed ground state energy, the second point is the charged state energy in the ground state molecular geometry, the third point is the relaxed charged state energy, and the fourth point is the ground state

energy in the charged state geometry. The reorganization energy is then given by $\lambda = (E_2 - E_3) + (E_4 - E_1)$.

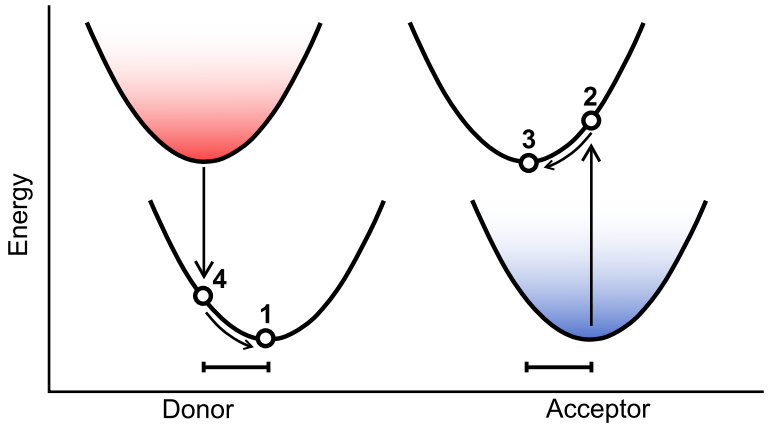

Figure 2.1: Schematic depiction of the donor and acceptor potential energy surfaces in the ground and charged/excited states. The reorganization energy associated with the Marcus transfer rate is the sum of the donor and acceptor relaxation as indicated by the arrow from point 4 to point 1 and point 2 to point 3.

2) Vibronic couplings

The vibronic couplings required for the calculation of the density of states are in this thesis obtained using the displaced harmonic oscillator model. This model assumes that the vibron energies and normal modes are the same for the neutral and charged or excited molecule. As a first step the Hessian matrix in mass-weighted coordinates ($\mathbf{H}$) is calculated and subsequently diagonalized to obtain the normal modes ($\mathbf{Q}$) and normal mode energies ω_i of the molecule. Within the displaced harmonic oscillator model the normal mode coordinates of the final electronic state ($\bar{\mathbf{Q}}$) are shifted by a displacement vector ($\mathbf{K}$) with respect to the initial state coordinates

$$\bar{\mathbf{Q}} = \mathbf{Q} - \mathbf{K}. \tag{2.10}$$

We can find the displacement vector from the diagonalized Hessian and the gradient of the final electronic state in the initial state geometry in mass-weighted coordinates ($\bar{\mathbf{g}}$) by taking a Newton's method step

$$\mathbf{K} = -\mathbf{H}^{-1}\bar{\mathbf{g}}. \tag{2.11}$$

The displacement vector is used to obtain the vibronic couplings (λ_i)

$$\lambda_i = \frac{1}{2} K_i^2 \omega_i^2, \tag{2.12}$$

with λ_i the vibronic coupling of the ith normal mode. The definition of initial state and final state is dependent on whether the molecule is the donor or acceptor in the transfer process. In this work the Hessian, gradient and geometries of the molecules are calculated using (TD-)DFT methods.

The magnitude of the vibronic couplings and vibron energies will be dependent on the unique molecular environment of the molecule in its morphology. This is why, for charges, we have developed a method to calculate the vibron energies and vibronic coupling of molecules embedded in the morphological environment. The details of the method and the results will be discussed in Chapter 3.

2.3 Calculation of the transfer rate

The transfer integral in the Fermi's Golden Rule transfer rate Eq. (2.1) is calculated as described in the last section. We now turn to the density of states $\rho_{\mathrm{FC}}(\Delta E)$. If we include all the intramolecular vibrations, also called vibrons, the Franck-Condon-weighted density of states becomes

$$\begin{aligned} \rho_{\mathrm{FC}}(\Delta E) \;=\; & \prod_i \sum_{n_i} p_{n_i} \sum_{\Delta n_i} \left| \langle \chi_{\mathrm{D}}^{\mathrm{i}} | \chi_{\mathrm{D}}^{\mathrm{f}} \rangle \right|_i^2 \times \prod_j \sum_{m_j} p_{m_j} \sum_{\Delta m_j} \left| \langle \chi_{\mathrm{A}}^{\mathrm{i}} | \chi_{\mathrm{A}}^{\mathrm{f}} \rangle \right|_j^2 \\ & \times \delta(\Delta E + \sum_i \Delta n_i \hbar\omega_i + \sum_j \Delta m_j \hbar\omega_j). \end{aligned} \tag{2.13}$$

This density of states is a sum over all the possible vibron occupations (n_i,m_j) and all possible vibron exchanges ($\Delta n_i, \Delta m_j$) of the vibron modes (i,j) belonging to the donor (i) and acceptor (j) molecule. The δ-function finally selects out only those terms that are in resonance with the actual energy difference (ΔE) between the donor and acceptor energy levels. The harmonic oscillator wavefunctions are given by $\chi_{\mathrm{D}}^{\mathrm{i}}$, $\chi_{\mathrm{D}}^{\mathrm{f}}$, $\chi_{\mathrm{A}}^{\mathrm{i}}$ and $\chi_{\mathrm{A}}^{\mathrm{f}}$ for the initial (i) and final (f) state of the donor (D) and acceptor (A). For a harmonic potential, the occupational probabilities (p_{n_i}) are

$$p_{n_i} = (1 - z_i) z_i^{n_i}, \;\; z_i = e^{-\hbar\omega_i / k_B T}. \tag{2.14}$$

The nuclear wavefunction overlaps are a function of the vibron occupation of the mode (n_i), the amount of vibrons exchanged (Δn_i) and the dimensionless vibronic coupling $\frac{\lambda_i}{\hbar\omega_i}$, which is a measure of the initial to final state displacement of the harmonic

oscillator wavefunctions

$$\left|\langle\chi^{\mathrm{i}}|\chi^{\mathrm{f}}\rangle\right|_i^2 = \exp\left[-\frac{\lambda_i}{\hbar\omega_i}\right]\left(\frac{\lambda_i}{\hbar\omega_i}\right)^{\Delta n_i}\frac{n_i!}{(n_i+\Delta n_i)!}\left[L_{n_i}^{\Delta n_i}\left(\frac{\lambda_i}{\hbar\omega_i}\right)\right]^2. \tag{2.15}$$

Here $L_{n_i}^{\Delta n_i}$ is the Laguerre polynomial. Using the following relation

$$\sum_n \frac{n![L_n^{\Delta n}(x)]^2 z^n}{(n+\Delta n)!} = \frac{x^{-\Delta n}\ z^{-\frac{\Delta n}{2}}}{1-z}e^{-2x\frac{z}{1-z}}\ \ I_{\Delta n}\left(2x\frac{\sqrt{z}}{1-z}\right), \tag{2.16}$$

we can rewrite the sum of occupational probabilities and wave function overlaps as a sum of Bessel functions $I_{\Delta n}$ over vibron exchanges

$$\sum_{n_i} p_{n_i}\sum_{\Delta n_i}\left|\langle\chi_{\mathrm{D}}^{\mathrm{i}}|\chi_{\mathrm{D}}^{\mathrm{f}}\rangle\right|_i^2 = \exp\left[-\frac{\lambda_i}{\hbar\omega_i}\frac{1+z_i}{1-z_i}\right]\sum_{\Delta n_i}\exp\left[\frac{\Delta n_i\hbar\omega_i}{2k_BT}\right]I_{\Delta n_i}\left[2\left(\frac{\lambda_i}{\hbar\omega_i}\right)\frac{\sqrt{z_i}}{1-z_i}\right]. \tag{2.17}$$

Applying this to all the vibron modes of the donor and acceptor we get

$$\begin{aligned}\rho_{\mathrm{FC}}(\Delta E) \;=\; & \prod_i\left(\exp\left[-\frac{\lambda_i}{\hbar\omega_i}\frac{1+z_i}{1-z_i}\right]\sum_{\Delta n_i}\exp\left[\frac{\Delta n_i\hbar\omega_i}{2k_BT}\right]I_{\Delta n_i}\left[2\left(\frac{\lambda_i}{\hbar\omega_i}\right)\frac{\sqrt{z_i}}{1-z_i}\right]\right)\times \\ & \prod_j\left(\exp\left[-\frac{\lambda_j}{\hbar\omega_j}\frac{1+z_j}{1-z_j}\right]\sum_{\Delta m_j}\exp\left[\frac{\Delta m_j\hbar\omega_j}{2k_BT}\right]I_{\Delta m_j}\left[2\left(\frac{\lambda_j}{\hbar\omega_j}\right)\frac{\sqrt{z_j}}{1-z_j}\right]\right)\times \\ & \delta(\Delta E+\sum_i\Delta n_i\hbar\omega_i+\sum_j\Delta m_j\hbar\omega_j).\end{aligned} \tag{2.18}$$

This expression is most easily solved by transformation to the time domain, where the δ-function becomes

$$\begin{aligned}& \delta(\Delta E+\sum_i\Delta n_i\hbar\omega_i+\sum_j\Delta m_j\hbar\omega_j) \qquad (2.19)\\ = \;& \frac{1}{2\pi\hbar}\int_{-\infty}^{\infty}dt\exp\left[i\left(\Delta E+\sum_i\Delta n_i\hbar\omega_i+\sum_j\Delta m_j\hbar\omega_j\right)t/\hbar\right],\end{aligned}$$

and we use the Jacobi-Anger identity

$$\sum_{\Delta n_i=-\infty}^{\infty}I_{\Delta n_i}(x)\exp(i\Delta n_i\theta) = \exp(x\cos\theta), \tag{2.20}$$

with $\theta=\omega_i t - i\hbar\omega/2k_BT$ and obtain

$$\rho_{\mathrm{FC}}(\Delta E) = \frac{1}{2\pi\hbar}\int_{-\infty}^{\infty} dt \exp\left[i\frac{\Delta E t}{\hbar} + \sum_i \frac{\lambda_i}{\hbar\omega_i}\left(\frac{1+z_i}{1-z_i}\left[\cos(\omega_i t) - 1\right] + i\sin(\omega_i t)\right)\right.$$
$$\left. + \sum_j \frac{\lambda_j}{\hbar\omega_j}\left(\frac{1+z_j}{1-z_j}\left[\cos(\omega_j t) - 1\right] + i\sin(\omega_j t)\right)\right]. \quad (2.21)$$

Finally, we use the relation

$$\coth\left(\frac{\hbar\omega_i}{2k_B T}\right) = \frac{1+z_i}{1-z_i}, \quad (2.22)$$

to obtain

$$\rho_{\mathrm{FC}}(\Delta E) = \frac{1}{2\pi\hbar}\int_{-\infty}^{\infty} dt \exp\left[i\frac{\Delta E t}{\hbar}\right.$$
$$+ \sum_i \frac{\lambda_i}{\hbar\omega_i}\left(\coth\left(\frac{\hbar\omega_i}{2k_B T}\right)\left[\cos(\omega_i t) - 1\right] + i\sin(\omega_i t)\right)$$
$$\left. + \sum_j \frac{\lambda_j}{\hbar\omega_j}\left(\coth\left(\frac{\hbar\omega_j}{2k_B T}\right)\left[\cos(\omega_j t) - 1\right] + i\sin(\omega_j t)\right)\right]. \quad (2.23)$$

Solving the integral in Eq. (2.23) numerically can be problematic. This is because for some values of ΔE there is no combination of the vibron mode transitions that is in exact resonance. Physically, this would be unrealistic because there are always some weakly coupling vibrational modes that can assist in creating the resonance condition. These can be for example intermolecular vibrational modes. If we assume that such modes have small frequencies and can be treated classically ($\hbar\omega_{\mathrm{cl}} \ll k_{\mathrm{B}}T$), then we can use the following approximations in Eq. (2.23):

$$\cos(\omega_{\mathrm{cl}} t) \approx 1 - (\omega_{\mathrm{cl}} t)^2/2 \ \text{ and } \ \sin(\omega_{\mathrm{cl}} t) \approx \omega_{\mathrm{cl}} t. \quad (2.24)$$

If we insert this into Eq. (2.23) we get

$$\rho_{\mathrm{FC}}(\Delta E) = \frac{1}{2\pi\hbar}\int_{-\infty}^{\infty} dt \exp\left[i\frac{(\Delta E + \lambda_{\mathrm{cl}})t}{\hbar} - \frac{\lambda_{\mathrm{cl}} k_{\mathrm{B}} T t^2}{\hbar^2}\right.$$
$$+ \sum_i \frac{\lambda_i}{\hbar\omega_i}\left(\coth\left(\frac{\hbar\omega_i}{2k_B T}\right)\left[\cos(\omega_i t) - 1\right] + i\sin(\omega_i t)\right)$$
$$\left. + \sum_j \frac{\lambda_j}{\hbar\omega_j}\left(\coth\left(\frac{\hbar\omega_j}{2k_B T}\right)\left[\cos(\omega_j t) - 1\right] + i\sin(\omega_j t)\right)\right]. \quad (2.25)$$

The small Gaussian broadening induced by $\lambda_{\rm cl}$ significantly facilitates the numerical integration, allowing all the ΔE values to be computed. In Chapter 3 we will show that if $\lambda_{\rm cl}$ is chosen sufficiently small, its influence on the magnitude of the transfer rate is negligible.

In Chapters 3 and 4 we will look at transfer between like molecules. In such cases the FCWD expression can be simplified because $\omega_j = \omega_i$ and $\lambda_j = \lambda_i$. We can then write

$$\begin{aligned}\rho_{\rm FC}(\Delta E) &= \frac{1}{2\pi\hbar}\int_{-\infty}^{\infty} dt \exp\left[i\frac{(\Delta E+\lambda_{\rm cl})t}{\hbar} - \frac{\lambda_{\rm cl}k_{\rm B}Tt^2}{\hbar^2}\right. \\ &\left. + \sum_i 2\frac{\lambda_i}{\hbar\omega_i}\left(\coth\left(\frac{\hbar\omega_i}{2k_BT}\right)\left[\cos(\omega_i t)-1\right] + i\sin(\omega_i t)\right)\right]. \quad (2.26)\end{aligned}$$

A convenient single vibron mode expression for the low temperature limit of $\rho_{\rm FC}$ can be obtained starting from the wavefunction overlaps Eq. (2.15) and assuming that the vibron mode is not thermally occupied $n = 0$

$$\rho_{\rm FC,eff}(\Delta E) = \exp\left(-\frac{\lambda_{\rm eff}}{\hbar\omega_{\rm eff}}\right)\sum_{\Delta n}\frac{(\lambda_{\rm eff}/\hbar\omega_{\rm eff})^{\Delta n}}{n!}\delta(\Delta E + \Delta n\hbar\omega_{\rm eff}) \quad (2.27)$$

Here, $\lambda_{\rm eff}$ is the single mode vibron coupling and equal to the reorganization energy within the Marcus theory, $\hbar\omega_{\rm eff}$ is the single mode vibron energy. This expression is similar to the Marcus-Levich-Jortner (MLJ) expression, where in the MLJ expression, the δ-function is replaced by a Gaussian broadening with classical reorganization energy $\lambda_{\rm cl}$. From Eq. (2.27) we exploit the δ-function to insert $\Delta n = \Delta E/\hbar\omega_{\rm eff}$ and write

$$\begin{aligned}\rho_{\rm FC,eff}(\Delta E) = \frac{1}{\hbar\omega_{\rm eff}}\frac{\exp(-S_{\rm eff})}{\Gamma\left(\Delta E/\hbar\omega_{\rm eff}+1\right)}\exp\left(\frac{\Delta E\ \ln(S_{\rm eff})}{\hbar\omega_{\rm eff}}\right) \\ \exp\left(-\frac{\Delta E+|\Delta E|}{2k_BT}\right).\end{aligned} \quad (2.28)$$

Here, $S_{\rm eff} = \lambda_{\rm eff}/\hbar\omega_{\rm eff}$ and the last factor is added to satisfy detailed balance. This equation will be used in Chapter 4 to approximate the full vibron rate using $S_{\rm eff}$ and $\hbar\omega_{\rm eff}$ as fitting parameters.

In Chapter 5 we study the transfer between different molecules. Starting from Eq. (2.23), we write the Franck-Condon-weighted density of states as a spectral overlap of the donor and acceptor vibronic spectra. To show this, we use $\Delta E = E_{\rm A} - E_{\rm D}$ to write

$$\rho_{\rm FC} = \frac{1}{2\pi\hbar}\int_{-\infty}^{\infty} dt \exp\left[i\frac{(E-E_{\rm D})t}{\hbar}\right]I_{\rm D}(t)\times\exp\left[i\frac{(E_{\rm A}-E)t}{\hbar}\right]I_{\rm A}(t), \quad (2.29)$$

with

$$I_{\mathrm{D}}(t) = \exp\left[\sum_i \frac{\lambda_i}{\hbar\omega_i}\left(\coth\left(\frac{\hbar\omega_i}{2k_BT}\right)\left[\cos(\omega_i t) - 1\right] + i\sin(\omega_i t)\right)\right], \tag{2.30}$$

and

$$I_{\mathrm{A}}(t) = \exp\left[\sum_j \frac{\lambda_j}{\hbar\omega_j}\left(\coth\left(\frac{\hbar\omega_j}{2k_BT}\right)\left[\cos(\omega_j t) - 1\right] + i\sin(\omega_j t)\right)\right]. \tag{2.31}$$

Now using the convolution theorem

$$\mathcal{F}\{f \cdot g\} = \mathcal{F}\{f\} * \mathcal{F}\{g\}, \tag{2.32}$$

we can write

$$\rho_{\mathrm{FC}} = \int I_{\mathrm{D}}(E) I_{\mathrm{A}}(E) dE, \tag{2.33}$$

with

$$I_{\mathrm{D}}(E) = \frac{1}{2\pi\hbar}\int_{-\infty}^{\infty} dt \exp\left[i\frac{(E - E_{\mathrm{D}})t}{\hbar}\right] I_{\mathrm{D}}(t), \tag{2.34}$$

and

$$I_{\mathrm{A}}(E) = \frac{1}{2\pi\hbar}\int_{-\infty}^{\infty} dt \exp\left[i\frac{(E_{\mathrm{A}} - E)t}{\hbar}\right] I_{\mathrm{A}}(t). \tag{2.35}$$

The deconvolution of ρ_{FC} into the donor and acceptor spectra will be useful when we want to interpret the effect of combining different donor and acceptor molecules, as is done in Chapter 5.

2.4 Simulating the disorder

In this section we introduce the methods required to calculate the spatial, orientational and energetic disorder. We start by explaining how the morphologies are obtained, which contain the spatial and orientational disorder of the molecular materials. The orientational disorder determines the disorder in the transfer integrals, and we discuss how this disorder is stochastically approximated. Finally, we will briefly discuss how the energetic disorder is calculated for the molecules in the disordered morphologies.

2.4.1 Spatial disorder

The microscopic morphologies used in this work are calculated using the DEPOSIT simulation code [11]. The code models the deposition and geometric relaxation of molecules on a surface, thereby mimicking the vapor deposition process often used to grow the organic layers in OLEDs. The microscopic morphologies generated consist

of around 10^3 molecules and are therefore not large enough to capture the percolative nature of the carrier transport [8]. In this work we employ two methods to upscale the microscopic morphologies to the device (10^6 molecules) scale.

1) Dominance competition point placement

The first method used in this work to upscale the morphologies has been developed by Baumeier *et al.* [2]. The method is based on a dominance-competition point-placement model that relies on the thinning of a Poisson process. The method starts out with an empty simulation box. Subsequently, uniformly generated points (representing the center-of-mass of the molecules) are added to the box. Once enough points are added, the dominance-competition process is used to thin out the morphology and make sure that there is a significant distance between the molecules. This process is repeated until the desired density of the morphology is reached. The result of this procedure can be compared with the microscopic morphologies by looking at, for example, the radial distribution function (RDF) or the nearest-neighbor distribution function (NNDF). The method reproduces the distribution of the molecules quite well for molecules that have a rather anisotropic shape, i.e. non-spherical molecules. However, we have found that if the molecules are more spherically shaped, like most of the iridium emitters studied in this work, the model does not correctly reproduce the RDF and NNDF of the morphology. This can already be seen by looking at a 0.7 nm thick cross section of a morphology of the host-guest system of the iridium emitter $Ir(ppy)_3$ in 4,4'-Bis(*N*-carbazolyl)-1,1'-biphenyl (CBP) as illustrated in Fig. 2.2.

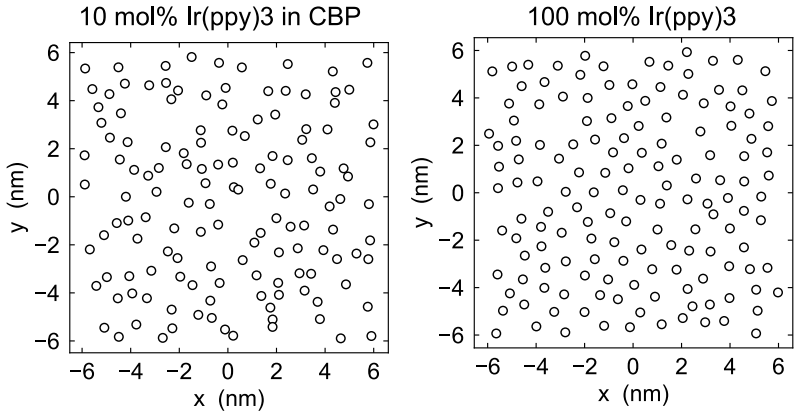

Figure 2.2: Left: 0.7 nm cross section of a morphology of 10 mol% $Ir(ppy)_3$ in CBP, the variation in center-of-mass distance in this morphology is quite large. Right: 0.7 nm cross section of a morphology of the $Ir(ppy)_3$ neat film, the morphology shows very evenly distributed centers-of-masses.

The CBP molecules are quite anisotropically shaped and determine the distribution of the molecules in the host-guest system. The cross section of the host-guest system Fig. 2.2 clearly shows much more variation in the center-of-mass distances, while the molecules in the neat film of $Ir(ppy)_3$ are evenly distributed. The stochastic nature of the point-placement method by Baumeier *et al.* makes it difficult to reproduce the distribution found in the $Ir(ppy)_3$ neat film. This is because the close packing in the neat film does not allow for many points to be added after a first morphology has been established. It is therefore difficult to reach the desired density, and the procedure becomes too time demanding. Therefore, we propose another method.

2) Disordered lattice Monte Carlo

Intuitively it seems more logical to start from a more ordered state to reproduce the neat film morphology displayed in Fig 2.2. For this we take a hard-sphere packing morphology. A schematic of the resulting method is given in Fig. 2.3.

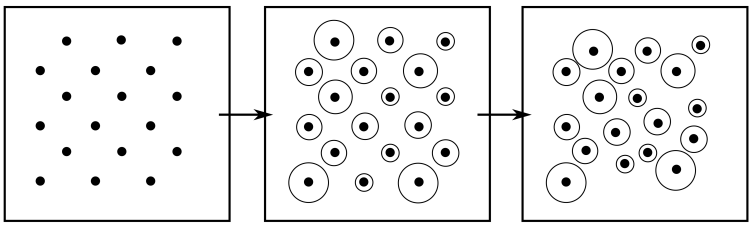

Figure 2.3: Schematic representation of the morphology expansion method for ordered morphologies: (1) face centered cubic lattice generation, (2) assignment of a radius r_i for each molecule i, and (3) application of an iterative Monte Carlo algorithm that leads to a stochastic mesoscopic distribution of points resembling the microscopic distribution function of the molecular centers-of-masses.

First (1), a face centered cubic lattice with a density equal to the microscopic morphology is generated. Each lattice point represents the center-of-mass of a molecule. Then (2), each point (i) in the lattice is assigned a radius (r_i), chosen randomly from a normal distribution with an average μ_r and a standard deviation σ_r. After this preparation procedure, an iterative Monte Carlo algorithm is started (3), from which for optimized values of μ_r and σ_r a mesoscopic morphology is obtained with a RDF that closely resembles that of the microscopic morphology:

1. A point i with position $\vec{p}_i$ is randomly chosen out of all N points, with initial position vectors $P = \{\vec{p}_1, .., \vec{p}_i, .., \vec{p}_N\}$.

2. A random displacement $\vec{d}$ is chosen with $\vec{d} = \alpha(R_x\hat{x} + R_y\hat{y} + R_z\hat{z})$. Here, R_x, R_y, and R_z are random numbers in the range $\{-1, 1\}$, and α is an adjustable parameter.

3. Distances $r_{ij} = |\vec{p'}_i - \vec{p_j}|$ from the new point with position $\vec{p'}_i = \vec{p}_i + \vec{d}$ to all other points j are calculated.

4. The new position of point i is accepted if $r_{ij} > r_i$ and $r_{ij} > r_j$.

5. Steps 1 to 4 are repeated until the RDF of the stochastic mesoscopic morphology resembles most closely the RDF of the microscopic morphology.

6. Steps 1 to 5 are repeated systematically for other values of the parameter set $\{\mu_r, \sigma_r\}$, until a set $\{\mu_r, \sigma_r\}$ is obtained that leads to a RDF and NNDF of the stochastic mesoscopic morphology that optimally resemble those of the microscopic morphology.

2.4.2 Transfer integral disorder

As mentioned in section 2.2, the transfer integrals are strongly dependent on the mutual orientation of the donor acceptor pairs. In order to get a fair representation of the distribution of the transfer integrals, they are calculated for a large amount of molecular pairs drawn from a microscopic morphology of around 10^3 molecules generated using the DEPOSIT code. We thus obtain a large set of squared transfer integrals (J^2) as a function of donor acceptor distance (R_{DA}), as depicted in Fig. 2.4.

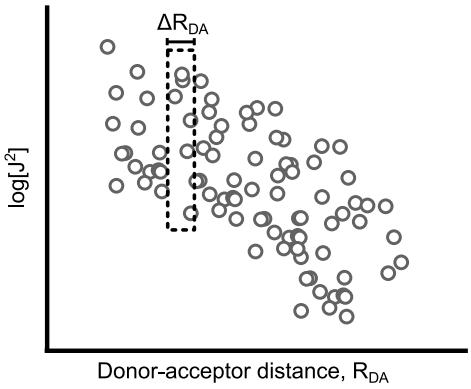

Figure 2.4: Schematic depiction of the transfer integral cloud obtained from the microscopic calculation, and the stochastic binning method used to extrapolate the cloud to the device scale system.

In order to extrapolate to the device scale, we first separate the transfer integral cloud into bins with distance intervals (ΔR_{DA}). Within each distance interval there is a distribution of transfer integrals due to the difference in orientations of the donor acceptor pairs. We now stochastically approximate the transfer integral distribution within the bin by fitting it with a Gaussian. The transfer integrals in the mesoscopic systems are now assigned by first finding the right distance bin and then picking a transfer integral from the fitted Gaussian belonging to that bin.

2.4.3 Energetic disorder

The energetic disorder of the charged and excited state energy levels in the mesoscopic system is described by a Gaussian distribution with disorder parameter σ. The disorder parameter is obtained by calculating the energy levels for a large set of molecules

in the microscopic system and fitting a Gaussian distribution to the energies. For the electrons, holes and triplets the energies are obtained as from the LUMO, HOMO and spin-restricted triplet state energies, respectively, of the molecules using DFT. The effect of the environment of the molecule on the energies is taken into account using the QUANTUM PATCH method. In this method the polarizability of the local environment of the molecule is described by point charges that are iteratively updated per molecule using DFT [5]. The long-range electrostatic interactions are taken into account by static point charges.

2.5 Transport simulations

2.5.1 Charge transport

With the steps described in the last subsection the transport network is generated from the mesoscopic morphology, energetic disorder and transfer integrals, while the rates between all the transport sites (molecules) are calculated using the FGR expression (Eq. 2.1). In the case of charge transport we are interested in the steady state charge transport properties. The charge carrier mobility can be calculated efficiently by setting up and numerically solving the time-dependent Pauli Master Equation (ME). The ME describes the time evolution of the charge carrier occupation probabilities p_i

$$\frac{dp_i}{dt} = \sum_j [k_{ji} p_j (1 - p_i) - k_{ij} p_i (1 - p_j)]. \tag{2.36}$$

In this equation the sum runs over all neighbouring sites j of site i, with k_{ji} the transfer rate from site j to i and k_{ij} from i to j. Here the factor $(1 - p_j)$ ensures that a site can not be occupied by more than one carrier as a consequence of the strong on-site Coulomb repulsion. Coulomb interactions of carriers on different sites are neglected in this method. For the carrier densities studied in this work ($< 10^{-4}$ per molecule) such an approximation is valid [7]. The steady-state ME is solved for $\frac{dp_i}{dt} = 0$ by using Yu's method [17]. In this method the initial occupational probabilities are chosen as

$$p_i = \frac{1}{1 + \exp([E_i - \mu_i]/k_B T)}, \tag{2.37}$$

and $\mu_i = E_\mathrm{F}$, with E_F the Fermi energy and E_i the on site energies drawn from the energetic disorder. From this initial occupational probability the probabilities are updated using

$$p_i = 1/\left[1 + \frac{\sum_j k_{ij}(1 - p_j)}{\sum_j k_{ji} p_j}\right]. \tag{2.38}$$

The updated probabilities are then again inserted in Eq. (2.38), this process is repeated until convergence is achieved. The problem with the Yu method is that at

large electric field, far from equilibrium, the carrier concentration is not conserved from one iteration to the next. To solve this problem we calculate the electrochemical potential μ_i after convergence using Eq. (2.37). Next, the μ_i values are shifted such that the original carrier concentration is obtained. From the converged result the current density is found by

$$J = \frac{e}{V} \sum_{ij} k_{ij} p_i (1 - p_j) R_{ij,x}, \tag{2.39}$$

where V is the volume of the system and $R_{ij,x}$ is the spatial separation of sites i and j in the x-direction.

While Yu's method is able to efficiently calculate the steady state transport properties, it does not allow calculation of transient properties. To simulate the transient behaviour we have to solve the Master Equation for consecutive time-steps. For this we use the implicit Euler method

$$\frac{p_i^{[n]} - p_i^{[n-1]}}{\Delta t^{[n]}} = \sum_j \left[k_{ji} p_j^{[n]} (1 - p_i^{[n]}) - k_{ij} p_i^{[n]} (1 - p_j^{[n]}) \right]. \tag{2.40}$$

For every consecutive time step n we then need to solve the equation

$$g_i = \frac{p_i^{[n]} - p_i^{[n-1]}}{\Delta t^{[n]}} - \sum_j \left[k_{ji} p_j^{[n]} (1 - p_i^{[n]}) - k_{ij} p_i^{[n]} (1 - p_j^{[n]}) \right] = 0. \tag{2.41}$$

We solve this equation using Newton's method

$$\mathbf{\Delta p} = \mathbf{J^{-1} g}, \tag{2.42}$$

where $\mathbf{\Delta p}$ is the step in the probability vector $\mathbf{p}^{[n]}$, which will go to zero after several iterations. The Jacobian matrix elements are given by

$$J_{ii} = 1/\Delta t^{[n]} + \sum_m k_{im} (1 - p_m^{[n]}) + k_{mi} p_m^{[n]} \tag{2.43}$$

$$J_{ij} = -k_{ij} p_i^{[n]} - k_{ji} (1 - p_i^{[n]}). \tag{2.44}$$

In the solver we now add an equation to make sure that the carrier concentration is conserved in the Newton iterations:

$$\sum_i \Delta p_i = 0. \tag{2.45}$$

The system of equations is finally solved using the PARDISO solver [3, 15].

2.5.2 Exciton transport

In the case of exciton transport we are following the time evolution of a single exciton. We could in principle use the Pauli Master Equation method introduced in the last subsection. However, for exciton transfer may neighbouring sites need to be included in order to model the long-range Förster transfer properly. Due to the large amount of neighbours it becomes difficult to store the Jacobian matrix, making the solver ineffective. Luckily, the motion of a single exciton can be very efficiently studied by the Kinetic Monte Carlo (KMC) method. We therefore choose to use a KMC simulation to study exciton diffusion. We use the KMC to study single excitons with a lifetime τ. The method works as follows:

1 An exciton is placed randomly on one of the guest sites within the simulation box.

2. The rates for the transfer events (k_{ij}) from the initial position (i) to all possible neighbouring sites (j) are calculated.

3. By comparing the rates to a uniform random number (R_1) multiplied by the sum over all rates $k_{\mathrm{tot}} = \sum_j k_{ij}$, a transfer or decay event is chosen.

4. The total simulation time is advanced by another random number (R_2) divided by the log of the sum over all rates: $\Delta t = R_2/\ln(k_{\mathrm{tot}})$.

5. Steps 2-4 are repeated until the exciton has decayed.

From the statistics of exciton decays a diffusion length calculated. The probability (P) distribution of diffusion distances is given by

$$P(|x|) = \frac{1}{2L_{\mathrm{D,1D}}} \exp\left[\frac{|x|}{L_{\mathrm{D,1D}}}\right], \tag{2.46}$$

with $|x|$ the absolute 1D displacement of the exciton from its initial position to its final position. The 3D diffusion length L_{D} is obtained as $L_{\mathrm{D}} = \sqrt{3}L_{\mathrm{D,1D}}$.

Bibliography

[1] R. Ahlrichs, M. Bär, M. Häser, H. Horn, and C. Kölmel. Electronic structure calculations on workstation computers: The program system turbomole. *Chem. Phys. Lett.*, 162(3):165–169, 1989. ISSN 0009-2614. doi: http://dx.doi.org/10.1016/0009-2614(89)85118-8. URL `http://www.sciencedirect.com/science/article/pii/0009261489851188`.

[2] B. Baumeier, O. Stenzel, C. Poelking, D. Andrienko, and V. Schmidt. Stochastic modeling of molecular charge transport networks. *Phys. Rev. B*, 86(18):184202, nov 2012. doi: 10.1103/PhysRevB.86.184202. URL `http://link.aps.org/doi/10.1103/PhysRevB.86.184202`.

[3] A. De Coninck, B. De Baets, D. Kourounis, F. Verbosio, O. Schenk, S. Maenhout, and J. Fostier. Needles: Toward Large-Scale Genomic Prediction with Marker-by-Environment Interaction. 203(1):543–555, 2016. ISSN 0016-6731. doi: 10.1534/genetics.115.179887. URL `http://dx.doi.org/10.1534/genetics.115.179887`.

[4] D. L. Dexter. A theory of sensitized luminescence in solids. *J. Chem. Phys.*, 21 (5):836–850, 1953. ISSN 00219606. doi: 10.1063/1.1699044.

[5] P. Friederich, F. Symalla, V. Meded, T. Neumann, and W. Wenzel. Ab Initio Treatment of Disorder Effects in Amorphous Organic Materials: Toward Parameter Free Materials Simulation. *J. Chem. Theory Comput.*, 10(9):3720–3725, 2014.

[6] R. D. Harcourt, G. D. Scholes, and K. P. Ghiggino. Rate expressions for excitation transfer. II. Electronic considerations of direct and through-configuration exciton resonance interactions. *J. Chem. Phys.*, 101(12):10521–10525, 1994. ISSN 00219606. doi: 10.1063/1.467869.

[7] F. Liu, H. Van Eersel, B. Xu, J. G. Wilbers, M. P. De Jong, W. G. Van Der Wiel, P. A. Bobbert, and R. Coehoorn. Effect of Coulomb correlation on charge transport in disordered organic semiconductors. *Phys. Rev. B*, 96(20):205203, 2017. ISSN 24699969. doi: 10.1103/PhysRevB.96.205203.

[8] A. Massé, R. Coehoorn, and P. A. Bobbert. Universal Size-Dependent Conductance Fluctuations in Disordered Organic Semiconductors. *Phys. Rev. Lett.*, 113(11):116604, sep 2014. doi: 10.1103/PhysRevLett.113.116604. URL `http://link.aps.org/doi/10.1103/PhysRevLett.113.116604`.

[9] F. Neese. Software update: the ORCA program system, version 4.0. *Wiley Interdiscip. Rev. Comput. Mol. Sci.*, 8(1):4–9, 2018. ISSN 17590884. doi: 10.1002/wcms.1327.

[10] S. F. Nelsen, S. C. Blackstock, and Y. Kim. Estimation of inner shell Marcus terms for amino nitrogen compounds by molecular orbital calculations. *J. Am. Chem. Soc.*, 109(3):677–682, 1987. ISSN 0002-7863. doi: 10.1021/ja00237a007.

[11] T. Neumann, D. Danilov, C. Lennartz, and W. Wenzel. Modeling disordered morphologies in organic semiconductors. *J. Comput. Chem.*, 34(31):2716–2725, 2013. ISSN 1096-987X. doi: 10.1002/jcc.23445. URL `http://dx.doi.org/10.1002/jcc.23445`.

[12] G. D. Scholes. Long range resonance energy transfer in molecular systems. *Annu. Rev. Phys. Chem.*, 54(1):57–87, 2003. ISSN 0066-426X. URL `http://www.annualreviews.org/doi/10.1146/annurev.physchem.54.011002.103746`.

[13] F. Symalla, S. Heidrich, P. Friederich, T. Strunk, T. Neumann, D. Minami, D. Jeong, and W. Wenzel. Multiscale simulation of photoluminescence quenching in phosphorescent OLED materials. (submitted).

[14] E. F. Valeev, V. Coropceanu, D. A. da Silva Filho, S. Salman, and J.-L. Brédas. Effect of electronic polarization on charge-transport parameters in molecular organic semiconductors. *J. Am. Chem. Soc.*, 128(30):9882–6, 2006. ISSN 0002-7863. doi: 10.1021/ja061827h. URL `http://www.ncbi.nlm.nih.gov/pubmed/16866546`.

[15] F. Verbosio, A. D. Coninck, D. Kourounis, and O. Schenk. Enhancing the scalability of selected inversion factorization algorithms in genomic prediction. *J. Comput. Sci.*, 22(Supplement C):99–108, 2017. ISSN 1877-7503. URL `https://doi.org/10.1016/j.jocs.2017.08.013`.

[16] J. Wehner and B. Baumeier. Intermolecular Singlet and Triplet Exciton Transfer Integrals from Many-Body Green's Functions Theory. *J. Chem. Theory Comput.*, 13(4):1584–1594, 2017. ISSN 15499626. doi: 10.1021/acs.jctc.6b00935.

[17] Z. G. Yu, D. L. Smith, A. Saxena, R. L. Martin, and A. R. Bishop. Molecular geometry fluctuations and field-dependent mobility in conjugated polymers. *Phys. Rev. B*, 63(8):85202, 2001.

Chapter 3

Full quantum treatment of charge dynamics in amorphous molecular semiconductors

In Chapter 2 we have introduced the Fermi's Golden Rule rate and the different methods necessary to apply the rate to realistic disorder and find the charge transport properties.

In this chapter we show the results of the single mode FGR rate as a function of vibron-coupling strength and vibron mode energy. We then calculate for three common OLED host materials (α-NPD, TCTA and spiro-DPVBi), the actual vibron modes and couplings using first-principles methods. The effect of the molecular environment on the coupling strength and mode energy is investigated by looking at a set of 20 molecules, each having its own unique environment, drawn from a microscopic morphology. The calculated rates are then applied to realistic energetic spatial and orientational disorder to calculate electron and hole mobilities for the three molecules. We look at the electric field and temperature dependence and find that at low temperatures the Marcus theory deviates significantly from the correct FGR treatment. Interestingly the Miller-Abrahams theory seems to describe the temperature dependence of the mobility more correctly. Finally, we look at the charge dynamics by following a carrier concentration as it relaxes from the center of the density of states to the equilibrated average energy. In the dynamics we see very little difference between the FGR, Marcus and MA models.

This work has been published: X. de Vries, P. Friederich, W. Wenzel, R. Coehoorn and P.A. Bobbert, Phys. Rev. B 97, 075203 (2018).

3.1 Introduction

Amorphous polymeric and molecular organic semiconductors are crucial compounds used in organic devices such as organic field-effect transistors (OFETs), organic photovoltaic (OPV) cells, and organic light-emitting diodes (OLEDs). The modeling of charge dynamics in these materials is essential for the further development of organic devices. Systematic modeling started with the work of Bässler in the nineteen-nineties [4]. It was assumed that due to the disorder the charge carriers are localized and hop non-adiabatically between localization sites by phonon-assisted tunneling, or "hopping". In the early studies use was made of the Miller-Abrahams (MA) hopping rate [20], $k_{\rm MA} = k_0$ if $\Delta E < 0$ and $k_{\rm MA} = k_0 \exp(-\Delta E/k_{\rm B}T)$ if $\Delta E > 0$, where ΔE is the electronic energy change, T temperature, $k_{\rm B}$ Boltzmann's constant, and k_0 a prefactor proportional to the square of the electronic coupling J between the sites, assumed to decay exponentially with intersite distance. The advantage of using the MA rate is its simplicity: no material-specific information is needed for describing the energy dependence of the rate. It was established that the strength of the energetic disorder, modeled by a Gaussian density of states (DOS), plays a central role, both for the steady-state mobility and energetic relaxation of charge carriers [4]. The resulting model is known as the Gaussian Disorder Model (GDM). It was later realized that filling of the DOS by only a small fraction of carriers can already strongly increase the charge-carrier mobility [27, 24, 3], requiring an extension of the GDM [23].

Present-day commercial OLEDs make use of amorphous molecular organic semiconductors. The theoretical advantage of considering molecular instead of polymeric semiconductors is that the localization sites are clearly defined: they coincide with the molecules. Recently, several groups made progress in evaluating charge dynamics in these materials from explicit calculations of the morphology, the on-site energies, the intermolecular electronic couplings, and the molecular reorganization energy λ [13, 25, 12, 10]. Use was made of the semiclassical Marcus hopping rate [15]

$$k_{\rm Marcus} = \frac{2\pi}{\hbar}\frac{J^2}{\sqrt{4\pi\lambda k_{\rm B}T}}\exp\left[-\frac{(\Delta E+\lambda)^2}{4\lambda k_{\rm B}T}\right]. \tag{3.1}$$

In Marcus theory, the coupling of the vibrons (intramolecular vibrations) to the charge is treated classically, which means that Eq. (3.1) is only valid if the vibron energy $\hbar\omega_i \ll k_{\rm B}T$ for all modes i. Because of the π-conjugation, intramolecular modes involving carbon-carbon bond vibrations couple strongly to the charges. These modes have typical energies in the range 0.1-0.2 eV, i.e., almost one order of magnitude larger than $k_{\rm B}T$ at room temperature, invalidating a semiclassical approach and the use of Eq. (3.1). It is of paramount importance to study the consequences of going beyond the semiclassical approximation by including the charge-vibron coupling fully quantum mechanically and to provide benchmark results for the charge dynamics that do no suffer from uncontrolled approximations. This is the goal of this chapter.

While Eq. (3.1) predicts a vanishing conductivity in the limit $T \to 0$, a quantum

treatment of the vibron modes, accounting for nuclear tunneling through a classically forbidden region of nuclear arrangements accompanying the charge transfer, explains the observed finite conductivity in this limit in chemically doped in-plane diodes and ferroelectric field-effect transistors of amorphous semiconducting polymers [2]. In a recent study of low-energy tails of external quantum efficiency (EQE) spectra of OPV cells of C_{60} mixed with different donor molecules, a failure of the application of Eq. (3.1) in describing the EQE tails was attributed to quantum mechanical freeze-out of high-energy vibrons [29]. These two examples point at the importance of considering the quantum character of vibrons in studying charge dynamics. We note that the impact of a full quantum treatment of vibron modes on charge transport has been considered for organic crystals [21], but, as far as we know, not yet for amorphous molecular semiconductors, where the percolative nature of the charge transport [7] adds an additional important complexity.

The chapter is built up as follows. In Section 3.2 we look at the single mode version of the quantum FGR rate as derived in the last chapter. In Section 3.3 we apply this expression to calculate the transfer rates of electrons and holes in three molecular semiconductors employed in OLEDs, based on first principles calculations of all intermolecular vibron frequencies and reorganization energies for simulated morphologies of these semiconductors. In Section 3.4 we calculate the resulting mobilities of electrons and holes as well as their energetic relaxation in these three materials. Section 3.5 contains a summary and conclusion. Values of the calculated intermolecular vibron frequencies and their corresponding reorganization energies, and various checks and comparisons can be found in the appendix.

3.2 Full quantum charge transfer rate

The product of Bessel functions derived in the previous chapter represents the FGR expression including all vibron modes. Taking one factor of the product, we obtain the single mode approximation of the FGR rate.

$$\begin{aligned} k &= \frac{2\pi}{\hbar} J^2 \exp\left[-\frac{\lambda}{\hbar\omega}\frac{1+z}{1-z}\right] \exp\left(\frac{\Delta n\hbar\omega}{2k_{\mathrm{B}}T}\right) \sum_{\Delta n} I_{\Delta n}\left[2\left(\frac{\lambda}{\hbar\omega}\right)\frac{\sqrt{z}}{1-z}\right] \times \\ &\quad \delta\big(\Delta E + \Delta n\hbar\omega\big). \end{aligned} \tag{3.2}$$

From this, we exploit the δ-function to replace $\Delta n\hbar\omega$ with $-\Delta E$ and obtain,

$$\begin{aligned} k &= \frac{2\pi}{\hbar} J^2 \exp\left(-\frac{\Delta E}{2k_{\mathrm{B}}T}\right) \exp\left[-\frac{\lambda}{\hbar\omega}\frac{1+z}{1-z}\right] \sum_{\Delta n} I_{\Delta n}\left[2\left(\frac{\lambda}{\hbar\omega}\right)\frac{\sqrt{z}}{1-z}\right] \times \\ &\quad \delta\big(\Delta E + \Delta n\hbar\omega\big). \end{aligned} \tag{3.3}$$

In Fig. 3.1 we show the ΔE dependence of the single mode FGR rate Eq. (3.3) at room temperature ($T = 300$ K) for different values of its frequency and coupling strength. A typical value $J = 1$ meV is chosen for the electronic coupling. For $\hbar\omega = k_{\mathrm{B}}T/2$ (left column), the Marcus rate Eq. (3.1) is approximately recovered, as expected, while for $\hbar\omega = 2k_{\mathrm{B}}T$ and $8k_{\mathrm{B}}T$ (middle and right column) Eq. (3.1) is inaccurate. For $\hbar\omega = 8k_{\mathrm{B}}T$ and $\lambda = \hbar\omega$ or $2\hbar\omega$ the full quantum rate is significantly larger than the Marcus rate around $\Delta E = 0$, in accordance with the rate enhancement by nuclear tunneling [2]. Interestingly, the ΔE dependence of the full quantum rates for $\hbar\omega = 8k_{\mathrm{B}}T$ is close to that of the MA rate, in particular for $\lambda = \hbar\omega$. The reason is that for that case the prefactors of the δ-function in Eq. (3.3) for $\Delta n = 0$ and $\Delta n = 1$ are approximately equal.

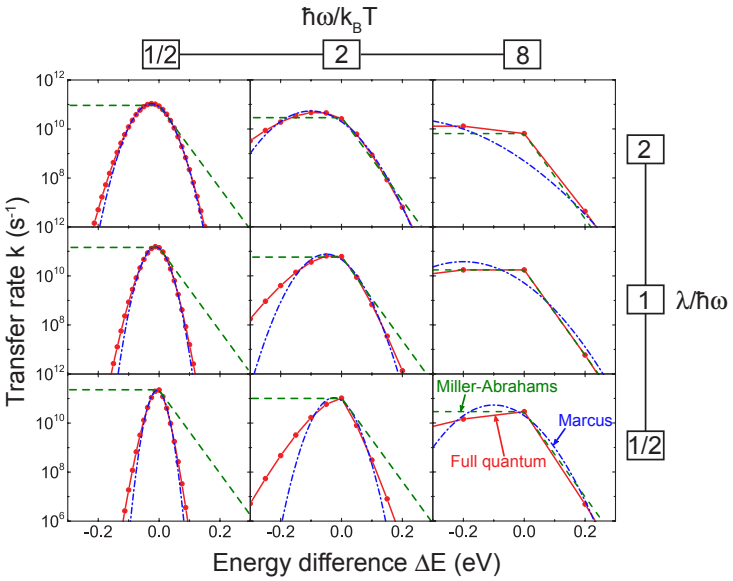

Figure 3.1: Transfer rates at $T = 300$ K vs. energy difference ΔE between two sites with electronic coupling $J = 1$ meV, and coupling to one vibron mode with varying frequency ω and reorganization energy λ. Red discs/full lines: full quantum rate (prefactor of δ-function in Eq. (3.3) divided by $\hbar\omega$). Blue dash-dotted curves: Marcus rate. Dashed green lines: MA rate, scaled to reproduce the full quantum rate at $\Delta E = 0$.

3.3 Electron and hole transfer rates: Application to α-NPD, TCTA, and spiro-DPVBi

We now turn to three specific molecular semiconductors employed in OLEDs, α-NPD [N,N'-di(1-naphthyl)-N,N'-diphenyl-(1,1'-biphenyl)-4,4'-diamine] and TCTA [tris(4-carbazoyl-9-ylphenyl)amine], both used as hole conductor and host for phosphorescent emitters, and spiro-DPVBi [2,2',7,7'-tetrakis(2,2-diphenylvinyl)spiro-9,9'-bifluorene], used as electron conductor and fluorescent emitter [18]. Recently, charge transport in these materials was studied using Marcus theory [16], on the basis of a simulated morphology and *ab initio* calculations of the molecular on-site energies, reorganization energies, and electronic couplings. In Fig. 3.2(a) we display for these materials the cumulative reorganization energy $\lambda(\omega) = \sum_{\omega_i<\omega} \lambda_i$ for electrons and holes of 20 molecules randomly chosen from an amorphous sample simulated as explained in the previous chapter, taking into account *all* intramolecular modes. Appendix A.2 explains how the frequencies ω_i and electron and hole reorganization energies λ_i of these modes were obtained for the three materials, and includes tables of their calculated values.

Clearly visible in Fig. 3.2(a) are the large contributions to λ of modes involving C-C bond vibrations in the range 0.1-0.2 eV. However, there are also important contributions from various dihedral rotations and other low-energy modes, particularly for electrons and holes in spiro-DPVBi and for holes in α-NPD and TCTA, resulting in quasi-continuous spectra up to about 0.2 eV. Additionally, small contributions involving C-H bond vibrations are visible just below 0.4 eV.

In the amorphous solid phase, apart from coupling to intramolecular modes, charges couple to intermolecular modes. Our present calculational framework does not allow to evaluate this coupling. However, intermolecular modes will have low frequencies and can therefore be treated classically. Their effect can thus be accommodated by introducing a "classical" reorganization energy $\lambda_{\rm cl}$ and replacing the δ-function in Eq. (3.3) by the right-hand-side of Eq. (3.1) with $\lambda = \lambda_{\rm cl}$ (excluding the factor $2\pi J^2/\hbar$), leading to a Gaussian broadening. We expect $\lambda_{\rm cl}$ to be considerably smaller than the intramolecular reorganization energies, but a small non-zero value is required in the charge dynamics calculations in the next section to allow for charge transfer at the various ΔE-values occurring in the amorphous phase. In Appendix A.3 we show for electrons in α-NPD and TCTA (the two most critical cases) that in a broad range $0.001 < \lambda_{\rm cl} < 0.05$ eV the room-temperature mobility in the amorphous phase is practically independent of $\lambda_{\rm cl}$. In all results presented henceforth we took the computationally convenient value $\lambda_{\rm cl} = 0.01$ eV.

In Fig. 3.2(b) we show for this value and $J = 1$ meV the ΔE dependence of the full quantum rates at room temperature for all 400 combinations of the molecules from Fig. 3.2(a), adding the vibron coupling spectra of two molecules to obtain the spectrum of their combination. The quasi-continuous spectra wash out features in

the rates, except for electrons in α-NPD and TCTA, for which the coupling to low-energy vibrons is relatively small. For these two cases features related to the 0.2 eV vibrons are clearly visible. The results are reminiscent of those for $\hbar\omega = 8k_{\mathrm{B}}T$ at room temperature and $\lambda = \hbar\omega \approx 0.2$ eV in Fig. 3.1. They can be understood as originating from a dominant mode of energy $\hbar\omega \approx 0.2$ eV, with low-frequency modes "filling up" to a varying degree the regions in between integer multiples of this energy.

We also show in Fig. 3.2(b) the Marcus rates for the average reorganization energy $\bar{\lambda}$ of all combinations of molecules (the values are, respectively, $\bar{\lambda} = 0.120$, 0.085, and 0.299 eV for electrons in the three materials, and $\bar{\lambda} = 0.212$, 0.184, and 0.212 eV for holes). In addition, we show MA rates with a prefactor tuned to reproduce the room-temperature zero-field mobilities (see next section). The Marcus as well as the MA rates roughly follow the quantum rates in the displayed energy range, but differences up to an order of magnitude do occur. A comparison between the quantum rates and the MLJ rates is given in Fig. 3.4 in Appendix A.1, showing that these rates are inapplicable to modeling charge dynamics in amorphous molecular semiconductors.

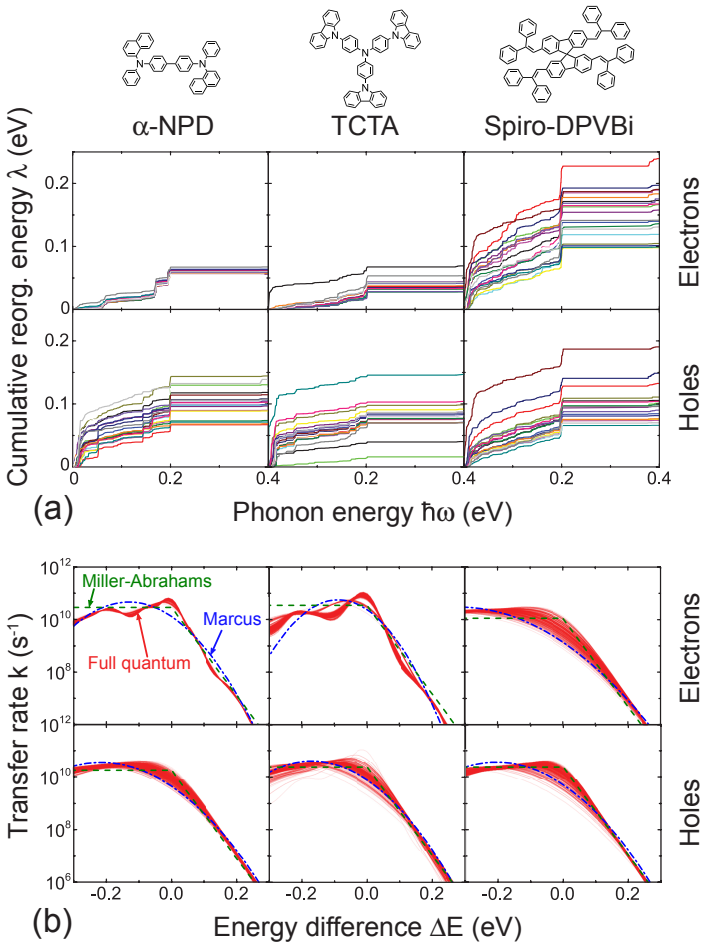

Figure 3.2: (a) Cumulative reorganization energies for electrons and holes on 20 molecules randomly chosen from α-NPD, TCTA, and spiro-DPVBi samples. (b) Energy dependence of transfer rates at $T = 300$ K for $J = 1$ meV. Red curves: full quantum rates for all 400 combinations of molecules from (a), using $\lambda_{\rm cl} = 0.01$ eV. Blue dash-dotted curves: Marcus rate using the average reorganization energy $\bar{\lambda}$ of the 20 molecules. Dashed green lines: MA rate with prefactor scaled to reproduce $\mu_{\rm full}$ in Fig. 3.3(a) at $T = 300$ K and $F = 0$.

3.4 Mobilities and energetic relaxation of electrons and holes: Application to α-NPD, TCTA, and spiro-DPVBi

In evaluating the charge-carrier mobilities μ we follow the procedures introduced in Chapter 2. With a stochastic expansion method [5], simulated morphologies of the materials in relatively small simulation boxes are stochastically expanded to a collection of sites representing molecular centers of mass in boxes of size $100\times100\times100$ nm^3, large enough to allow reliable evaluation of μ by solving a master equation. A Gaussian DOS is taken for the site energies of electrons and holes, with standard deviations σ equal to those of *ab initio* calculations of the energies of the lowest unoccupied and highest occupied molecular orbitals (LUMO and HOMO) [9], respectively, of 1000 molecules in the simulated morphology (the values are, respectively, $\sigma = 0.087$, 0.100, and 0.156 eV for electrons in the three materials, and $\sigma = 0.087$, 0.136, and 0.122 eV for holes [16]). We neglect spatial correlations in the site energies; they only weakly increase μ in the considered materials [16]. The electronic couplings J between sites at a certain intersite distance are obtained by the stochastic method described in Chapter 2. We randomly assign a label in the range 1-20 to each site and attribute one of the 400 transfer rates of Fig. 3.2(b) to each pair of electronically coupled sites (correcting the prefactor for the actual value of J) according to its label combination. We account for the presence of an electric field F by adding an appropriate term to ΔE.

Figure 3.3(a) shows the resulting F dependence of the full quantum mobilities $\mu_{\rm full}$ at $T = 300$ and 200 K, which we compare to $\mu_{\rm Marcus}$ and $\mu_{\rm MA}$ obtained with the Marcus and MA rates. Since for spatially uncorrelated disorder the F dependence of μ is approximately independent of the carrier concentration c at not too high F and c [23], we take a convenient value $c = 10^{-4}$ carriers per site, which is also realistic for OLEDs under operational conditions. The F-dependent μ at a different (not too high) c can be obtained from the shown curves using the universal c dependence of μ given in Ref. 7. The mobilities $\mu_{\rm MA}$ were obtained by tuning the prefactor in the MA rate such that the mobilities $\mu_{\rm full}$ at $T = 300$ K and $F = 0$ are reproduced. The values of the MA prefactor correspond to, respectively, $k_0/J^2 = 2.92\times10^{16}$, 3.46×10^{16}, and 1.12×10^{16} s^{-1}eV^{-2} for electrons in the three materials, and $k_0/J^2 = 1.79\times10^{16}$, 2.41×10^{16}, and 2.15×10^{16} s^{-1}eV^{-2} for holes. It is gratifying to see that all these prefactors are of comparable magnitude.

Extremely large differences between $\mu_{\rm full}$, $\mu_{\rm Marcus}$, and $\mu_{\rm MA}$ do not occur in Fig. 3.3(a), which should be ascribed to the washing out of most of the differences in the rates in Fig. 3.2(b) by the energetic disorder. Still, significant differences between $\mu_{\rm full}$ and $\mu_{\rm Marcus}$ of up to a factor of 3 do in some cases occur. Quite strikingly, in those cases $\mu_{\rm MA}$ yields a better description. By evaluating $\mu_{\rm Marcus}$ using the separately calculated reorganization energies (see Tables 3.1-3.3 in appendix A.2) instead of their average - leading to virtually the same results - we checked that the differences

between μ_{full} and μ_{Marcus} are not caused by taking the average reorganization energy for the latter case.

Figure 3.3(b) shows the dependence of the $F = 0$ mobilities on $\hat{\sigma}^2 \equiv (\sigma/k_{\text{B}}T)^2$ at a very low carrier concentration $c = 10^{-6}$, where the c dependence of μ has become almost negligible. For comparison, we draw dashed lines corresponding to $\mu \propto \exp\bigl(-C\hat{\sigma}^2\bigr)$ with $C = 0.4$, as approximately found in Ref. [16]. We conclude that this dependence is still rather well obeyed. Again, we observe that μ_{MA} quite accurately describes μ_{full}. At low T we observe an enhancement of μ_{full} with respect to μ_{Marcus}, amounting to a factor of about 3 for holes in α-NPD at the lowest considered T, which can be attributed to nuclear tunneling. However, at room temperature (dotted line) this effect is in all cases unimportant.

We finally study energetic relaxation of carriers, which is claimed to play a crucial role in the functioning of bulk heterojunction OPV cells [28, 17]. This relaxation has predominantly been studied using the MA rate [4, 28, 17] and it is important to investigate the use of the full quantum rate. We evaluate energetic relaxation by solving a time-dependent master equation [19] in a $50 \times 50 \times 50$ nm^3 box with an equal occupational probability of all sites as initial condition. Figure 3.3(c) shows for the three materials the time evolution of the average energy $\langle E \rangle$ of electrons and holes relaxing in the Gaussian DOS. The temperature is $T = 300$ K, except for electrons in spiro-DPVBi, where for computational stability reasons related to the large value of σ we took $T = 400$ K. The results of using full quantum, Marcus, or MA rates are almost indistinguishable.

3.5 Summary and conclusion

Summarizing, we have studied the charge dynamics in three molecular semiconductors used in OLEDs with a hopping rate that includes the coupling to all intramolecular vibron modes in a fully quantum mechanical way, improving on the widely used semiclassical Marcus rate. In some cases we find a significant modulation of the rate associated with C-C bond vibrations. Benchmark results for the mobility and energetic relaxation of electrons and holes are obtained that are free from uncontrolled approximations. We find that nuclear tunneling can affect the mobility at low temperature. Surprisingly good results for the mobilities as well as the energetic relaxation of charge carriers are obtained with the simple and material-independent Miller-Abrahams rate, which can be used as a computationally cost-effective alternative. We conclude that extracting the disorder strength from temperature-dependent charge transport studies, as initially proposed by Bässler [4], is well possible, but extracting the reorganization energy is not.

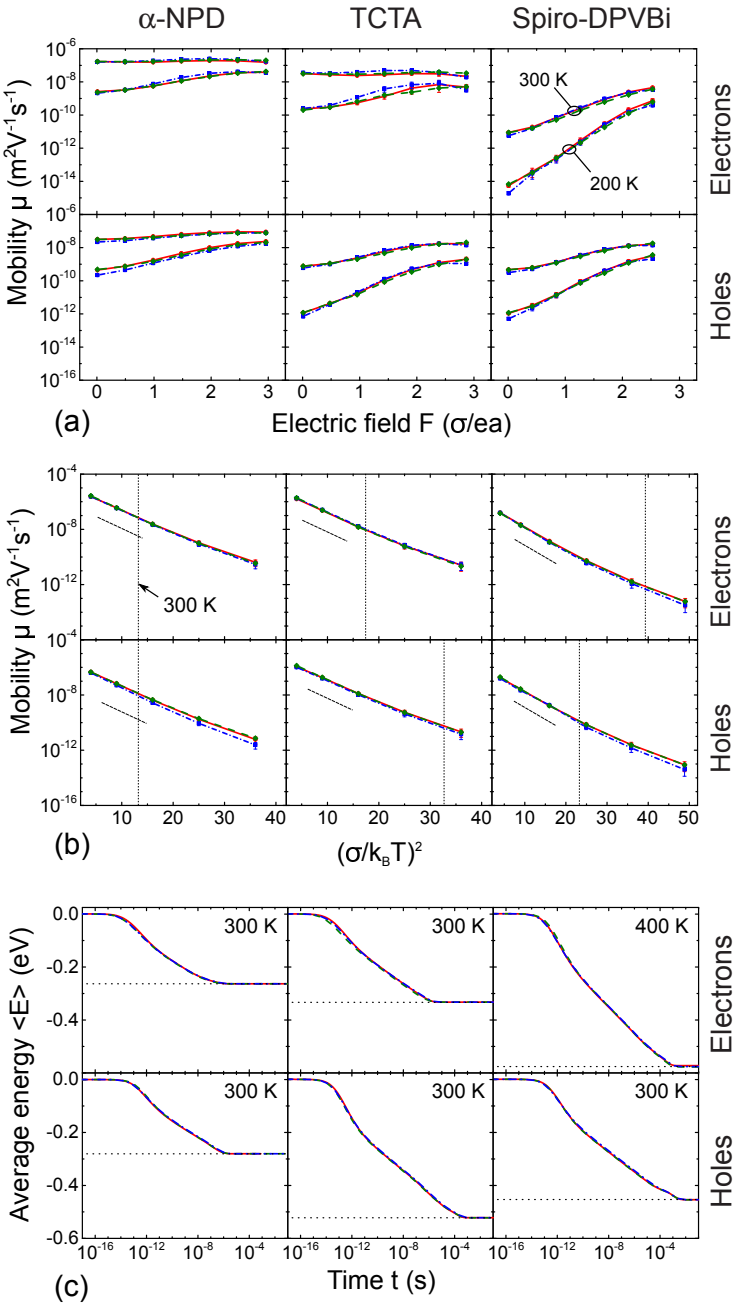
α-NPD
TCTA
Spiro-DPVBi
Mobility μ (m²V⁻¹s⁻¹)
300 K
200 K
Electrons
Holes
(a)
Electric field F (σ/ea)
(b)
(σ/k_BT)²
Average energy <E> (eV)
400 K
Time t (s)
(c)

Figure 3.3: (a) Field dependent mobilities at $T = 300$ and 200 K, and carrier concentration $c = 10^{-4}$, where e is the charge unit and a the average intersite distance (1.01, 1.05, and 1.19 nm, respectively, in the three materials [16]). The results are averages over 10 disorder realizations. Red discs/solid lines: full quantum rates ($\mu_{\rm full}$). Blue squares/dash-dotted lines: Marcus rates ($\mu_{\rm Marcus}$). Green diamonds/dashed lines: MA rates ($\mu_{\rm MA}$), scaled to reproduce $\mu_{\rm full}$ at $T = 300$ K and $F = 0$. (b) Dependence of mobilities on $\hat{\sigma}^2 \equiv (\sigma/k_{\rm B}T)^2$ for $c = 10^{-6}$ and $F = 0$. Dotted lines indicate $T = 300$ K and dashed lines slopes corresponding to $\mu \propto \exp\bigl(-0.4\hat{\sigma}^2\bigr)$. (c) Time dependent average energy, with respect to the center of the DOS, of carriers initially released at arbitrary sites ($T = 400$ K for electrons in spiro-DPVBi and 300 K for all other cases). Dotted lines indicate full relaxation.

Appendix

A.1 Relation and comparison to the Marcus-Levich-Jortner rate

The Marcus-Levich-Jortner (MLJ) formulation [14, 11], which goes beyond the semi-classical approximation, assumes an initial state without vibrons in the modes that are treated quantum mechanically. Thermal excitations in the classically treated modes are still accounted for. We start with Eq. (3.4) which is taken from Chapter 2 for the case of transfer to like molecules

$$\begin{aligned}\rho_{\rm FC}(\Delta E) &= \frac{1}{2\pi\hbar}\int_{-\infty}^{\infty} dt \exp\left[i\frac{(\Delta E+\lambda_{\rm cl})t}{\hbar} - \frac{\lambda_{\rm cl}k_{\rm B}Tt^2}{\hbar^2}\right.\\ &\left. + \sum_i \frac{\lambda_i}{\hbar\omega_i}\left(\coth\left(\frac{\hbar\omega_i}{2k_BT}\right)\Big[\cos(\omega_i t)-1\Big] + i\sin(\omega_i t)\right)\right]. \quad (3.4)\end{aligned}$$

here, $\lambda_i = 2\lambda_i'$ where λ_i' is the vibronic coupling of the single molecule. To obtain the MLJ expression we take the limit $T \to 0$, but keep T finite in the second term in the exponent of the integrand in Eq. (3.4). As a result, we obtain:

$$\begin{aligned}\rho_{\rm MLJ} &= \frac{1}{2\pi\hbar}\exp\left[-\sum_i \frac{\lambda_i}{\hbar\omega_i}\right]\\ &\times \int_{-\infty}^{\infty} dt \exp\left[i\frac{(\Delta E+\lambda_{\rm cl})\,t}{\hbar} - \frac{\lambda_{\rm cl}k_{\rm B}Tt^2}{\hbar^2} + \sum_i \frac{\lambda_i}{\hbar\omega_i}\exp(i\omega_i t)\right], \quad (3.5)\end{aligned}$$

which is an expression that allows more efficient numerical computation than the familiar expression for the multi vibron mode MLJ rate:

$$\rho_{\rm MLJ} = \frac{1}{\sqrt{4\pi\lambda_{\rm cl}k_{\rm B}T}}\prod_i\left(\exp\left[-\frac{\lambda_i}{\hbar\omega_i}\right]\sum_{\Delta n_i=0}^{\infty}\frac{(\lambda_i/\hbar\omega_i)^{\Delta n_i}}{\Delta n_i!}\right) \exp\left[-\frac{(\Delta E+\lambda_{\rm cl}+\sum_i\Delta n_i\hbar\omega_i)^2}{4\lambda_{\rm cl}k_{\rm B}T}\right]. \quad (3.6)$$

By expanding $\exp\left[\sum_i \frac{\lambda_i}{\hbar\omega_i}\exp(i\omega_i t)\right]$ in a Taylor series and performing the time integral in Eq. (3.5) one can show that Eqs. (3.5) and (3.6) are equivalent.

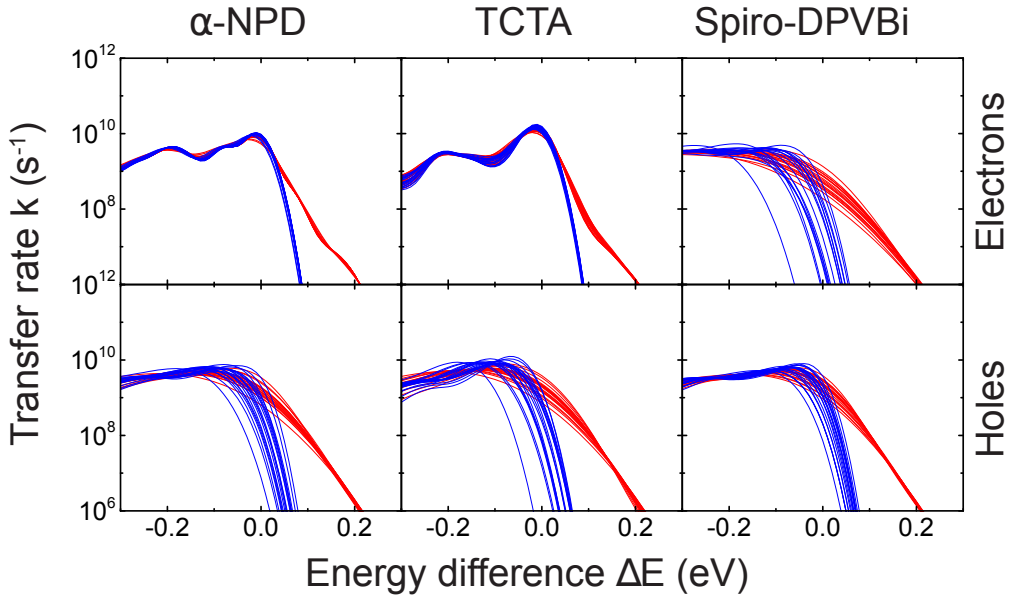

Figure 3.4: Full quantum rates (red curves) and MLJ rates (blue curves) for electron and hole transfer at room temperature as a function of ΔE for 20 randomly chosen pairs in the three materials studied in this chapter, for $J = 1$ meV and $\lambda_{\rm cl} = 0.01$ eV.

In Fig. 3.4 we compare the ΔE dependence at room temperature of the MLJ rates Eq. (3.5) (blue curves) with that of the full quantum rates (red curves) for 20 randomly chosen molecular pairs of the three materials studied in this chapter, for electrons and holes. As in the main text, we have taken $J = 1$ meV and $\lambda_{\rm cl} = 0.01$ eV. It is clear that for $\Delta E < 0$ the MLJ rates are in general reasonably accurate (yet in some specific

cases they are still significantly off) but that they are inapplicable for $\Delta E > 0$, where they are much too small. In the percolative transport in the disordered amorphous semiconductors studied in this work, the charge-carrier mobility is determined by "difficult but necessary" hops, which will almost always have $\Delta E > 0$. Hence, the MLJ rates are inapplicable to modeling charge dynamics in amorphous molecular semiconductors.

A.2 Calculation of the vibron energies and coupling in embedded environments

Morphologies of α-NPD, TCTA, and spiro-DPVBi were obtained using the METROPOLIS Monte Carlo based simulated annealing protocol DEPOSIT [22], which was applied to simulate the deposition of about 1000 molecules in the vertical direction in simulation boxes of a lateral size of 7×7 nm^2 with periodic boundary conditions in the lateral directions. For each material we randomly selected 20 molecules and calculated their intramolecular phonon mode frequencies ω_i, the reorganization energies λ_i associated with all modes i, and their total reorganization energies λ for charging with an electron or a hole. The calculations were performed using density functional theory (DFT) with a def2-SV(P) [26] basis set and a B3LYP [6] functional as implemented in TURBOMOLE [1]. Every molecule is surrounded by an environment of 100 effective all-electron potentials to take into account the confinement of the molecule by the surrounding molecules [8].

The total reorganization energies λ for electrons and holes were calculated using Nelsen's four-point procedure. They are split into a charging (λ^0) and decharging (λ^*) contribution. The results are given in Tables 3.1-3.3 for the three materials. The frequencies ω_i and reduced masses μ_i of the vibron (normal) modes were obtained from the mass-weighted Hessian matrix of force constants. The displacements of all atoms in all three cartesian directions from their equilibrium positions for the neutral molecule to the equilibrium positions for the charged molecule were decomposed in displacements Δq_i of the vibron modes i. The reorganization energies λ_i were then obtained as $\lambda_i = \frac{1}{2}\mu_i\omega_i^2\Delta q_i^2$.

When the charge-vibron coupling is linear in the displacements Δq_i of the vibron modes and when these displacements are within the harmonic regime, we have $\lambda^0 = \lambda^* = \sum_i \lambda_i$. We see from Tables 3.1-3.3 that this is almost always to a reasonable approximation the case. In cases where $\sum_i \lambda_i$ calculated with this method was 30% larger than λ^0 we used a different method to calculate the λ_i's. In those cases, indicated with a star (*) in Tables 3.1-3.3, we used a linearization method in which we calculated the derivatives $\partial E/\partial q_i$ of the total energy of the charged molecule with respect to the vibron mode coordinates q_i in the equilibrium structure of the neutral molecule. From these derivatives we calculated Δq_i as $\Delta q_i = (\partial E/\partial q_i)/\mu_i\omega_i^2$ and from these the reorganization energies $\lambda_i = \frac{1}{2}\mu_i\omega_i^2\Delta q_i^2$. In this way we obtain the leading linear term of the charge-vibron coupling. It is seen in Tables 3.1-3.3 that this method always yields reasonable values of $\sum_i \lambda_i$. We note, however, that

the method is necessarily approximate, because in these cases the displacements are beyond the linear regime of the charge-vibron coupling and/or beyond the harmonic regime. Because these cases are rare, they have no significant effect on the results presented in this chapter. We also note that for the first spiro-DPVBi molecule in Table 3.3, λ^0 is negative for charging by an electron. The reason is that the molecule is in a local minimum and can gain energy by crossing a barrier in the direction of the equilibrium structure of the charged molecule. This is accompanied by a very large positive value of λ^*. However, also for this case $\sum_i \lambda_i$ as calculated with the linearization method has a reasonable value.

Table 3.1: Reorganization energies λ^0 for charging, λ^* for decharging, and the sum $\sum_i \lambda_i$ of the reorganization energies associated with all intramolecular phonon modes for 20 α-NPD molecules randomly chosen from a simulated sample of about 1000 molecules. The values indicated with a star (*) were obtained with the linearization method explained in the text.

α-NPD electron			α-NPD hole		
λ^0 (eV)	λ^* (eV)	$\sum_i \lambda_i$ (eV)	λ^0 (eV)	λ^* (eV)	$\sum_i \lambda_i$ (eV)
0.066	0.072	0.067	0.116	0.104	0.108
0.061	0.061	0.061	0.110	0.102	0.103
0.058	0.057	0.059	0.096	0.104	0.106
0.057	0.055	0.057	0.154	0.157	0.170
0.057	0.056	0.057	0.053	0.062	0.062
0.061	0.060	0.061	0.137	0.129	0.130
0.061	0.060	0.062	0.159	0.135	0.188
0.060	0.058	0.060	0.127	0.110	0.139
0.060	0.060	0.061	0.087	0.081	0.089
0.063	0.061	0.063	0.067	0.060	0.067
0.057	0.064	0.060	0.098	0.091	0.098
0.057	0.055	0.057	0.092	0.086	0.074*
0.063	0.065	0.064	0.103	0.096	0.099
0.062	0.064	0.063	0.094	0.086	0.090
0.062	0.062	0.063	0.106	0.108	0.105
0.056	0.055	0.056	0.116	0.117	0.097*
0.059	0.064	0.060	0.071	0.066	0.071
0.061	0.062	0.063	0.114	0.113	0.108
0.055	0.058	0.056	0.138	0.147	0.125*
0.061	0.060	0.062	0.122	0.116	0.115

Table 3.2: Same as Table 3.1, but for TCTA.

TCTA electron			TCTA hole		
λ^0 (eV)	λ^* (eV)	$\sum_i \lambda_i$ (eV)	λ^0 (eV)	λ^* (eV)	$\sum_i \lambda_i$ (eV)
0.032	0.034	0.033	0.017	0.017	0.016
0.053	0.048	0.053	0.072	0.062	0.070
0.033	0.035	0.033	0.120	0.142	0.104*
0.040	0.041	0.041	0.108	0.115	0.083*
0.043	0.042	0.043	0.083	0.086	0.071*
0.037	0.043	0.038	0.079	0.070	0.070*
0.041	0.041	0.043	0.088	0.091	0.088
0.039	0.038	0.039	0.085	0.085	0.081
0.043	0.041	0.044	0.149	0.111	0.082*
0.031	0.033	0.032	0.085	0.117	0.099*
0.067	0.220	0.069*	0.232	0.108	0.040*
0.036	0.036	0.037	0.077	0.077	0.076
0.028	0.031	0.029	0.085	0.090	0.087
0.032	0.038	0.032	0.085	0.091	0.092
0.043	0.042	0.043	0.082	0.077	0.076
0.034	0.035	0.035	0.087	0.087	0.084
0.032	0.033	0.033	0.113	0.141	0.147*
0.027	0.030	0.028	0.083	0.077	0.077
0.033	0.035	0.034	0.078	0.077	0.076
0.037	0.038	0.039	0.080	0.078	0.077

Table 3.3: Same as Table 3.1, but for spiro-DPVBi.

spiro-DPVBI electron			spiro-DPVBI hole		
λ^0 (eV)	λ^* (eV)	$\sum_i \lambda_i$ (eV)	λ^0 (eV)	λ^* (eV)	$\sum_i \lambda_i$ (eV)
-0.052	0.535	0.166*	0.087	0.103	0.101
0.173	0.149	0.197	0.133	0.198	0.149
0.210	0.216	0.239	0.133	0.131	0.133
0.151	0.150	0.136*	0.089	0.091	0.099
0.091	0.104	0.099	0.067	0.067	0.066
0.138	0.139	0.142	0.095	0.088	0.096
0.134	0.116	0.147	0.067	0.069	0.068
0.180	0.164	0.131*	0.069	0.077	0.070
0.232	0.258	0.191*	0.107	0.197	0.191*
0.147	0.169	0.173	0.103	0.099	0.106
0.129	0.124	0.140	0.081	0.215	0.085
0.171	0.183	0.189	0.071	0.072	0.074
0.115	0.106	0.119	0.064	0.070	0.067
0.159	0.143	0.167	0.097	0.159	0.104
0.088	0.105	0.101	0.077	0.080	0.081
0.155	0.133	0.175	0.081	0.098	0.090
0.164	0.148	0.183	0.073	0.078	0.076
0.102	0.105	0.105	0.106	0.097	0.111
0.227	0.205	0.158*	0.097	0.094	0.096
0.094	0.099	0.098	0.074	0.173	0.076

A.3 Influence of λ_{cl} on charge transfer rates and mobilities

Equation (3.4) with $\lambda_{\mathrm{cl}} = 0.01$ eV is used in this chapter to calculate the full quantum transfer rates, mobilities, and energy relaxation of electrons and holes in α-NPD, TCTA, and spiro-DPVBi. We investigate the effect of using different values of λ_{cl} in Fig. 3.5. Figure 3.5(a) and (b) show the room-temperature rates for electron transfer in α-NPD and TCTA, respectively, for $\lambda_{\mathrm{cl}} = 0.001$ eV (green lines), 0.01 eV (red lines, same results as in Fig. 3.2(b)), and 0.05 eV (blue lines). Figure 3.5(c) and (d) show the corresponding room-temperature mobilities as a function of electric field. While detailed features in the rates clearly depend on the value of λ_{cl}, the variations in the mobilities do not exceed 40% (note that λ_{cl} varies by a factor of fifty!). This shows that the mobilities are quite insensitive to the choice of λ_{cl}. The two considered

cases of electrons in α-NPD and TCTA are the most critical. For the other cases the mobilities are even less sensitive to the choice of λ_{cl}.

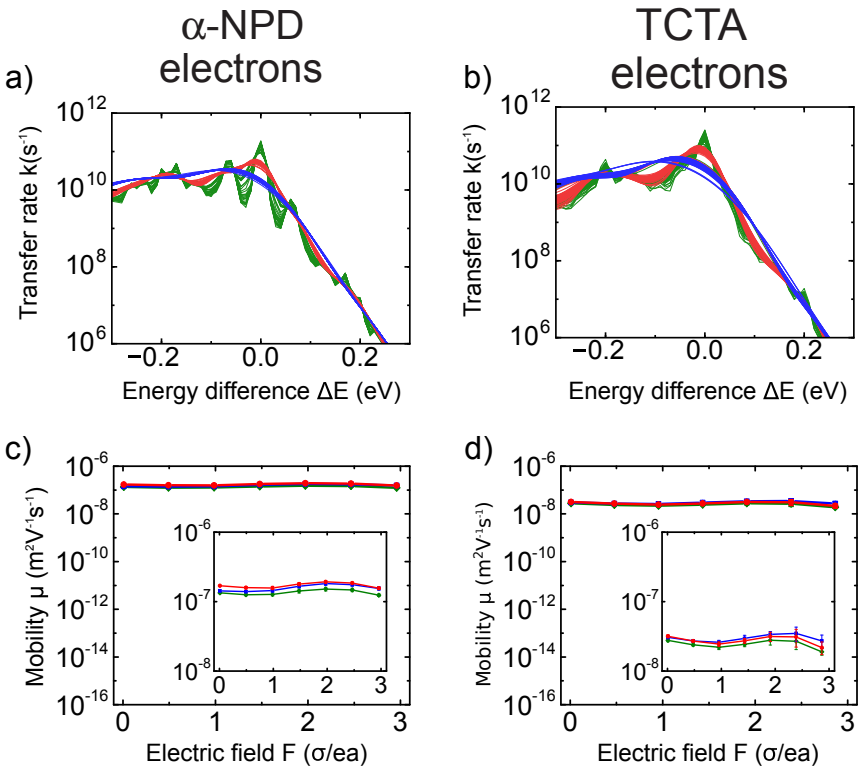

Figure 3.5: (a) and (b) Room-temperature full quantum transfer rates as a function of energy difference ΔE calculated for electrons in α-NPD and TCTA, respectively, for $J = 1$ meV. Green lines: $\lambda_{\mathrm{cl}} = 0.001$ eV. Red lines: $\lambda_{\mathrm{cl}} = 0.01$ eV (same as in Fig. 3.2(b)). Blue lines: $\lambda_{\mathrm{cl}} = 0.05$ eV. (c) and (d) Electron mobilities μ in α-NPD and TCTA, respectively, as a function of electric field F for the different values of λ_{cl} in (a) and (b). The scale of the vertical axis in the main panels is the same as in Fig. 3.3(a). The insets have a reduced vertical scale to make the differences visible.

Bibliography

[1] R. Ahlrichs, M. Bär, M. Häser, H. Horn, and C. Kölmel. Electronic structure calculations on workstation computers: The program system turbomole. *Chem. Phys. Lett.*, 162(3):165 – 169, 1989. ISSN 0009-2614. doi: http://dx.doi.org/10.1016/0009-2614(89)85118-8. URL `http://www.sciencedirect.com/science/article/pii/0009261489851188`.

[2] K. Asadi, A. J. Kronemeijer, T. Cramer, L. Jan Anton Koster, P. W. M. Blom, and D. M. de Leeuw. Polaron hopping mediated by nuclear tunnelling in semiconducting polymers at high carrier density. *Nat. Commun.*, 4:1710, 2013.

[3] S. Baranovskii, O. Rubel, and P. Thomas. Theoretical description of hopping transport in disordered materials. *Thin Solid Films*, 487(1-2):2 – 7, 2005.

[4] H. Bässler. Charge transport in disordered organic photoconductors. *Phys. Status Solidi (b)*, 175:15, 1993.

[5] B. Baumeier, O. Stenzel, C. Poelking, D. Andrienko, and V. Schmidt. Stochastic modeling of molecular charge transport networks. *Phys. Rev. B*, 86:184202, Nov 2012. doi: 10.1103/PhysRevB.86.184202. URL `http://link.aps.org/doi/10.1103/PhysRevB.86.184202`.

[6] A. D. Becke. A new mixing of hartree-fock and local density-functional theories. *J. Chem. Phys.*, 98(2):1372–1377, 1993. doi: http://dx.doi.org/10.1063/1.464304. URL `http://scitation.aip.org/content/aip/journal/jcp/98/2/10.1063/1.464304`.

[7] J. Cottaar, L. J. A. Koster, R. Coehoorn, and P. A. Bobbert. Scaling theory for percolative charge transport in disordered molecular semiconductors. *Phys. Rev. Lett.*, 107:136601, Sep 2011. URL `http://link.aps.org/doi/10.1103/PhysRevLett.107.136601`.

[8] M. Dolg, U. Wedig, H. Stoll, and H. Preuss. Energy-adjusted ab initio pseudopotentials for the first row transition elements. *The Journal of Chemical Physics*, 86(2):866–872, 1987.

[9] P. Friederich, F. Symalla, V. Meded, T. Neumann, and W. Wenzel. Ab Initio Treatment of Disorder Effects in Amorphous Organic Materials: Toward Parameter Free Materials Simulation. *J. Chem. Theory Comput.*, 10(9):3720–3725, 2014.

[10] P. Friederich, V. Meded, A. Poschlad, T. Neumann, V. Rodin, V. Stehr, F. Symalla, D. Danilov, G. Lüdemann, R. F. Fink, I. Kondov, F. von Wrochem, and W. Wenzel. Molecular origin of the charge carrier mobility in small molecule

organic semiconductors. *Adv. Funct. Mater.*, 26(31):5757–5763, 2016. ISSN 1616-3028. doi: 10.1002/adfm.201601807. URL `http://dx.doi.org/10.1002/adfm.201601807`.

[11] J. Jortner. Temperature dependent activation energy for electron transfer between biological molecules. *J. Chem. Phys.*, 64(12):4860–4867, 1976. doi: 10.1063/1.432142.

[12] P. Kordt, J. J. M. van der Holst, M. Al Helwi, W. Kowalsky, F. May, A. Badinski, C. Lennartz, and D. Andrienko. Modeling of organic light emitting diodes: From molecular to device properties. *Adv. Funct. Mater.*, 25(13):1955–1971, 2015. ISSN 1616-3028. doi: 10.1002/adfm.201403004. URL `http://dx.doi.org/10.1002/adfm.201403004`.

[13] J. J. Kwiatkowski, J. Nelson, H. Li, J. L. Bredas, W. Wenzel, and C. Lennartz. Simulating charge transport in tris(8-hydroxyquinoline) aluminium (alq3). *Phys. Chem. Chem. Phys.*, 10:1852–1858, 2008.

[14] R. A. Marcus. On the theory of oxidation-reduction reactions involving electron transfer. i. *J. Chem. Phys.*, 24(5):966–978, 1956. doi: 10.1063/1.1742723.

[15] R. A. Marcus. Electron transfer reactions in chemistry. theory and experiment. *Rev. Mod. Phys.*, 65(3):599–610, 1993.

[16] A. Massé, P. Friederich, F. Symalla, F. Liu, V. Meded, R. Coehoorn, W. Wenzel, and P. A. Bobbert. Effects of energy correlations and superexchange on charge transport and exciton formation in amorphous molecular semiconductors: An ab initio study. *Phys. Rev. B*, 95:115204, Mar 2017. doi: 10.1103/PhysRevB.95.115204. URL `https://link.aps.org/doi/10.1103/PhysRevB.95.115204`.

[17] A. Melianas, F. Etzold, T. J. Savenije, F. Laquai, O. Inganäs, and M. Kemerink. Photo-generated carriers lose energy during extraction from polymer-fullerene solar cells. *Nat. Commun.*, 6:8778, 2015.

[18] M. Mesta, M. Carvelli, R. J. de Vries, H. van Eersel, J. J. M. van der Holst, M. Schober, M. Furno, B. Lüssem, K. Leo, P. Loebl, R. Coehoorn, and P. A. Bobbert. Molecular-scale simulation of electroluminescence in a multilayer white organic light-emitting diode. *Nature Mater.*, 12:652, 2013.

[19] M. Mesta, C. Schaefer, J. de Groot, J. Cottaar, R. Coehoorn, and P. A. Bobbert. Charge-carrier relaxation in disordered organic semiconductors studied by dark injection: Experiment and modeling. *Phys. Rev. B*, 88:174204, Nov 2013. doi: 10.1103/PhysRevB.88.174204. URL `https://link.aps.org/doi/10.1103/PhysRevB.88.174204`.

[20] A. Miller and E. Abrahams. Impurity conduction at low concentrations. *Phys. Rev.*, 120(3):745–755, 1960.

[21] G. Nan, L. Wang, X. Yang, Z. Shuai, and Y. Zhao. Charge transfer rates in organic semiconductors beyond first-order perturbation: From weak to strong coupling regimes. *J. Chem. Phys.*, 130(2):024704, 2009.

[22] T. Neumann, D. Danilov, C. Lennartz, and W. Wenzel. Modeling disordered morphologies in organic semiconductors. *J. Comput. Chem.*, 34(31):2716–2725, 2013. ISSN 1096-987X. doi: 10.1002/jcc.23445. URL `http://dx.doi.org/10.1002/jcc.23445`.

[23] W. F. Pasveer, J. Cottaar, C. Tanase, R. Coehoorn, P. A. Bobbert, P. W. M. Blom, D. M. de Leeuw, and M. A. J. Michels. Unified description of charge-carrier mobilities in disordered semiconducting polymers. *Phys. Rev. Lett.*, 94 (20):206601, 2005.

[24] Y. Roichman and N. Tessler. Charge transport in conjugated polymers: The influence of charge concentration. *Synth. Met.*, 135:443, 2003.

[25] V. Rühle, A. Lukyanov, F. May, M. Schrader, T. Vehoff, J. Kirkpatrick, B. Baumeier, and D. Andrienko. Microscopic simulations of charge transport in disordered organic semiconductors. *J. Chem. Theory Comput.*, 7(10):3335–3345, 2011. doi: 10.1021/ct200388s.

[26] A. Schäfer, H. Horn, and R. Ahlrichs. Fully optimized contracted gaussian basis sets for atoms li to kr. *J. Chem. Phys.*, 97(4):2571–2577, 1992. doi: http://dx.doi.org/10.1063/1.463096. URL `http://scitation.aip.org/content/aip/journal/jcp/97/4/10.1063/1.463096`.

[27] C. Tanase, E. J. Meijer, P. W. M. Blom, and D. M. de Leeuw. Unification of the hole transport in polymeric field-effect transistors and light-emitting diodes. *Phys. Rev. Lett.*, 91(21):216601, 2003.

[28] H. van Eersel, R. A. J. Janssen, and M. Kemerink. Mechanism for efficient photoinduced charge separation at disordered organic heterointerfaces. *Adv. Funct. Mater.*, 22(13):2700–2708, 2012. ISSN 1616-3028. doi: 10.1002/adfm.201200249. URL `http://dx.doi.org/10.1002/adfm.201200249`.

[29] K. Vandewal, J. Benduhn, K. S. Schellhammer, T. Vangerven, J. E. Rückert, F. Piersimoni, R. Scholz, O. Zeika, Y. Fan, S. Barlow, D. Neher, S. R. Marder, J. Manca, D. Spoltore, G. Cuniberti, and F. Ortmann. Absorption tails of donor:c60 blends provide insight into thermally activated charge-transfer processes and polaron relaxation. *J. Am. Chem. Soc.*, 139(4):1699–1704, 2017.

Chapter 4

Triplet exciton diffusion in metal-organic phosphorescent host-guest systems

In Chapter 3 we have looked at the effects of the FGR rate on the charge carrier mobility and dynamics in commonly used OLED host molecules. The full quantum FGR rate as a function of the site energy differences (ΔE) is very different from the Marcus and Miller-Abrahams rate for these molecules. In the final charge mobility of the whole system of molecules we do not see significant differences between the application of the different rate theories.

In this chapter we apply the same FGR rate to study triplet diffusion between common phosphorescent emitter molecules. We see that the vibronic coupling for the triplet transfer in these systems is much stronger than for the charge transfer studied in Chapter 3. As a consequence, the Marcus theory rate drastically underestimates the FGR transfer rate. Therefore, the diffusion lengths predicted by the Marcus theory in these systems are much too short. Additionally, we study the short range Dexter and long range Förster contributions to the transfer integrals for the triplet transfer. We find that at realistic guest concentration for OLED application of around 10 mol% the Förster contributions dominates the transfer integral and diffusion lengths are on the order of 2 nm. From 30 mol% guest concentration the Dexter contributions starts to play a role, and the diffusion length increases to around 30 nm for a neat film system of guest molecules.

This work has been published: X. de Vries, P. Friederich, R. Coehoorn and P. A. Bobbert, Phys. Rev. B 99, 205201 (2019).

4.1 Introduction

In phosphorescent organic light-emitting diodes (OLEDs), the emission takes place from a host-guest blend in which, often iridium-cored, metal-organic emitter molecules (guests) are incorporated at a small concentration in a host material. In dilute host-guest systems and at low luminance levels, the internal quantum efficiency (IQE) can be close to 100% [1, 29, 31]. With increasing guest concentration, the photoluminescence efficiency of host-guest systems is often found to decrease [30], leading to a decrease of the maximum possible IQE of OLEDs. This effect, known as concentration quenching, is attributed to increased triplet exciton diffusion at high guest concentrations, when transfer between the guests is favored due to shorter distances [24, 52]. Furthermore, at high luminance levels, triplet exciton diffusion enhances the IQE loss ("roll-off") that occurs due to triplet-triplet annihilation (TTA) and triplet-polaron quenching (TPQ) [5, 62, 60, 61, 70, 51, 44, 17, 12, 68, 27, 69, 33].

Triplet exciton diffusion has been extensively studied for purely organic neat-film materials that are commonly used as a host, as an electron or hole transport layer, or a fluorescent emissive layer [41, 35, 71, 14, 39]. Due to the long triplet lifetime in such materials and the small intermolecular distances, the diffusion lengths can be of the order of 100 nm. The transfer is commonly viewed as a result of a Dexter-type process [16], with an exponential ($\exp[-2\alpha R]$) distance (R) dependence. Here, α is an effective inverse triplet exciton wave function decay length. In contrast, the diffusion of triplets between iridium-cored phosphorescent emitter molecules, embedded at small concentrations in a host-guest blend, is less well understood. Kawamura *et al.* have suggested that the triplet diffusion leading to concentration quenching is best described as a result of a Förster-type dipole-dipole interaction, with an R^{-6} distance dependence. For molecules containing a heavy-metal atom such as iridium, which due to a strong spin-orbit interaction gives rise to a significant admixture of singlet character in the triplet state, such a mechanism is quantum-mechanically allowed. On the other hand, Ribierre *et al.* conclude that concentration quenching follows an exponential Dexter-type distance dependence [52]. Recently, Ligthart *et al.* have reported that the enhancement of the efficiency loss due to TTA in a phosphorescent host-guest system with varying guest concentration can be understood from both mechanisms [33]. From the latter study, carried out for guest concentrations x_{g} up to 18 mol%, it follows that triplet exciton diffusion can significantly enhance the efficiency loss due to TTA for x_{g} larger than approximately 5 mol%.

These experimental studies probe, inevitably, the exciton transfer processes that give rise to triplet diffusion in an ensemble-averaged manner. The development of a mechanistic and predictive model that includes the role of the energetic and positional disorder in the dilute amorphous films and the effect of thermal activation should be based on a theoretical framework for describing, at the molecular scale, the rate of exciton transfer between a donor (D) and an acceptor (A) molecule. From studies of the transfer process by Scholes *et al.* [56, 57, 26, 58], the donor-acceptor (D-A)

transfer rate k_{DA} is from a Fermi's Golden rule approach [57] given by

$$k_{\mathrm{DA}} = \frac{2\pi}{\hbar} J_{\mathrm{DA}}^2 \rho_{\mathrm{FC}}. \tag{4.1}$$

Here J_{DA} is the D-A transfer integral, which is dependent on the distance and relative orientation of the donor and acceptor, and ρ_{FC} is the Franck-Condon (FC) weighted density of vibrational states of the D-A pair. The function ρ_{FC} is a sum over all possible combinations of vibronic transitions, at the donor and acceptor molecules, that satisfy the criterion of energetic resonance: $\Delta E \equiv E_{\mathrm{DA}^*} - E_{\mathrm{D}^*\mathrm{A}} = \sum_i n_i \hbar\omega_i$, with ΔE the energy difference between the donor and acceptor triplet states, $\hbar\omega_i$ the vibron energy for mode i, and n_i the number of excited ($n_i < 0$) or absorbed ($n_i > 0$) vibrons for that mode. The asterisk indicates whether the donor or acceptor is excited by the presence of the exciton. Importantly, Eq. (1) shows that the transfer rate can be factorized. The distance dependence of k_{DA} is contained in the factor J_{DA}^2, which contains contributions due to Förster-type and Dexter-type coupling. The temperature and ΔE dependence are contained in ρ_{FC}, which contains the combined contributions of many vibron modes of each molecule. Within simplified approaches, this factor is approximated using a semi-classical approach to the triplet-vibron coupling (Marcus theory [38]), using a quantum-mechanical single-mode approach (Marcus-Levich-Jortner (MLJ) theory [65, 8]), or using the Miller-Abrahams (MA) theory [42]. For some classes of materials, the validity of these various approaches has been studied theoretically and experimentally [3, 4, 28, 35, 39]. E.g., Hoffmann *et al.* [28] found that the temperature dependence of triplet diffusion in conjugated polymers is best described by Marcus theory, with a transition to MA theory at lower temperatures. A similar conclusion was drawn by Liu *et al.* for diffusion in the disordered fluorescent small-molecule host-guest system consisting of tris(8-hydroxyquinolinato) aluminum (Alq_3) doped with 4-(dicyanomethylene)-2-methyl-6-julolidyl-9-enyl-4H-pyran (DCM2) [35]. However, for metal-organic phosphorescent emitter molecules, it is presently not clear which of these approaches is most accurate, which type of transfer process (Förster or Dexter) is predominant, and to what extent information about the detailed diffusion mechanism can be gained by studying the guest concentration and temperature dependence of the diffusion-related efficiency loss due to, e.g., concentration quenching or TTA.

Here, we present the results of a first-principles study of the triplet transfer rate k_{DA} between four iridium-cored metal-organic guest molecules that are used frequently as phosphorescent emitters in OLEDs and the resulting diffusion lengths in realistic thin films. The emitter materials studied and their emission colors are

(i) tris[2-phenylpyridinato-C^2,N]iridium(III) ($Ir(ppy)_3$, green),
(ii) bis[2-(2-pyridinyl-N)phenyl-C](acetylacetonato)-iridium(III) ($Ir(ppy)_2(acac)$, yellow-green),
(iii) bis(2-benzo[b]thiophen-2-ylpyridine)(acetyl-

acetonate)iridium(III) ($Ir(BT)_2(acac)$, yellow),
(iv) bis(2-methyldibenzo[f,h]quinoxaline)(acetylaceto-
nate)iridium(III) ($Ir(MDQ)_2(acac)$, orange-red).

For all these emitter molecules we studied the thermodynamically most stable isomers. For $Ir(ppy)_3$ this is the facial isomer, for the other three emitters we studied the *trans*-N,N isomers. Our study includes the calculation of the triplet transfer integrals J_{DA}, the FC weighted density of vibrational states ρ_{FC}, based on all the vibron energies and on the triplet-vibron coupling for all modes, and the effects of energetic and positional disorder on the diffusion coefficient. The triplet energetic disorder and triplet transfer integrals are calculated for realistic molecular geometries obtained from a Monte Carlo based simulated annealing algorithm. Two commonly used host materials are considered: 4,4'-N,N'-dicarbazole-1,1'-biphenyl (CBP) and tris(4-carbazoyl-9-ylphenyl)amine (TCTA). We show that for guest concentrations above 10 mol%, Dexter transfer is the dominant diffusion mechanism, whereas for concentrations around 10 mol%, the relative contributions of Förster and Dexter transfer depend on the emitter material. Our calculations furthermore show that for these systems Marcus theory predicts triplet transfer rates that are up to one order of magnitude too small.

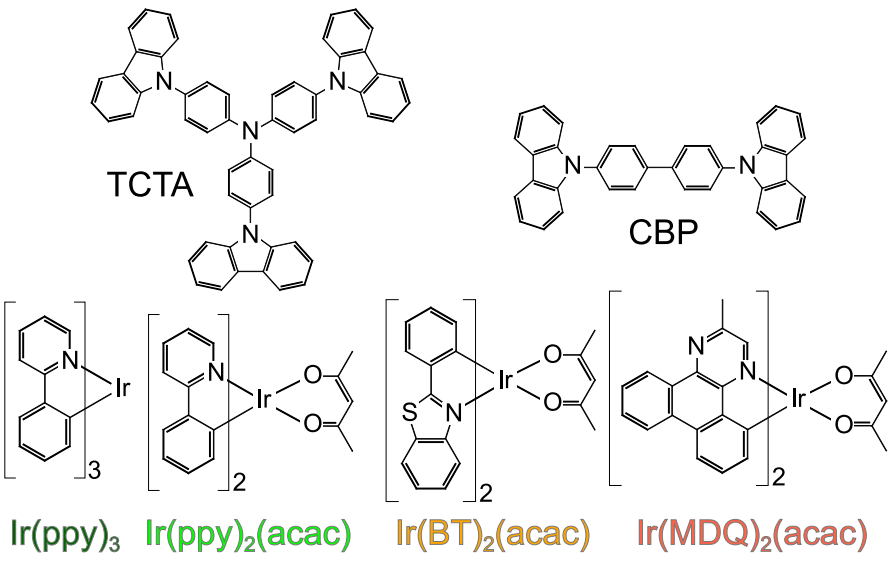

Figure 4.1: Chemical structures of the two host materials (CBP and TCTA) and four emitter materials ($Ir(ppy)_3$, $Ir(ppy)_2(acac)$, $Ir(BT)_2(acac)$, $Ir(MDQ)_2(acac)$) studied in this chapter.

The structure of the chapter is as follows. In Section 4.2 we present the *ab initio* methods used for calculating the two factors in Eq. (4.1), and the methods used for obtaining a realistic thin-film morphology with positional and energetic disorder. In Section 4.3 we present for the four iridium-cored phosphorescent emitters the calculated distance dependence of the triplet transfer rates, interpret these in terms of the commonly used Förster and Dexter models, and compare a full multi-mode approach with the results of the Marcus, MA and MLJ theory. In Section 4.4, we study the consequence of using the calculated transfer rates on the diffusion lengths in the various host-guest systems, incorporating realistic disorder in energy, position, and orientation of the molecules. Section 4.5 gives a summary and outlook.

4.2 Theoretical methods

In this section we discuss first the theoretical methods that we use to calculate the D-A transfer integrals (Subsection 4.2.1) and the FC weighted densities of vibrational states (Subsection 4.2.2). Using Eq. (4.1), this provides the transfer rates for each specific D-A pair. Subsequently, we discuss how a realistic host-guest morphology is obtained (Subsection 4.2.3), how the transition dipole moments are calculated (Subsection 4.2.4), and how the guest concentration and temperature dependent diffusion coefficient is obtained (Subsection 4.2.5).

4.2.1 Triplet transfer integrals

The triplet exciton transfer integral, J_{DA}, consists of a Coulomb and an exchange contribution [16, 57]. The Coulomb contribution can be approximated well by Förster theory [21] when the donor-acceptor distance is sufficiently large with respect to the donor and acceptor molecule size [55]. At guest concentrations used in typical OLEDs ($x_{\mathrm{g}} \leq 10$ mol%) this condition is satisfied. The process associated with the exchange contribution is Dexter transfer [16]. In purely organic molecular materials, triplet transfer is governed by the Dexter process because the Coulomb contribution to the transfer integral vanishes due to spin conservation. However, for the iridium-cored metal-organic emitter molecules considered in this chapter the admixture of singlet character in triplet exciton states is strong enough to facilitate significant Förster transfer. Förster theory describes the Coulomb coupling of excitons as a dipole-dipole interaction [55],

$$J_{\mathrm{DA,Förster}} = \frac{1}{4\pi\epsilon_0\epsilon_{\mathrm{r}}} \frac{\kappa\mu_{\mathrm{D}}\mu_{\mathrm{A}}}{R^3}, \tag{4.2}$$

with μ_{D} and μ_{A} the transition dipole moments of the donor and acceptor molecule, respectively, ϵ_0 the vacuum dielectric permittivity, ϵ_{r} the relative dielectric constant of the host-guest system, and κ an orientational factor given by

$$\kappa = \vec{\mu}_{\mathrm{D}} \cdot \vec{\mu}_{\mathrm{A}} - 3(\vec{\mu}_{\mathrm{D}} \cdot \vec{R})(\vec{\mu}_{\mathrm{A}} \cdot \vec{R}). \tag{4.3}$$

Within first order perturbation theory, the Dexter transfer integral $J_{\mathrm{DA,Dexter}}$ is equal to the direct exchange integral $J_{\mathrm{DA,exchange,d}}$, between the excited donor ($\mathrm{D^*A}$) and the excited acceptor ($\mathrm{DA^*}$) states. In order to obtain this contribution, the coupling matrix elements of emitter molecule dimers were calculated using the Löwdin orthogonalization based on single-molecule Kohn-Sham molecular orbitals and the Fock and overlap matrix from the molecular dimer [37, 25].

Previous studies have shown that contributions of intermediate charge transfer (CT) states of the type $\mathrm{D^+A^-}$ or $\mathrm{D^-A^+}$ can strongly enhance the transfer integral for Dexter coupling [57, 67]. We add the contribution of intermediate CT states to the total transfer integral for Dexter coupling as described in Ref. 67:

$$\begin{aligned} J_{\mathrm{DA,Dexter}} = {} & J_{\mathrm{DA,exchange,d}} \\ & + \frac{1}{2} \sum_{\text{CT states}} J_{\mathrm{D,CT}} J_{\mathrm{CT,A}} \left[\frac{1}{E_{\mathrm{CT}} - E_{\mathrm{T}}^{\mathrm{D}}} - \frac{1}{E_{\mathrm{CT}} - E_{\mathrm{T}}^{\mathrm{A}}} \right], \end{aligned} \tag{4.4}$$

where the coupling integrals to the CT states are given by $J_{\mathrm{D,CT}}$ and $J_{\mathrm{CT,A}}$, and the energies of the donor and acceptor triplet and CT states by $E_{\mathrm{T}}^{\mathrm{D}}$, $E_{\mathrm{T}}^{\mathrm{A}}$ and E_{CT}, respectively. We show in Section 4.3 that for the iridium-cored emitters studied in this chapter the CT-state contributions enhance the Dexter transfer integrals significantly.

4.2.2 Vibronic coupling

The FC weighted density of vibrational states ρ_{FC} in Eq. (4.1) sums over all possible combinations of vibrational modes of both molecules that enable the triplet transfer. The triplet-vibron coupling is often described using Marcus theory, within which the coupling to vibrational modes is treated semi-classically. The transfer rate is then given by $k_{\mathrm{DA,Marcus}} = (2\pi/\hbar) J_{\mathrm{DA}}^2 \rho_{\mathrm{Marcus}}$, with

$$\rho_{\mathrm{Marcus}} = \frac{1}{\sqrt{4\pi\lambda k_{\mathrm{B}} T}} \exp\left(-\frac{(\Delta E + \lambda)^2}{4\lambda k_{\mathrm{B}} T} \right), \tag{4.5}$$

where k_{B} is the Boltzmann constant, T the temperature and λ the reorganization energy. Within a harmonic approximation, the reorganization energy is equal to a sum over all the vibron mode energies, weighted by their dimensionless coupling strength S_i, the Huang-Rhys parameter:

$$\lambda = 2 \sum_i S_i \hbar \omega_i. \tag{4.6}$$

The factor 2 accounts for the modes of the donor and acceptor molecules, under the assumption that the mode energies and couplings are the same for both molecules. It has been recognized by Siders and Marcus [59] that the Marcus theory does not yield

correct results for the case of strong coupling ($S_i > 1$) to modes with relatively high energy, i.e., when $\hbar\omega_i > 0.05$ eV, well above $k_{\mathrm{B}}T$ at room temperature.

Exciton transfer for coupling to a single high-energy mode is described within the Marcus-Levich-Jortner (MLJ) theory [65, 8]. Historically, a restriction to a single-mode formulation has often been made in view of the intractable number of degrees of freedom in ρ_{FC} when including combinations of all vibron modes in the molecules. Another limiting factor is the calculation of the vibron modes and vibron couplings for medium-sized molecules ($\sim$ 100 atoms). Using modern computational methods and resources both issues can be tackled. Vibron energies and couplings can be calculated for large molecules using density functional theory (DFT). Calculating ρ_{FC} can be done by using Monte Carlo sampling techniques [11] or by transforming the problem to the time domain and numerically calculating the resulting time integral [19, 15]. Here, ρ_{FC} is calculated the method developed in Chapter 2. In this method all vibron energies ($\hbar\omega_i$) and couplings (S_i) are calculated with DFT and ρ_{FC} is transformed into an integral in the time domain that is solved numerically. The integral involves a broadening parameter (λ_{cl}), which can be physically interpreted as a very small reorganization contribution that is treated classically. This slightly broadens the vibronic levels and makes the triplet transfer energetically allowed. In Chapter 3 we showed that for small values the transfer rate is independent of λ_{cl}.

In Figure 4.2, we show ρ_{FC} for the case of coupling between identical donor and acceptor molecules, each with one quantum-mechanically treated vibron mode with an energy $\hbar\omega$, and for a combined (donor-acceptor) coupling parameter $S_{\mathrm{DA}} = 2S$. In panels (a) and (c), the vibron energy is equal to the thermal energy ($\hbar\omega = k_{\mathrm{B}}T$). In that case, and more generally for $\hbar\omega \leq k_B T$, Marcus theory provides a good approximation. In panels (b) and (d), the vibron energy is significantly ($4\times$) larger than the thermal energy so that Marcus theory no longer applies. Panel (d) corresponds to a modest vibronic coupling strength ($S_{\mathrm{DA}} = 1$), which is common for charges [15]. Panel (b) corresponds to a strong vibronic coupling strength ($S_{\mathrm{DA}} = 4$), which in Section 4.3 will be shown to be realistically applicable to triplets on the metal-organic emitter molecules studied in this chapter. The diffusion in a disordered organic material consists of a sequence of transfers between molecules with random energies, often distributed according to a Gaussian density of states. As the width (standard deviation σ_{T}) of the density of states is only approximately 0.05 eV, a typical triplet transfer process is expected to occur within the energy range -0.05 eV $< \Delta E < +0.05$ eV. Panel (d) shows that at a modest vibronic coupling strength ($S_{\mathrm{DA}} = 1$), the approximate and exact densities of states ρ_{Marcus} and ρ_{FC}, respectively, have very similar values around $\Delta E = 0$. This was found to explain why charge mobilities calculated using Marcus theory do not differ much from those calculated with a fully quantum-mechanical approach [15]. However, panel (b) shows that for a strong coupling strength, the quantum-mechanically exact rate is significantly larger than the Marcus rate. The enhancement is due to nuclear tunneling [10].

The triplet-vibron couplings of the four emitter molecules in Fig. 1 were calculated using open-shell DFT employing the B3LYP functional [7] and a def2-SVP basis set

[54], using corresponding effective core potentials as employed in the ORCA [46] package. The B3LYP functional was chosen because it has been succesfully used in calculating the lifetimes and triplet energies of iridium cored emitters [43, 18] and also performs rather well in the calculation of reorganization energies for electrons and holes [9]. The dimensionless triplet-vibron couplings (S_i) and vibron mode energies ($\hbar\omega_i$) were obtained from calculations of the Hessians and gradients in the triplet and ground state geometries, as detailed in Ref. 15 for the case of charges.

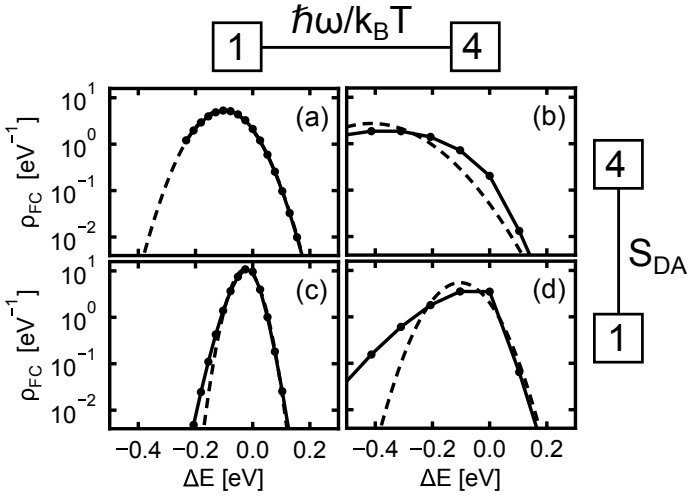

Figure 4.2: Dependence of the FC weighted density of vibrational states, to which the triplet exciton transfer rate is proportional (see Eq. (1)), on the energy difference ΔE between the final and initial state, for the case of coupling to a single quantum-mechanical mode with energy $\hbar\omega$ and with a coupling strength S ($S_{\mathrm{DA}} = 2S$). Panels (a)−(d) give the results for four combinations of these parameters. The points are prefactors at integer multiples of $\hbar\omega$ for ΔE of delta-functions in ρ_{FC} divided by $\hbar\omega$. The full lines connect these points. The dashed curves give the classical Marcus result, obtained from Eqs. (5) and (6).

4.2.3 Calculation of the morphology and energetic disorder

To generate microscopic morphologies, a Metropolis Monte Carlo based simulated annealing algorithm [47] was used to generate atomistically resolved amorphous samples of the two host and four emitter materials. We generated pure guest and mixed host-guest morphologies with a guest concentration of 10 mol%. The details of the method can be found in the appendix.

To obtain distributions of triplet energies of host and guest molecules, we performed DFT-based calculations using the Quantum Patch method [22]. These calculations were performed with open-shell DFT using the Turbomole package [2] with

the B3LYP functional [7] and def2-SVP basis set [54]. Due to the effect of the environment the energetic disorder is slightly different for the CBP, TCTA and neat film systems. In the CBP films with 10 mol% emitter, the energetic disorder is 0.058, 0.044, 0.037 and 0.052 eV for $Ir(ppy)_3$, $Ir(ppy)_2(acac)$, $Ir(BT)_2(acac)$ and $Ir(MDQ)_2(acac)$, respectively. In the 100 mol% emitter films, the energetic disorder is 0.050, 0.056, 0.032 and 0.066 eV, respectively. Details about the calculation method and triplet energies and energetic disorder values for TCTA can be found in the appendix.

4.2.4 Transition dipole moments and lifetimes

The transition dipole moments for the different emitter molecules are required in order to calculate the Förster transfer integrals as given in Eq. (4.2) and to determine the radiative lifetimes of the triplet excitons. We start with calculating the triplet energy E_T as the difference between the spin-restricted and geometrically relaxed DFT triplet state energy and the ground state DFT energy, both calculated in the zeroth order relativistic approximation (ZORA) with scalar relativistic corrections; see Table 4.1). These energies are quite close to the experimental values [33]. Next, we calculate with time-dependent DFT (TD-DFT), including spin-orbit coupling in the ZORA approximation [45], the energy splitting of the three triplet states and their transition dipole moments in the geometry of the spin-restricted DFT calculations. In the calculations, the segmented all-electron relativistically controlled (SARC) basis set for the ZORA method was used for the iridium atom [49]. For the other atoms the 6-31G basis set was used. In order to describe the effect of the environment, a conductor-like polarizable continuum model (CPCM) [50] was used with $\epsilon_\mathrm{r} = 3$, close to the relative dielectric constant measured in CBP and TCTA [36, 53], and $n = \sqrt{\epsilon_\mathrm{r}}$. All methods and basis sets are implemented in the ORCA [46] package that was used for the calculations.

Using the calculated transition dipole moments μ_i ($i = \mathrm{I}, \mathrm{II}, \mathrm{III}$), the radiative lifetime τ of the triplet states can be calculated by [43, 48, 63]

$$\frac{1}{\tau_i} = \frac{4}{3}\,\frac{\mu_i^2 n^2}{4\pi\epsilon_0\hbar}\left(\frac{E_\mathrm{T}}{\hbar c}\right)^3, \tag{4.7}$$

where, because of their small energy splittings, we can take in this expression the energies of all three triplet states equal to E_T. The lifetimes of the three triplet states are reported in Table 4.1. We assume that transitions between the three triplet states induced by vibrations occur sufficiently rapidly to establish thermal equilibrium in the occupations of the three triplet levels before decay of the exciton or transfer to another molecule. The Boltzmann-averaged effective radiative lifetime then becomes

$$\tau^{-1} = \frac{\tau_\mathrm{I}^{-1} + \tau_\mathrm{II}^{-1}\exp\left(\frac{-\Delta E_\mathrm{II\text{-}I}}{k_\mathrm{B}T}\right) + \tau_\mathrm{III}^{-1}\exp\left(\frac{-\Delta E_\mathrm{III\text{-}I}}{k_\mathrm{B}T}\right)}{1 + \exp\left(\frac{-\Delta E_\mathrm{II\text{-}I}}{k_\mathrm{B}T}\right) + \exp\left(\frac{-\Delta E_\mathrm{III\text{-}I}}{k_\mathrm{B}T}\right)}. \tag{4.8}$$

The average triplet lifetimes of the different emitter molecules at 300 K are given in Table 4.1, together with experimental values [33]. The calculated and experimental values are quite close. The shorter experimental lifetimes for $Ir(BT)_2(acac)$ and $Ir(MDQ)_2(acac)$ can be attributed to significant non-radiative decay rates in these molecules: the photoluminescence (PL) efficiencies of $Ir(BT)_2(acac)$ and $Ir(MDQ)_2(acac)$ are 0.65 [32] and 0.77 [20], respectively, whereas the PL efficiencies of $Ir(ppy)_3$ and $Ir(ppy)_2(acac)$ are close to 1 [29, 32].

Table 4.1: Calculated triplet energies, triplet level splittings, triplet lifetimes (Eq. (4.7)), Boltzmann-averaged lifetimes (Eq. (4.8)), and effective transition dipole moments (Eq. (4.9)) for the different emitter molecules. The values in parentheses are obtained from experiments on the emitters in a TCTA film [33] (the results in a CBP film are almost the same).

	E_T (eV)	$\Delta E_{II\text{-}I}$ (meV)	$\Delta E_{III\text{-}I}$ (meV)	τ_I (μs)	τ_{II} (μs)	τ_{III} (μs)	τ (μs)	μ (D)
$Ir(ppy)_3$	2.51(2.43)	14.6	40.6	94.8	10.4	0.15	1.26(1.22)	0.540
$Ir(ppy)_2(acac)$	2.43(2.38)	6.67	25.0	7.15	18.0	0.35	1.73(1.38)	0.411
$Ir(BT)_2(acac)$	2.16(2.23)	3.55	34.4	60.1	284	0.29	2.39(1.31)	0.490
$Ir(MDQ)_2(acac)$	2.05(2.05)	8.79	17.5	13.1	9.62	0.50	1.93(1.65)	0.474

In order to calculate the Förster transfer integrals we should use Eq. (4.2). Because the three triplet levels of the emitter molecules can all be thermally occupied (see above) we need, in principle, to average the Förster transfer integrals over all possible transitions from the three levels of the donor to the three levels of the acceptor molecule. Taking into account all the transitions between the triplet levels would involve an average over 9 different Förster transfer integrals. However, we can readily see from Table 4.1 that most of these contributions will be small, since for each molecule the lifetime of the highest triplet state (T_{III}) is at least 20 times smaller than the other lifetimes. Since the lifetime is proportional to the square of the transition dipole moment, the strongest Förster transfer integral contribution is at least 20 times larger than the other contributions. To avoid having to sum over all transitions, and having to take all the correlations in orientations of the molecules into account, we therefore only take the donor T_{III} to acceptor T_{III} Förster transfer integral into account . This assumption leads to an error in the transfer rate of at most 15% (for $Ir(MDQ)_2(acac)$), which is on the order of the diffusion length error bars (see Section 4.4). The Förster contribution to the triplet transfer rate should then be Boltzmann-weighted by the occupation of the highest triplet level. Since the rate is proportional to the fourth power of the transition dipole (assuming that $\mu_D = \mu_A$) we take as effective transition dipole moment

$$\mu = \left(\frac{\exp\left(\frac{-\Delta E_{III\text{-}I}}{k_B T}\right)}{1 + \exp\left(\frac{-\Delta E_{II\text{-}I}}{k_B T}\right) + \exp\left(\frac{-\Delta E_{III\text{-}I}}{k_B T}\right)} \right)^{\frac{1}{4}} \mu_{III}. \tag{4.9}$$

These transition dipole are given in the last column of Table 4.1.

4.2.5 Calculation of the diffusion length

Calculations of the guest concentration dependence of the triplet exciton diffusion length, L_{D}, are carried out for each of the eight host-guest systems and four pure guest sytems studied. For that purpose, we perform random walker kinetic Monte Carlo (KMC) simulations in a simulation box of $50\times50\times50$ nm^3 with periodic boundary conditions, with a morphology obtained using the morphology expansion method discussed in the appendix. Each emitter molecule in the box is assigned a triplet energy drawn from a Gaussian density of states with a standard deviation σ_{T} (see Subsection 4.2.3), a randomly chosen orientation, and the transition dipole moment given in Table 4.1. For each emitter pair, the transfer rate is obtained using Eq. (1), with the squared transfer integrals ($J^2_{\mathrm{DA}} = (J_{\mathrm{Dexter}} + J_{\mathrm{Förster}})^2$) and the FC weighted density of vibrational states ρ_{FC} calculated from the energies, distances, orientations, and transition dipole moments of the molecules in the box. After that, the random walk of a triplet exciton, introduced at a randomly chosen position, is followed throughout the simulation, until the exciton decays. After each decay a new triplet exciton is introduced, until a sufficient level of statistical accuracy is obtained.

From diffusion theory, the probability (P) distribution of diffusion distances in the positive or negative x directions is for ordered systems given by

$$P(|x|) = \frac{1}{2L_{\mathrm{D,1D}}} \exp\left[-\frac{|x|}{L_{\mathrm{D,1D}}}\right], \tag{4.10}$$

with L_{D} the one-dimensional diffusion length. For disordered molecular systems that contain a certain fraction of strongly isolated sites from which no diffusion takes place, such as the host-guest systems studied in this chapter, it is not correct anymore to obtain the diffusion length from the root-mean-square displacement [13]. However, $P(|x|)$ is still proportional to $\exp(-|x|/L_{\mathrm{D}})$. We therefore define L_{D} as the average of the values obtained from the exponential decrease of the emission profiles in the positive and negative x, y, and z directions. In order to obtain the three-dimensional diffusion length, we multiply the one-dimensional diffusion length by a factor $\sqrt{3}$, so that the diffusion lengths reported are obtained from Eq. (4.10) and $L_{\mathrm{D}} = \sqrt{3}L_{\mathrm{D,1D}}$.

4.3 Results

4.3.1 Transfer integrals

Figures 4.3(a) and 4.3(b) show for neat (100 mol% emitter) films of Ir(ppy)$_3$, Ir(ppy)$_2$(acac), Ir(BT)$_2$(acac), and Ir(MDQ)$_2$(acac) the calculated center-of-mass distance (R) dependence of the absolute values of the squared transfer integrals, for Förster-type and Dexter-type coupling, respectively. The full white curves in Fig.

4.3(a) indicate the R^{-6} distance dependence of the decay expected for Förster-type transfer. The dashed lines in Fig. 4.3(b) indicate the exponential ($\exp[-2\alpha R]$) decay expected for Dexter-type transfer, for $\alpha = 10$ nm^{-1}. Figure 4.3(b) shows that for intermolecular distances larger than 1.5 nm the transfer integrals for Förster transfer are for all emitters much larger than those for Dexter transfer. The molecular density of the films is around 1.4 nm^{-3}. In neat films, the average nearest-neighbor distance is therefore below 1 nm, so that Dexter transfer is then the dominant diffusion mechanism. This will be confirmed in Section 4.4.

Transfer integrals have also been calculated for 10 mol% films with a CBP and TCTA host (see appendix, A.3). The transfer integrals are comparable to those of the 100% systems, although the statistics is less good. At a 10% guest concentration, the average emitter-emitter separation is approximately 2 nm. One could therefore expect that Förster transfer is then the dominant diffusion mechanism. However, we will show in Section 4.4 that as a result of the randomness of the spatial distribution of emitter sites, leading locally to much shorter distances between the emitters, the Dexter transfer contribution is then still significant.

Figure 4.3(b) also shows the significance of the CT-state contributions described in Eq. (4.4). Including the CT-state coupling enhances the Dexter transfer integrals by at least two orders of magnitude. The resulting effect on the diffusion length will be discussed in Section 4.4. For Ir(MDQ)$_2$(acac), the Dexter-coupling extends over a larger distance than for the other emitters considered. The difference can be attributed to the larger molecular size of this emitter.

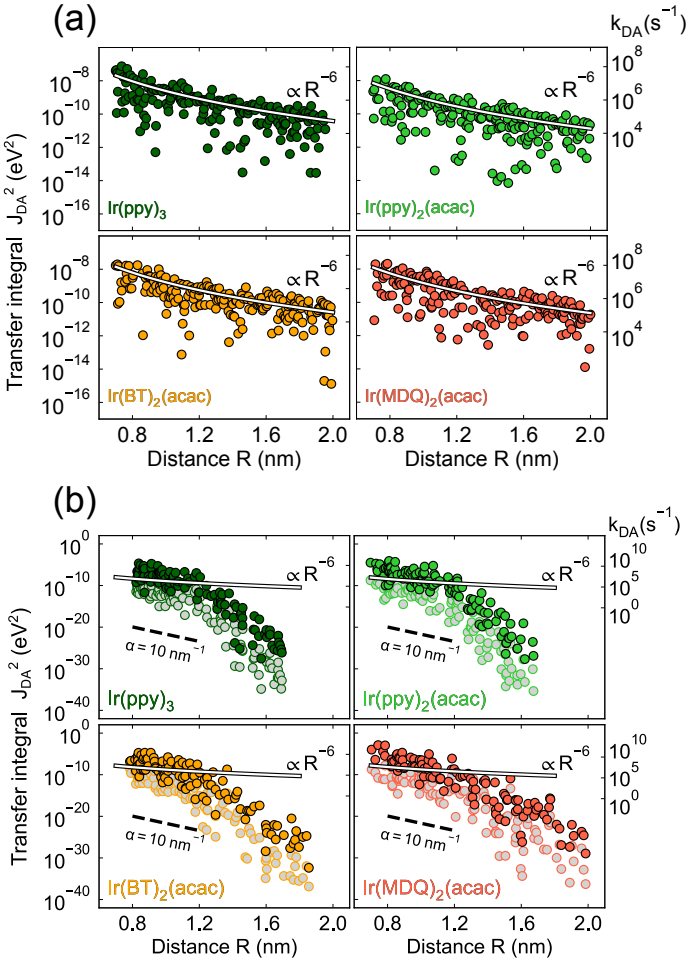

Figure 4.3: (a) Squared Förster transfer integrals for triplet excitons as a function of the center-of-mass distance between two emitter molecules, calculated for 100 mol% films of the four emitter materials studied in this chapter. The Förster transfer integrals were obtained by generating random orientations of the molecules. The white solid line shows the result for a squared orientational factor $\kappa^2 = \langle\kappa^2\rangle = 2/3$. The y-axis to the right shows the rate k_{DA} for a transfer with equal D and A triplet energies. (b) Squared Dexter transfer integrals for triplet excitons. The shaded circles show the result when neglecting the CT-state contribution in Eq. (4.4). The dashed line indicates the transfer integral decrease expected in the case of an exponential $\exp(-2\alpha R)$ distance dependence, with $\alpha = 10$ nm^{-1}. The y-axis to the right shows the rate k_{DA} for a transfer with equal D and A triplet energies. The white solid line shows the same result as in (a).

4.3.2 Vibronic coupling and energy dependence of the transfer rate

Figure 4.4(a) shows for the emitter molecules studied in this chapter the cumulative triplet-vibron coupling strength. Each step in the figure, at a vibron energy $\hbar\omega_i$, gives the contribution $\lambda_i = S_i\hbar\omega_i$ of mode i to the total reorganization energy per molecule. The figure shows that the four emitters can be separated into two groups. For $Ir(ppy)_2(acac)$ and $Ir(MDQ)_2(acac)$, vibron modes with energies around 25 meV already contribute to about half of the total reorganization energy per molecule. In contrast, for $Ir(BT)_2(acac)$ and $Ir(ppy)_3$, the high-energy vibrons that are due to C−C bond stretching, from 125 meV to 200 meV, contribute most. Furthermore, the total reorganization energy is significantly larger for $Ir(BT)_2(acac)$ and $Ir(ppy)_3$ than for $Ir(ppy)_2(acac)$ and $Ir(MDQ)_2(acac)$.

The contribution of low-energy modes, below 0.025 eV, is for all four emitters found to be very small. In contrast, modes with such low energies were found to contribute strongly to the electron-vibron and hole-vibron coupling for the purely organic materials NPB, TCTA and spiro-DPVBi [15].

Figure 4.4(b) (full curves) shows for each of the materials studied in this chapter the energy (ΔE) dependence of the triplet transfer rate for the case of Förster transfer at 300 K between two molecules at a distance of 1 nm, averaged over all combinations of relative molecular orientations (i.e., based on the transfer integral given by the white solid curve in Fig. 4.3(a)). We note that the transfer integral is not dependent on the energy difference between D and A, so that the ΔE dependence is equal for Förster and Dexter transfer. The short-dashed curves give, for comparison, the rates obtained from Marcus theory using the total reorganization energy for the transfer process, $\lambda = 2\sum_i \lambda_i$. The differences between the two groups of emitters, mentioned earlier, are evident. While the triplet transfer rate for $Ir(ppy)_2(acac)$ and $Ir(MDQ)_2(acac)$ is reasonably approximated by the Marcus rate (the deviation at $\Delta E = 0$ is approximately a factor of two), the Marcus theory underestimates for $Ir(BT)_2(acac)$ and $Ir(ppy)_3$ the rate by about one order of magnitude. At lower temperatures, the underestimation by the Marcus theory is for all iridium emitters even more pronounced. At 150 K, the underestimation by the Marcus rate is one order of magnitude for $Ir(ppy)_2(acac)$ and $Ir(MDQ)_2(acac)$ and almost three orders of magnitude for $Ir(BT)_2(acac)$ and $Ir(ppy)_3$ (see appendix, A.5). This shows that nuclear tunneling, which for charges is often only at low temperatures of importance [15], is for triplet excitons already significant at room temperatures, in particular when strongly coupled high-energy modes are involved, such as for $Ir(BT)_2(acac)$ and $Ir(ppy)_3$. Treating these modes classically, instead of quantum-mechanically, leads to a strong underestimation of the transfer rate.

Figure 4.4(b) also shows that for all systems studied the transfer rate is a smooth function of the energy difference ΔE between the final and initial states. This is due to the multi-mode nature of the triplet transfer process, as would already be expected from Fig. 4.4(a). We note that for electron or hole hopping in purely organic systems,

the rate was in some cases found to be determined predominantly by a single vibron mode, leading to an oscillatory component in the dependence on ΔE [15].

The ΔE dependence of the transfer rate is quite insensitive to the detailed contributions of individual modes. Actually, it is possible to describe the transfer as a result of coupling with a single (effective) high-energy mode, combined with coupling to a continuum of lower-energy modes. Application of the single-mode MLJ theory, with a Boltzmann factor added for $\Delta E > 0$ in order to satisfy detailed balance, then leads to an effective FC weighted vibrational density of states

$$\rho_{\mathrm{FC,eff}}(\Delta E) = \frac{1}{\hbar\omega_{\mathrm{eff}}} \frac{\exp(-S_{\mathrm{eff}})}{\Gamma\left(\Delta E/\hbar\omega_{\mathrm{eff}} + 1\right)} \exp\left(\frac{\Delta E\ \ln(S_{\mathrm{eff}})}{\hbar\omega_{\mathrm{eff}}}\right) \exp\left(-\frac{\Delta E + |\Delta E|}{2k_B T}\right), \tag{4.11}$$

corresponding to a vibronic coupling with a strength S_{eff} to a single mode with an energy $\hbar\omega_{\mathrm{eff}}$. The two effective parameters, S_{eff} and $\hbar\omega_{\mathrm{eff}}$, are obtained from a fit of $\rho_{\mathrm{FC,eff}}(\Delta E)$ to the *ab initio* function $\rho_{\mathrm{FC}}(\Delta E)$, under the constraint that $S_{\mathrm{eff}}\hbar\omega_{\mathrm{eff}} = \lambda$, with $\lambda = 2\sum_i S_i\hbar\omega_i$ the total reorganization energy. For the studied emitters, these parameters are given in Table 4.2. We note that S_{eff} contains the contributions from *both* molecules, and that the value $S_{\mathrm{eff}}/2$ per molecule is not simply equal to the ratio of the first and second vibronic emission peaks because of to the multi-mode nature of the triplet-vibron coupling. This means that the effective parameters introduced in Eq. (4.11) can not straightforwardly be obtained from emission spectra of the emitter molecules.

Figure 4.4(b) (long-dashed curves) shows that this approximation agrees well with the *ab initio* result. A first benefit of deriving the effective parameters $\hbar\omega_{\mathrm{eff}}$ and S_{eff} is that from their value the location of the transfer process in the diagram shown in Fig. 1 may be quantified. Secondly, the approximation provides a convenient method for describing the rate using a compact expression that may be readily used in, e.g., KMC device simulations. We note that the effective parameters are temperature dependent, as may be seen from Table 4.2. At lower temperature, the quantized nature of ever lower energy modes must be included, so that $\hbar\omega_{\mathrm{eff}}$ becomes smaller. S_{eff} becomes then larger, as the product $S_{\mathrm{eff}}\hbar\omega_{\mathrm{eff}}$ remains equal to the (temperature independent) reorganization energy λ. The overall effect is a predicted decrease of the transfer rate with decreasing temperature, as may be seen from the one but last column in Table 4.2 for the case of transfer with $\Delta E = 0$. However, the temperature dependence is much weaker than that following from Marcus theory (Eq. (4.5)).

Similar to our finding that for commonly used iridium-cored metal-organic phosphorescent emitters the triplet-vibron coupling is strong ($S_{\mathrm{eff}} \gg 1$), theoretical work by Pabst *et al.* has revealed that also for purely organic materials used in organic electronic devices the triplet reorganization energies are high (0.6 - 0.8 eV per D-A pair), and at least twice as large as those for electrons and holes (0.2 - 0.4 eV per

D-A pair) [34, 23]. The authors found that the triplet wave functions are considerably more localized on the molecules than the single electron or hole wave functions. Highly localized triplet wave functions lead to strong C−C bond distortions, resulting in a strong coupling with the corresponding high-energy vibrons. We find a similar trend in the case of the phosphorescent iridium molecules studied in this chapter. For $Ir(ppy)_3$ and $Ir(BT)_2(acac)$, the triplet wave function extends over the iridium core and one of the ligands, while for $Ir(ppy)_2(acac)$ and $Ir(MDQ)_2(acac)$, the triplet wave function extends over the iridium core and both of the ppy or MDQ ligands. The different degrees of delocalization are reflected in the triplet reorganization energy, which is lower for $Ir(ppy)_2(acac)$ and $Ir(MDQ)_2(acac)$, with smaller contributions from the C−C vibrons; see Fig. 4.4(a). Plots of the triplet wave functions are given in the appendix (A.4).

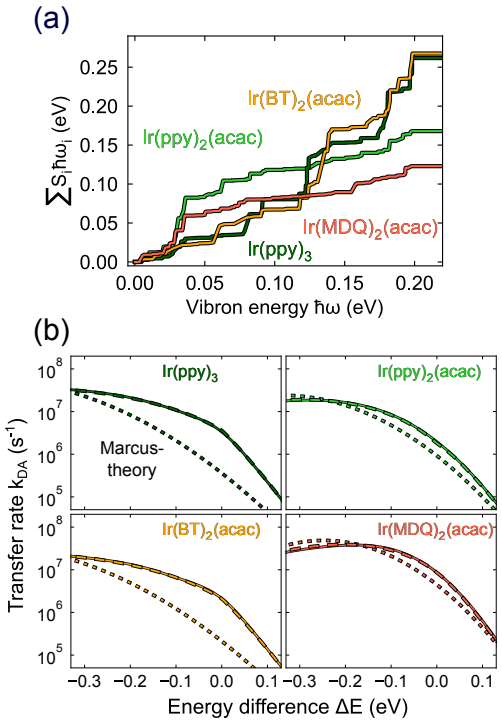

Figure 4.4: (a) Cumulative vibronic coupling energy per molecule as a function of the vibron energy for Ir(ppy)$_2$(acac) (light green), Ir(BT)$_2$(acac) (orange), Ir(ppy)$_3$ (dark green), and Ir(MDQ)$_2$(acac) (red). (b) Quantum-mechanical multi-mode rate (full curve), single-mode approximation (Eq. (4.11), dashed curve), and Marcus rate (Eq. (4.5), dotted curve) of triplet transfer for the four investigated emitters at 300 K. The Förster coupling given by Eq. (4.2) was used for two molecules at 1 nm center-of-mass distance, with $\epsilon_r = 3$, $\mu_D = \mu_A = \mu$ from Table 4.1, and $\kappa^2 = 2/3$.

4.3.3 Förster radius

In analyses of experiments probing Förster transfer, the effective (ensemble-averaged) rate is conventionally expressed as

$$k_{\text{Förster}}(R) = \frac{1}{\tau}\left(\frac{R_F}{R}\right)^6, \tag{4.12}$$

with τ the lifetime of the exciton at the donor and R_F the so-called Förster radius. At the microscopic level, the distribution of D-A transfer integrals and D-A triplet energy differences leads to a distribution of pair-specific Förster radii. The Förster

Table 4.2: Total reorganization energy λ for D-A transfer between the investigated emitters, and effective vibron energy $\hbar\omega_{\text{eff}}$ and triplet-vibron coupling strength S_{eff} at 300 K|150 K that provide with $\rho_{\text{FC,eff}}$ from Eq. (4.11) a best fit to the *ab initio* FC weighted vibrational density of states ρ_{FC} that enters Eq. (1). The one but last column gives $\rho_{\text{FC,eff}}$ for $\Delta E = 0$. The last column gives the Förster radius $R_{\text{F},0}$ for transfer with $\Delta E = 0$ from Eq. (4.13) at 300 K.

	λ (eV)	$\hbar\omega_{\text{eff}}$ (eV)	S_{eff}	$\rho_{\text{FC,eff},0}$ (eV^{-1})	$R_{\text{F},0}$ (nm)
Ir(ppy)_3	0.524	0.135|0.123	3.88|4.26	0.153|0.115	1.29
$\text{Ir(ppy)}_2\text{(acac)}$	0.336	0.085|0.061	3.95|5.51	0.226|0.066	1.22
$\text{Ir(BT)}_2\text{(acac)}$	0.535	0.133|0.127	4.02|4.22	0.134|0.116	1.31
$\text{Ir(MDQ)}_2\text{(acac)}$	0.246	0.083|0.063	2.96|3.91	0.624|0.318	1.60

radius for transfer between molecules for which $\Delta E = 0$ may from Eqs. (4.1), (4.2), (4.11), and (4.12) be written as

$$R_{\text{F},0}(\kappa) \cong \left(\frac{\kappa^2 \mu^4 \tau}{8\pi\epsilon_0^2 \epsilon_{\text{r}}^2 \hbar} \frac{\exp(-S_{\text{eff}})}{\hbar\omega_{\text{eff}}} \right)^{1/6}. \tag{4.13}$$

The Förster radii $R_{\text{F},0}$ calculated with Eq. (4.13) are reported in Table 4.2. These Förster radii are calculated at room temperature for $\kappa^2 = \langle\kappa^2\rangle = 2/3$ (the isotropic orientation value [55]). The values for μ and E_{T} are obtained from Table 4.1, and the values of $\hbar\omega_{\text{eff}}$ and S_{eff} from Table 4.2. For Ir(ppy)_3, the value of $R_{\text{F},0} = 1.29$ nm is slightly smaller than the Förster radii of 1.4 nm and 1.8 nm that were deduced by Kawamura *et al.* [30] from concentration quenching and spectral overlap measurements, respectively. For $\text{Ir(Btp)}_2\text{(acac)}$, the same experimental studies yielded Förster radii of 0.8 nm for a concentration quenching study, and 1.5 nm for a spectral overlap measurement, whereas we find a value of $R_{\text{F},0} = 1.31$ nm for the similar molecule $\text{Ir(BT)}_2\text{(acac)}$. The calculated values of the Förster radius for $\Delta E = 0$ do not include the effects of energetic relaxation in the triplet density of states. These effects can be important because in diffusion experiments and spectral overlap measurements relaxation plays a role. The role of relaxation in diffusion will be studied in the next section.

4.3.4 Dexter rate

The Dexter transfer rate is often expressed as

$$k_{\text{Dexter}}(R) = k_0 \exp(-2\alpha R), \tag{4.14}$$

where α is the wave function attenuation parameter and R is the D-A distance. The prefactor k_0 includes the vibronic factor ρ_{FC} discussed previously and a transfer integral contribution that is extrapolated to $R = 0$. In Eq. (4.14), the orientations of the donor and acceptor molecules are not taken into account. Previous results have shown that the triplet transfer integral is highly dependent on orientation [67]. This is confirmed by our calculations. At a fixed distance, the squared transfer integrals shown in Fig. 4.3(b) show a value spread of many orders of magnitude. Between 0.8 to 1.5 nm the disorder in the squared transfer integrals is much stronger than the distance dependence. Above 1.5 nm the coupling decreases rapidly, which implies that Dexter transfer with $R > 1.5$ nm practically does not occur. For the case of Dexter transfer we therefore expect diffusion over significant distances only for average guest-guest distances smaller than 1.5 nm. In the next section we will look at the emitter concentration dependence of the diffusion process and show that this is indeed the case.

4.4 Diffusion length − concentration and temperature dependence

4.4.1 KMC simulations for a realistic morphology

Figure 4.5(a) shows the results of calculations of the triplet diffusion lengths for CBP films with 10 mol% of $Ir(ppy)_3$, $Ir(ppy)_2(acac)$, $Ir(BT)_2(acac)$, and $Ir(MDQ)_2(acac)$, obtained using KMC simulations for a realistic morphology. The diffusion lengths taking into account Dexter and Förster transfer ("full") vary from 1.5 - 2.5 nm. Consistent with these small values, which are on the order of the nearest-neighbor to next-nearest-neighbour distance, we find that many triplets introduced in the system do not diffuse but decay radiatively on the molecule at which they have been generated. The figure also gives the results when including only Dexter transfer ($J_{\mathrm{DA}} = J_{\mathrm{Dexter}}$) and only Förster transfer ($J_{\mathrm{DA}} = J_{\mathrm{Förster}}$). In all cases the Dexter-only values are about a factor of two smaller than the Förster-only contributions. This can be explained by the fact that at 10 mol% the average guest-guest distance is on the order of 2 nm. As can be seen from Fig. 4.3, the squared Förster transfer integrals dominate over the Dexter transfer integrals at distances larger than 1.5 nm. The diffusion lengths with combined Dexter and Förster couplings are only slightly longer than the largest of the Dexter-only or Förster-only diffusion lengths. This can be explained by the fact that the Dexter and Förster D-A couplings can both enhance or diminish each other, depending on the relative sign of the transfer integrals.

Figure 4.5(a) also shows that the Marcus theory approximation to ρ_{FC} underestimates the diffusion length in all the emitter systems. However, the effect is not as large as might be expected from the transfer rates shown in Fig. 4.4(b), where at $\Delta E = 0$ an order of magnitude difference was found between the transfer rates obtained with the full theory for ρ_{FC} and within the framework of Marcus theory. We

ascribe this to the very wide distribution of the transfer integrals (see Figs. 4.3(a) and 4.3(b)), in combination with the relatively small probability that (in these 10 mol% films) an exciton diffuses before decaying radiatively. The diffusion process often involves at most a single, already quite improbable, transfer process. The effect of a change of the transfer rate by one order of magnitude is therefore relatively small.

The results for the 100 mol% films are shown in Fig. 4.5(b). In these neat film systems, the strong short-range Dexter coupling between nearest-neighbor molecules is the dominant process. For nearest-neighbor transfer, the squared Dexter coupling is up to four orders of magnitude larger than the squared Förster coupling. Förster coupling contributes therefore only little to the triplet transfer. As the diffusion length is in this case a result of many transfer steps, the difference between the full theory and Marcus theory is larger than for the 10 mol% films, in particular for $Ir(ppy)_3$ and $Ir(BT)_2(acac)$.

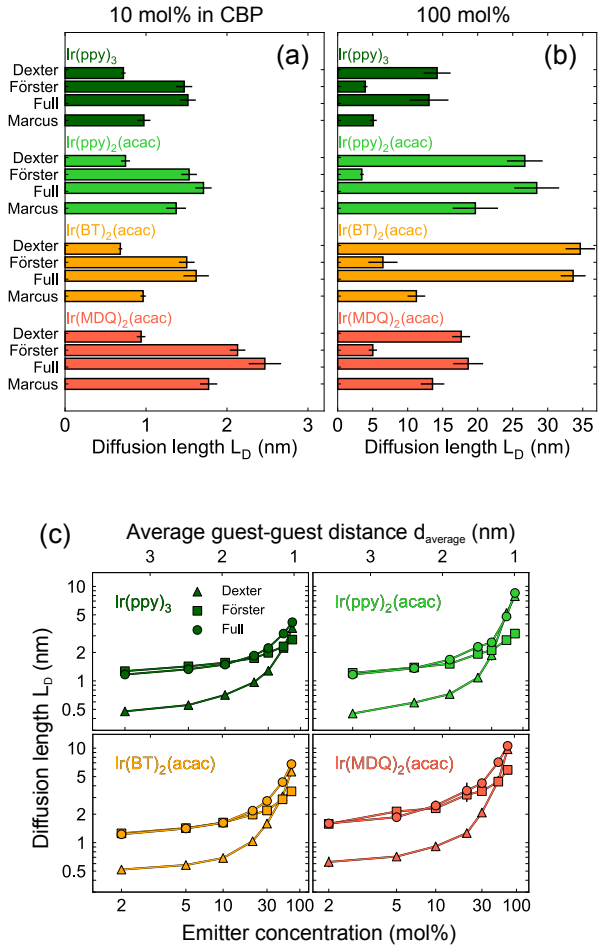

Figure 4.5: Triplet diffusion lengths at room temperature for (a) 10 mol% and (b) 100 mol% films of the four emitter materials studied in this chapter, obtained from KMC simulations for a realistic morphology. A comparison is made between results obtained using Dexter-only ($J_{\mathrm{DA}} = J_{\mathrm{Dexter}}$), Förster-only ($J_{\mathrm{DA}} = J_{\mathrm{Förster}}$), and full ($J_{\mathrm{DA}} = J_{\mathrm{Dexter}} + J_{\mathrm{Förster}}$) transfer integrals. The Marcus result shows the effect of taking $J_{\mathrm{DA}} = J_{\mathrm{Dexter}} + J_{\mathrm{Förster}}$ and using the semi-classical Marcus expression ρ_{Marcus} (Eq. (4.5)) instead of ρ_{FC}. The FC weighted density of vibrational states (ρ_{FC}) has been calculated with all the vibron contributions. The numerical uncertainty is indicated by the thin black error bars. (c) Concentration dependence of the triplet diffusion length calculated with Dexter (triangles), Förster (squares) and combined (circles) transfer integrals for the four emitter molecules in CBP. The average guest-guest distance is defined as $d_{\mathrm{average}} \equiv (c_{\mathrm{emitter}} \times n)^{-1/3}$ with n the molecular density of the film.

Figure 4.5(c) shows the emitter concentration dependence of the diffusion length, for Dexter-only, Förster-only and combined transfer. In the $2 - 10$ mol% range, the Förster contribution is dominant or at least comparable with the Dexter contribution. Above approximately 30 mol%, depending on the system, the Dexter contribution is largest.

4.4.2 Diffusion on a simple cubic lattice

In the absence of detailed structural information, the actual thin film morphology is in KMC simulations of OLEDs often replaced by a simple cubic (sc) lattice [40, 66]. In such simulations, the ΔE dependence of exciton transfer is usually described by the Miller-Abrahams (MA) theory, which does not require molecule-specific knowledge of the vibron spectra and the exciton-vibron interaction strength. The molecule-specific parameters that lead to the transfer integrals (J_{DA}) and the FC weighted density of vibrational states (ρ_{FC}), discussed in this chapter, are often unknown. Information about the exciton transfer rate can be obtained from dedicated experiments probing the effect of diffusion on the efficiency loss due to, e.g., quenching at defects or due to TTA. It is therefore of interest to compare the Förster radii that would follow from a KMC analysis of experiments probing triplet diffusion when assuming a sc lattice and thermally activated exciton transfer as described using the MA model, with the values that follow from assuming diffusion in the actual morphology and thermally activated transfer as described using the model presented in this chapter.

We consider a sc lattice with a lattice constant of 1 nm, containing 10 mol% of randomly dispersed guest molecules, assuming $\sigma_{\mathrm{T}} = 0.05$ eV. Within the MA model, the transfer rate is given by $k = k_{\mathrm{Förster}} \exp[-(\Delta E + |\Delta E|)/(2k_{\mathrm{B}}T)]$, with $k_{\mathrm{Förster}} = (1/\tau)(R_{\mathrm{F}}/R)^6$. We note that the diffusion length does not depend on τ. The simulations are carried out for $T = 300$ K. Figure 4.6 (open circles) gives the dependence of the diffusion length on R_{F}. The colored squares give for the four emitter molecules the diffusion length and the Förster radii calculated at $\Delta E = 0$ (see Section 4.3.3.) for the real morphology and using the full model for the dependence of the transfer rate on ΔE, developed in this chapter. For all emitters, the description using a sc lattice and the MA model requires the use a larger value of R_{F} than using the realistic morphology and the full model for the rates. The Förster radii that, using the sc lattice and the MA approximation, yield the best fit to the actual diffusion lengths are approximately 1.5 nm for $\mathrm{Ir(ppy)_3}$, $\mathrm{Ir(ppy)_2(acac)}$ and $\mathrm{Ir(BT)_2(acac)}$, and 2.0 nm for $\mathrm{Ir(MDQ)_2(acac)}$. The difference is due to neglecting the spatial and orientational disorder, and the use of MA theory instead of the FC weighted density of vibrational states. The latter effect is found to have the largest impact. That may be seen from the diamond symbols in Fig. 4.6, which show simulation results for a real morphology and Förster couplings but with a MA-type vibronic factor ($\rho_{\mathrm{MA}} = \rho_{\mathrm{FC,eff},0} \exp[-(\Delta E + |\Delta E|)/(2k_{\mathrm{B}}T)]$). The importance of using the full model for the rates can be understood from Fig. 4.4(b), which shows that within the full model

energetically downward transfer is favored considerably. This effect is not present in the MA rate.

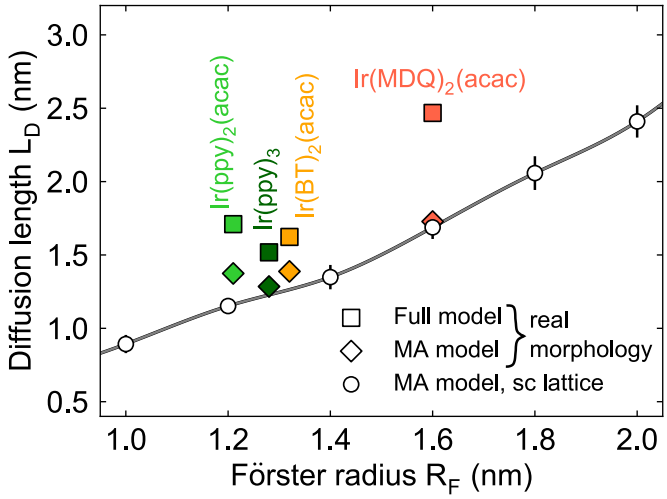

Figure 4.6: Results of KMC simulations of the triplet diffusion length for Förster-type emitter-emitter transfer as a function of Förster radius in 10 mol% emitter systems at room temperature. Colored squares: results for realistic morphologies of the four emitters embedded in CBP using the full model for the Förster transfer. The Förster radii on the x-axis are obtained from Table 4.2 ($R_{\mathrm{F},0}$). Colored diamonds: the same, but with a MA-type vibronic factor $\rho_{\mathrm{MA}} = \rho_{\mathrm{FC,eff},0} \exp[-(\Delta E + |\Delta E|)/(2k_{\mathrm{B}}T)]$, with $\rho_{\mathrm{FC,eff},0}$ from Table 4.2. Open circles connected by a curve that serves as a guide to the eye: results for a simple cubic (sc) lattice and triplet energy disorder $\sigma_{\mathrm{T}} = 0.05$ eV using Eq. (4.12) and the MA model for the energy dependence of the transfer: $k = (1/\tau)(R_{\mathrm{F}}/R)^6 \exp[-(\Delta E + |\Delta E|)/(2k_{\mathrm{B}}T)]$. Unless otherwise indicated, the uncertainties are equal to the symbol size.

4.5 Summary and conclusion

We have developed an *ab initio* model for triplet exciton diffusion due to intermolecular transfer in four phosphorescent emitters that are commonly used in OLEDs: Ir(ppy)$_3$, Ir(ppy)$_2$(acac), Ir(BT)$_2$(acac), and Ir(MDQ)$_2$(acac). Our study includes neat films and 10 mol% films formed by the commonly used host materials CBP and TCTA, containing these emitters as a guest. The triplet transfer rates and the resulting diffusion lengths are expressed as a sum of Förster and Dexter contributions, and are calculated for realistic morphologies. The effects of positional, orientational and energetic disorder are thus included. The molecular reorganization process that occurs upon triplet transfer is described by taking the coupling of triplet states with

all intramolecular vibron modes into account, by expressing the rate in terms of the full Franck-Condon weighted density of vibrational states (ρ_{FC}).

Due to the various types of disorder, the Förster and Dexter transfer integrals show both, for a given donor-acceptor distance, a wide distribution. On average, the Förster transfer integrals are larger for an average guest-guest distance above approximately 1.5 nm (20−30 mol%). The Dexter transfer integrals, which are enhanced by at least two orders of magnitude due to coupling via intermediate charge-transfer states, are strongest for average guest-guest distances smaller than 1.5 nm. Each of the four iridium emitters has its own unique vibron spectrum, with associated vibron couplings. These spectra lead in all cases studied to a dependence of the triplet transfer rate on the difference between the final and initial triplet state energies that deviates strongly from the often-used Miller-Abrahams model. Furthermore, for some cases ($\mathrm{Ir(ppy)_3}$ and $\mathrm{Ir(BT)_2(acac)}$) the transfer rate is enhanced by an order of magnitude or more as compared to the semi-classical Marcus theory.

In the 10 mol% films, the average diffusion lengths are small, close to the average intermolecular distance of around 1.5 nm. Many triplets then do not diffuse before decaying. At this concentration, Förster transfer is the predominant mechanism for all systems studied. In contrast, for 100 mol% emitter films the calculated diffusion length increases to 15−30 nm. Above 30−40 mol% Dexter transfer is the dominant mechanism, and the Förster contribution becomes unimportant. For $\mathrm{Ir(ppy)_3}$ and $\mathrm{Ir(BT)_2(acac)}$, Marcus theory underestimates the diffusion length then by a factor of 2−3.

Finally, we have "translated" the results of our study to KMC simulations assuming a simple cubic lattice and assuming thermally activated exciton transfer as described within the Miller-Abrahams theory, as is commonly done in OLED device simulations. We find that a description of Förster-type diffusion leading to the same diffusion length as obtained from our *ab initio* study would require the use of Förster radii of approximately 1.5 nm for $\mathrm{Ir(ppy)_3}$, $\mathrm{Ir(ppy)_2(acac)}$ and $\mathrm{Ir(BT)_2(acac)}$, and 2.0 nm for $\mathrm{Ir(MDQ)_2(acac)}$. These values are 0.2−0.4 nm larger than obtained within our full theory. The difference is mainly due to the use of the Miller-Abrahams rate, which does not account for the favoring of transfers down in energy as in the full theory.

This chapter unveils the importance of molecule-specific parameters, such as transfer integrals, energetic disorder and triplet-vibron couplings, in the calculation of triplet diffusion in host-guest systems. Although many different stable and functional iridium-cored phosphorescent emitters have been discovered [64], the molecular parameters determining the transfer rates between these molecules have long remained unknown. The calculational method presented in this chapter is expected to support exploring novel routes towards engineering triplet-vibron coupling in order to increase or decrease triplet diffusion.

Appendix

A.1 Morphology expansion

To generate atomistically resolved amorphous morphologies, the film formation process was simulated by depositing molecules individually on a substrate, followed by relaxation of the molecular positions and orientations using a Metropolis Monte Carlo based simulated annealing algorithm (DEPOSIT code, [47]). We generated pure host, pure guest and mixed host-guest morphologies with a mixing ratio of 10 mol%. During the vapor deposition simulations, single molecules are added sequentially to the simulation box. Each molecule undergoes a series of 10 simulated annealing cycles with 140,000 Monte Carlo steps per cycle. In each cycle the molecule is cooled down from 4000 K to room temperature. After deposition, the atomic positions are fixed and added to the growing thin film that acts as the substrate for the next molecules. We use periodic boundary conditions in the x- and y-directions, which are perpendicular to the growth (z-) direction. The force field used in the deposition simulations contains intermolecular Lennard-Jones and electrostatic interactions as well as intramolecular dihedral degrees of freedom, which are parameterized using density functional theory (DFT) calculations (B3-LYP/def2-SV(P) level of theory). Atomic partial charges and equilibrium geometries are obtained using the same level of theory.

These growth simulations lead to mesoscopic morphologies consisting of ∼1000 molecules. Each morphology is characterized by a radial distribution function (RDF, the normalized probability density of finding a neighbor molecule at a certain (center-of-mass) distance) and a nearest-neighbor distribution function (NNDF, the probability of finding the first nearest-neighbor within a given distance). In order to scale up to larger simulation boxes (∼50×50×50 nm) we attempted to use the method of Ref. 6. However, we were not able to reproduce the shape of the RDF with this method. We attribute this to the fact that the microscopic morphologies are relatively well ordered. The high first peak in the RDF (see the next section) suggests a hard-sphere packing like morphology. Such a morphology is hard to reproduce using the method of Ref. 6. We therefore use an alternative method, more attuned to a hard-sphere system as described in the chapter 2.

The optimized parameter sets $\{\mu_r,\ \sigma_r\}$ that are obtained from this procedure, applied to 100% films of the emitter molecules, are given in Table 4.3. For the 10 mol% films, with CBP as the host material, the 100 mol% morphologies were diluted such that the density of emitter molecules matches the density of emitter molecules in the 10 mol% microscopic morphologies. The same procedure was followed for 10 mol% with TCTA as the host material, except for $Ir(MDQ)_2(acac)$ in TCTA. For that case, the match with the microscopic morphology was found to be nonsatisfactory. A satisfactory match was found by using in that case the parameters $\mu_r = 0.6$ nm and $\sigma_r = 0.13$ nm.

The method is used to generate $50 \times 50 \times 50$ nm^3 simulation boxes of mesoscopic morphologies. The film densities are chosen such that they reproduce the average

layer density of the microscopic morphologies generated using the DEPOSIT software. The average layer density is chosen because of the open boundary condition in the film growth (z) direction. The radial distribution functions (RDF) and the nearest neighbour distribution functions (NNDF) of the generated mesoscopic morphologies are in good agreement with the distribution functions of the microscopic morphologies. Figures 4.7, 4.8, and 4.9 provide for the four emitters studied in this chapter a comparison of the mesoscopic RDFs and NNDFs (red) with the results obtained from the microscopic morphologies generated with the DEPOSIT code (blue) for the neat (100 mol%) films and the films with 10 mol% emitters in CBP and in TCTA, respectively.

Table 4.3: Normal distribution parameters used for generating the mesoscopic morphologies of the 100 mol% phosphorescent emitter films.

	μ_r (nm)	σ_r (nm)
$Ir(ppy)_3$	0.61	0.09
$Ir(ppy)_2(acac)$	0.52	0.11
$Ir(BT)_2(acac)$	0.60	0.10
$Ir(MDQ)_2(acac)$	0.38	0.19

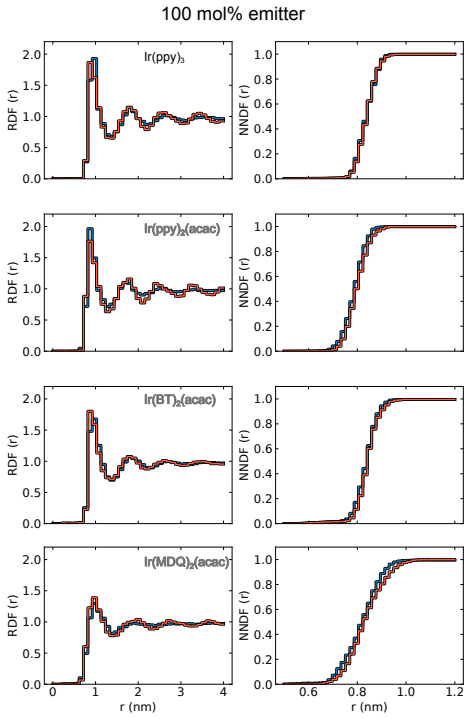

Figure 4.7: Radial distribution function (RDF) and nearest-neighbor distribution function (NNDF) of mesoscopic neat film morphologies generated by the method described in the previous section (red), and microscopic morphologies generated using the DEPOSIT code (blue).

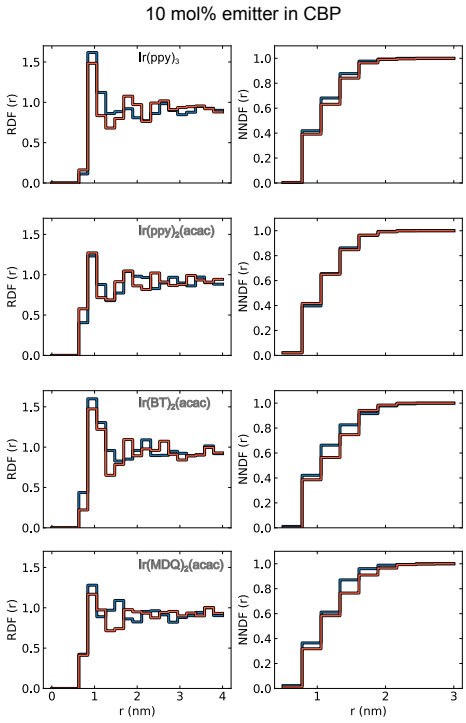

Figure 4.8: Radial distribution function (RDF) and nearest-neighbor distribution function (NNDF) of mesoscopic morphologies of films with 10 mol% emitter in CBP generated by the method described in the previous section (red), and microscopic morphologies generated using the DEPOSIT code (blue).

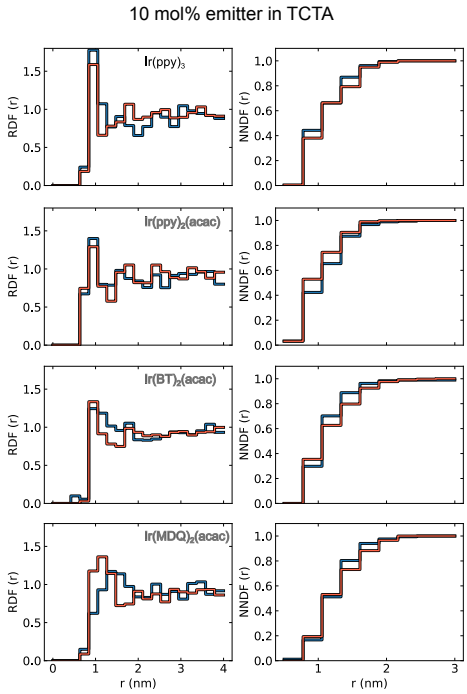

Figure 4.9: Radial distribution function (RDF) and nearest-neighbor distribution function (NNDF) of mesoscopic morphologies of films with 10 mol% emitter in TCTA generated by the method described in the previous section (red), and microscopic morphologies generated using the DEPOSIT code (blue).

A.2 Triplet energies and energetic disorder

To obtain distributions of triplet energies of host and guest molecules, we performed DFT-based calculations using the Quantum Patch method [22]. The mean and width of the triplet energy distribution depends on the conformational variability of molecules in the amorphous thin films as well as on the electrostatic interaction between the molecules. Conformational reorganization of excited molecules in the triplet state occurs on a fs to ps timescale, whereas typical residence times of a triplet exciton on a molecule are much longer ($\sim$ 1 μs). To account for the reorganization effect on the triplet energy distribution, we iteratively and self-consistently optimized the geometry of randomly selected molecules in the center of the morphologies, including steric interaction effects between the molecules, using DFT calculations of single molecules embedded in atom-centered pseudo-potentials modelling their respective environment. The triplet energies used for the kinetic Monte Carlo simulations of the

triplet diffusion were obtained using the total energy difference between the emitter molecules in their stucturally relaxed triplet state and in their structurally relaxed ground state. The triplet energetic disorder values (σ_T) are calculated by fitting a Gaussian function to a sample of emitter molecule triplet energies. Because of the effect of the environment the energetic disorder is slightly different for the CBP, TCTA and neat film systems. Triplet energies and energetic disorder values are reported in Table 4.4.

Table 4.4: Calculated triplet energies (E_T) and energetic disorder (σ_T) for films with 10 mol% emitter in CBP and TCTA, and the neat 100 mol% films. The calculations were performed using the embedded DFT method described in the text. The energetic disorder has been determined from a sample of 50 emitter molecules for the neat films and 25 emitter molecules for the CBP and TCTA films.

	10 mol% in CBP		10 mol% in TCTA		100 mol%	
	E_T (eV)	σ_T (eV)	E_T (eV)	σ_T (eV)	E_T (eV)	σ_T (eV)
$Ir(ppy)_3$	2.62	0.058	2.60	0.044	2.60	0.050
$Ir(ppy)_2(acac)$	2.52	0.044	2.51	0.045	2.51	0.056
$Ir(BT)_2(acac)$	2.31	0.037	2.31	0.036	2.29	0.032
$Ir(MDQ)_2(acac)$	2.23	0.052	2.23	0.076	2.20	0.066

A.3 Dexter transfer integrals for 10 mol% emitters in CBP and TCTA

The Dexter transfer integrals shown in the main text are calculated for emitter molecule pairs in a neat film morphology. Figure 4.10 displays the transfer integrals as calculated in the 10 mol% films, with CBP and TCTA hosts. Their values are found to be essentially identical to those for the neat films, albeit that the statistics is low. For that reason, the analyses given in the main text are based on the results obtained for neat films.

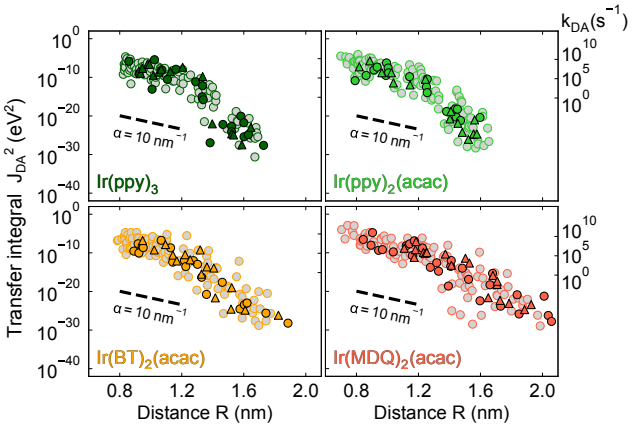

Figure 4.10: Squared Dexter transfer integrals as a function of the center-of-mass distance between two emitters. Light-colored circles show the values for the 100 mol% films. The dark-colored circles with black (blue) edges give values calculated for films containing 10 mol% emitter in CBP (TCTA). The right vertical axis indicates the transfer rate over a 1 nm distance between donor and acceptor molecules with equal triplet energies.

A.4 Triplet wave functions

Figure 4.11 shows the triplet wavefunctions for the four emitter molecules. The calculations have been performed with open shell DFT with a def2-SVP basis set using the ORCA package [46], on triplet state optimized geometries. For $Ir(ppy)_3$ and $Ir(BT)_2(acac)$, the wave functions are localized on the iridium core atom and a single ligand. For $Ir(ppy)_2(acac)$ and $Ir(MDQ)_2(acac)$, the wave functions are spread out over the core and both ligands. The difference in localization of the triplet wavefunctions can explain the strong coupling constants related to C−C vibrational modes for $Ir(ppy)_3$ and $Ir(BT)_2(acac)$, where the structure of the ligand on which the triplet resides is more strongly distorted due to the presence of the triplet. The opposite is true for $Ir(ppy)_2(acac)$ and $Ir(MDQ)_2(acac)$, where the distortion is spread out over both ligands.

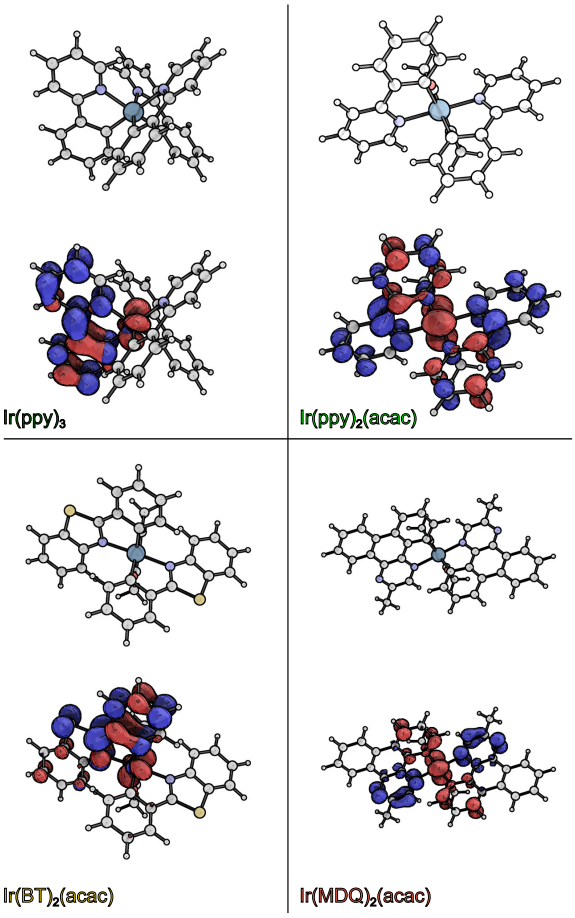

Figure 4.11: For each of the four emitters the molecular structure is plotted with (bottom) and without (top) the triplet orbitals. In the red (blue) colored regions the electron charge density is smaller (larger) than for the same molecular configuration molecule in the ground state. For the three acac emitters the acac-group has been rotated backwards in order to show more clearly the charge density distribution on the other ligands.

A.5 Energy dependence of the triplet transfer rate at 150 K

Figure 4.12 (full curves) shows for each of the emitters studied in this chapter the energy (ΔE) dependence of the triplet transfer rate for the case of Förster transfer at 150 K between two molecules at a distance of 1 nm, averaged over all combinations of the relative molecular orientations. From the figure it is clear that the Marcus theory drastically underestimates the rates at 150 K. The rapid decrease of the Marcus rate with temperature comes from the exponential temperature dependence in this rate (see Eq. (5) in the main text). The *ab-initio* calculated ρ_{FC} does not have this exponential temperature dependence because many of the vibron modes that couple strongly to the transfer are already in the quantum-mechanical tunneling regime. This weakened temperature dependence due to nuclear tunneling also occurs for charges at temperatures below room temperature [10].

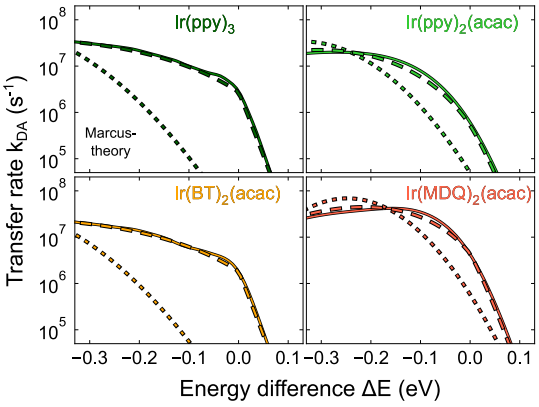

Figure 4.12: Quantum-mechanical multi-mode rate (full curve), single-mode approximation (Eq. (11) in the main text with parameters from Table II), and Marcus rate (dotted curve, Eq. (5) in the main text) of triplet transfer for the four investigated emitters at 150 K. The Förster coupling given by Eq. (2) in the main text was used for two molecules at 1 nm center-of-mass distance, with $\epsilon_{\mathrm{r}} = 3$, μ from Table I in the main text, and $\kappa = 2/3$.

A.6 Diffusion length – 10 mol% emitters in TCTA

In Figure 4.13 the diffusion lengths at room temperature obtained from KMC simulations for 10 mol% of the four emitters in TCTA are shown. The absolute values and the relative contributions from Förster and Dexter transfer are quite similar to those for 10 mol% of the emitters in CBP, shown in Fig. 5(a) of the main text.

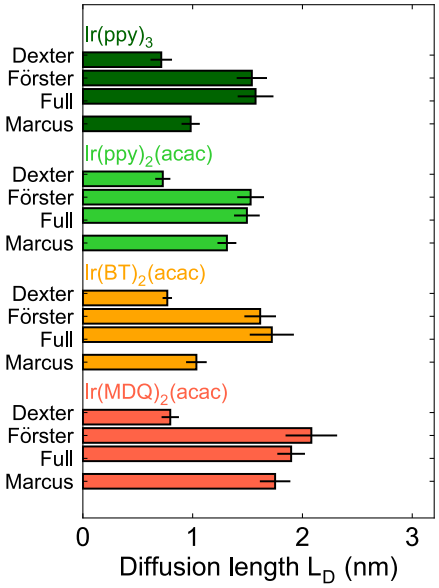

Figure 4.13: Triplet diffusion lengths at room temperature for 10 mol% films of the four emitters studied in this chapter in TCTA, obtained from KMC simulations for a realistic morphology and using a FC weighted vibrational density of states ρ_{FC} that contains all vibronic contributions. A comparison is made between results obtained using Dexter-only ($J_{\mathrm{DA}} = J_{\mathrm{Dexter}}$), Förster-only ($J_{\mathrm{DA}} = J_{\mathrm{Förster}}$) and full ($J_{\mathrm{DA}} = J_{\mathrm{Dexter}} + J_{\mathrm{Förster}}$) transfer integrals. The numerical uncertainty is indicated by the thin black error bars.

Bibliography

[1] C. Adachi, M. A. Baldo, M. E. Thompson, and S. R. Forrest. Nearly 100% internal phosphorescence efficiency in an organic light emitting device. *Journal of Applied Physics*, 90(10):5048–5051, 2001. ISSN 00218979. doi: 10.1063/1.1409582.

[2] R. Ahlrichs, M. Bär, M. Häser, H. Horn, and C. Kölmel. Electronic structure calculations on workstation computers: The program system turbomole. *Chem. Phys. Lett.*, 162(3):165 – 169, 1989. ISSN 0009-2614. doi: http://dx.doi.org/10.1016/0009-2614(89)85118-8. URL `http://www.sciencedirect.com/science/article/pii/0009261489851188`.

[3] T. S. Ahn, N. Wright, and C. J. Bardeen. The effects of orientational and energetic disorder on Forster energy migration along a one-dimensional lattice. *Chemical Physics Letters*, 446(1-3):43–48, 2007. ISSN 00092614. doi: 10.1016/j.cplett.2007.08.003.

[4] S. Athanasopoulos, E. V. Emelianova, A. B. Walker, and D. Beljonne. Exciton diffusion in energetically disordered organic materials. *Physical Review B*, 80 (19):195209, 2009. ISSN 1098-0121. doi: 10.1103/PhysRevB.80.195209. URL `https://link.aps.org/doi/10.1103/PhysRevB.80.195209`.

[5] M. A. Baldo, C. Adachi, and S. R. Forrest. Transient analysis of organic electrophosphorescence. II. Transient analysis of triplet-triplet annihilation. *Physical Review B*, 62(16):10967–10977, 2000. ISSN 01631829. doi: 10.1103/PhysRevB.62.10967.

[6] B. Baumeier, O. Stenzel, C. Poelking, D. Andrienko, and V. Schmidt. Stochastic modeling of molecular charge transport networks. *Phys. Rev. B*, 86(18):184202, nov 2012. doi: 10.1103/PhysRevB.86.184202. URL `http://link.aps.org/doi/10.1103/PhysRevB.86.184202`.

[7] A. D. Becke. A new mixing of Hartree-Fock and local density-functional theories. *The Journal of Chemical Physics*, 98(2):1372–1377, 1993. ISSN 00219606.

[8] M. Bixon and J. Jortner. Solvent relaxation dynamics and electron transfer. *Chemical Physics*, 176:467–481, 1993.

[9] C. Brückner and B. Engels. A theoretical description of charge reorganization energies in molecular organic P-type semiconductors. *Journal of Computational Chemistry*, 37(15):1335–1344, 2016. ISSN 1096987X. doi: 10.1002/jcc.24325.

[10] E. Buhks, M. Bixon, J. Jortner, and G. Navon. Quantum effects on the rates of electron-transfer reactions. *Journal of Physical Chemistry*, 85(25):3759–3762, 1981. ISSN 00223654. doi: 10.1021/j150625a010.

[11] S. Chaudhuri, S. Hedström, D. D. Méndez-Hernández, H. P. Hendrickson, K. A. Jung, J. Ho, and V. S. Batista. Electron Transfer Assisted by Vibronic Coupling from Multiple Modes. *Journal of Chemical Theory and Computation*, 13(12): 6000–6009, 2017. ISSN 15499626. doi: 10.1021/acs.jctc.7b00513.

[12] R. Coehoorn, H. Van Eersel, P. A. Bobbert, and R. A. Janssen. Kinetic Monte Carlo Study of the Sensitivity of OLED Efficiency and Lifetime to Materials Parameters. *Advanced Functional Materials*, 25(13):2024–2037, 2015. ISSN 16163028. doi: 10.1002/adfm.201402532.

[13] R. Coehoorn, P. A. Bobbert, and H. van Eersel. Effect of exciton diffusion on the triplet-triplet annihilation rate in organic semiconductor host-guest systems. *Physical Review B*, 99(2):024201, 2019. ISSN 2469-9950. doi: 10.1103/PhysRevB.99.024201. URL `https://link.aps.org/doi/10.1103/PhysRevB.99.024201`.

[14] B. W. D'Andrade, M. E. Thompson, and S. R. Forrest. Controlling Exciton Diffusion in Multilayer White Phosphorescent Organic Light Emitting Devices. *Adv. Mater.*, 14(2):147–151, 2002.

[15] X. de Vries, P. Friederich, W. Wenzel, R. Coehoorn, and P. A. Bobbert. Full quantum treatment of charge dynamics in amorphous molecular semiconductors. *Physical Review B*, 97(7):075203, 2018. ISSN 24699969. doi: 10.1103/PhysRevB.97.075203.

[16] D. L. Dexter. A theory of sensitized luminescence in solids. *The Journal of Chemical Physics*, 21(5):836–850, 1953. ISSN 00219606. doi: 10.1063/1.1699044.

[17] N. C. Erickson and R. J. Holmes. Engineering Efficiency Roll-Off in Organic Light-Emitting Devices. *Advanced Functional Materials*, 24(38):6074–6080, 2014. ISSN 16163028. doi: 10.1002/adfm.201401009.

[18] D. Escudero. Quantitative prediction of photoluminescence quantum yields of phosphors from first principles. *Chemical Science*, 7(2):1262–1267, 2016. ISSN 20416539. doi: 10.1039/c5sc03153b.

[19] M. Etinski, J. Tatchen, and C. M. Marian. Thermal and solvent effects on the triplet formation in cinnoline. *Physical Chemistry Chemical Physics*, 16(10): 4740–4751, 2014. ISSN 14639076. doi: 10.1039/c3cp53247j.

[20] C. Fan and C. Yang. Yellow/orange emissive heavy-metal complexes as phosphors in monochromatic and white organic light-emitting devices. *Chemical Society Reviews*, 43(17):6439–6469, 2014. ISSN 14604744. doi: 10.1039/c4cs00110a.

[21] T. Förster. Zwischenmolekulare Energiewanderung und Fluoreszenz. *Annalen der Physik.*, 437:55–75, 1948.

[22] P. Friederich, F. Symalla, V. Meded, T. Neumann, and W. Wenzel. Ab Initio Treatment of Disorder Effects in Amorphous Organic Materials: Toward Parameter Free Materials Simulation. *J. Chem. Theory Comput.*, 10(9):3720–3725, 2014.

[23] P. Friederich, V. Meded, A. Poschlad, T. Neumann, V. Rodin, V. Stehr, F. Symalla, D. Danilov, G. Lüdemann, R. F. Fink, I. Kondov, F. von Wrochem, and W. Wenzel. Molecular Origin of the Charge Carrier Mobility in Small Molecule Organic Semiconductors. *Advanced Functional Materials*, 26(31):5757–5763, 2016. ISSN 16163028. doi: 10.1002/adfm.201601807.

[24] R. H. Friend, R. W. Gymer, A. B. Holmes, J. H. Burroughes, R. N. Marks, C. Taliani, D. D. C. Bradley, D. A. Dos Santos, J. L. Brédas, M. Lögdlund, and W. R. Salaneck. Electroluminescence in conjugated polymers. *Nature*, 397: 121–128, 1999.

[25] R. Hamze, R. Jazzar, M. Soleilhavoup, P. I. Djurovich, G. Bertrand, and M. E. Thompson. Phosphorescent 2-, 3- and 4-coordinate cyclic (alkyl)(amino)carbene (CAAC) Cu(i) complexes. *Chemical Communications*, 53(64):9008–9011, 2017. ISSN 1364548X. doi: 10.1039/c7cc02638b.

[26] R. D. Harcourt, G. D. Scholes, and K. P. Ghiggino. Rate expressions for excitation transfer. II. Electronic considerations of direct and through-configuration exciton resonance interactions. *The Journal of Chemical Physics*, 101(12):10521–10525, 1994. ISSN 00219606. doi: 10.1063/1.467869.

[27] K. W. Hershey and R. J. Holmes. Unified analysis of transient and steady-state electrophosphorescence using exciton and polaron dynamics modeling. *Journal of Applied Physics*, 120(19), 2016. ISSN 10897550.

[28] S. T. Hoffmann, S. Athanasopoulos, D. Beljonne, H. Bässler, and A. Köhler. How do triplets and charges move in disordered organic semiconductors? A Monte Carlo study comprising the equilibrium and nonequilibrium regime. *Journal of Physical Chemistry C*, 116(31):16371–16383, 2012. ISSN 19327447. doi: 10.1021/jp305062p.

[29] Y. Kawamura, K. Goushi, J. Brooks, J. J. Brown, H. Sasabe, and C. Adachi. 100% phosphorescence quantum efficiency of Ir (III) complexes in organic semiconductor films. *Applied Physics Letters*, 86(7):071104, 2005. ISSN 00036951. doi: 10.1063/1.1862777.

[30] Y. Kawamura, J. Brooks, J. J. Brown, H. Sasabe, and C. Adachi. Intermolecular interaction and a concentration-quenching mechanism of phosphorescent ir(iii) complexes in a solid film. *Physical Review Letters*, 96(1):017404, 1 2006. ISSN 0031-9007. doi: 10.1103/PhysRevLett.96.017404.

[31] K. H. Kim, S. Lee, C. K. Moon, S. Y. Kim, Y. S. Park, J. H. Lee, J. W. Lee, J. Huh, Y. You, and J. J. Kim. Phosphorescent dye-based supramolecules for high-efficiency organic light-emitting diodes. *Nature Communications*, 5:5769, 2014. ISSN 20411723. doi: 10.1038/ncomms5769. URL `http://dx.doi.org/10.1038/ncomms5769`.

[32] S. Y. Kim, W. I. Jeong, C. Mayr, Y. S. Park, K. H. Kim, J. H. Lee, C. K. Moon, W. Brütting, and J. J. Kim. Organic light-emitting diodes with 30% external quantum efficiency based on a horizontally oriented emitter. *Advanced Functional Materials*, 23(31):3896–3900, 2013. ISSN 1616301X. doi: 10.1002/adfm.201300104.

[33] A. Ligthart, X. de Vries, L. Zhang, M. C. Pols, P. A. Bobbert, H. van Eersel, and R. Coehoorn. Effect of Triplet Confinement on Triplet–Triplet Annihilation in Organic Phosphorescent Host–Guest Systems. *Adv. Funct. Mater.*, 1804618: 1804618, 2018. ISSN 16163028. doi: 10.1002/adfm.201804618.

[34] B. C. Lin, C. P. Cheng, and Z. P. M. Lao. Reorganization energies in the transports of holes and electrons in organic amines in organic electroluminescence studied by density functional theory. *Journal of Physical Chemistry A*, 107(26): 5241–5251, 2003. ISSN 10895639. doi: 10.1021/jp0304529.

[35] X. Liu, Y. Zhang, and S. R. Forrest. Temperature dependence of the exciton dynamics in DCM2: Alq3. *Physical Review B*, 90(8):085201, 2014. ISSN 1550235X. doi: 10.1103/PhysRevB.90.085201.

[36] Z. T. Liu, C. Y. Kwong, C. H. Cheung, A. B. Djurišić, Y. Chan, and P. C. Chui. The characterization of the optical functions of BCP and CBP thin films by spectroscopic ellipsometry. *Synthetic Metals*, 150(2):159–163, 2005. ISSN 03796779. doi: 10.1016/j.synthmet.2005.02.001.

[37] P. O. Löwdin. On the Non-Orthogonality Problem Connected with the Use of Atomic Wave Functions in the Theory of Molecules and Crystals. *J. Chem. Phys.*, 18(3):365–375, 1950. doi: http://dx.doi.org/10.1063/1.1747632. URL `http://scitation.aip.org/content/aip/journal/jcp/18/3/10.1063/1.1747632`.

[38] R. A. Marcus. On the Theory of Oxidation-Reduction Reactions Involving Electron Transfer. I. *J. Chem. Phys.*, 24(5):966–978, 1956. doi: 10.1063/1.1742723.

[39] S. Matthew Menke and R. J. Holmes. Evaluating the role of energetic disorder and thermal activation in exciton transport. *Journal of Materials Chemistry C*, 4(16):3437–3442, 2016. ISSN 20507526. doi: 10.1039/c6tc00525j.

[40] M. Mesta, M. Carvelli, R. J. de Vries, H. van Eersel, J. J. M. van der Holst, M. Schober, M. Furno, B. Lüssem, K. Leo, P. Loebl, R. Coehoorn, and P. A. Bobbert. Molecular-scale simulation of electroluminescence in a multilayer white organic light-emitting diode. *Nature Mater.*, 12:652, 2013.

[41] O. V. Mikhnenko, R. Ruiter, P. W. M. Blom, and M. A. Loi. Direct Measurement of the Triplet Exciton Diffusion Length in Organic Semiconductors. *Physical Review Letters*, 108(13):137401, 2012. ISSN 0031-9007. doi: 10.1103/PhysRevLett.108.137401. URL `https://link.aps.org/doi/10.1103/PhysRevLett.108.137401`.

[42] A. Miller and E. Abrahams. Impurity Conduction at Low Concentrations. *Phys. Rev.*, 120(3):745–755, 1960.

[43] K. Mori, T. P. Goumans, E. Van Lenthe, and F. Wang. Predicting phosphorescent lifetimes and zero-field splitting of organometallic complexes with time-dependent density functional theory including spin-orbit coupling. *Physical Chemistry Chemical Physics*, 16(28):14523–14530, 2014. ISSN 14639076. doi: 10.1039/c3cp55438d.

[44] C. Murawski, K. Leo, and M. C. Gather. Efficiency roll-off in organic light-emitting diodes. *Advanced Materials*, 25(47):6801–6827, 2013. ISSN 09359648. doi: 10.1002/adma.201301603.

[45] F. Neese. Efficient and accurate approximations to the molecular spin-orbit coupling operator and their use in molecular g-tensor calculations. *Journal of Chemical Physics*, 122(3), 2005. ISSN 00219606.

[46] F. Neese. Software update: the ORCA program system, version 4.0. *Wiley Interdiscip. Rev. Comput. Mol. Sci.*, 8(1):4–9, 2018. ISSN 17590884. doi: 10.1002/wcms.1327.

[47] T. Neumann, D. Danilov, C. Lennartz, and W. Wenzel. Modeling disordered morphologies in organic semiconductors. *J. Comput. Chem.*, 34(31):2716–2725, 2013. ISSN 1096-987X. doi: 10.1002/jcc.23445. URL `http://dx.doi.org/10.1002/jcc.23445`.

[48] K. Nozaki. Theoretical Studies on Photophysical Properties and Mechanism of. *J. Chin. Chem. Soc.*, 53:101–112, 2006. ISSN 00094536. doi: 10.1002/jccs.200600013.

[49] D. A. Pantazis, X.-Y. Chen, C. R. Landis, and F. Neese. All-Electron Scalar Relativistic Basis Sets for Third-Row Transition Metal Atoms. *Journal of chemical theory and computation*, 4(6):908–919, 2008. ISSN 1549-9618. doi: 10.1021/ct800047tPM-26621232.

[50] J. Pascual-Ahuir, E. Silla, and I. Tunon. GEPOL : An Improved Description of for the Computation of a. *Journal of Computational Chemistry*, 15(10):1127–1138, 1994. ISSN 1096987X. doi: 10.1002/jcc.540151009.

[51] S. Reineke and M. A. Baldo. Recent progress in the understanding of exciton dynamics within phosphorescent OLEDs. *Physica Status Solidi (A)*, 209(12): 2341–2353, 2012. ISSN 18626300. doi: 10.1002/pssa.201228292.

[52] J. C. Ribierre, A. Ruseckas, K. Knights, S. V. Staton, N. Cumpstey, P. L. Burn, and I. D. W. Samuel. Triplet exciton diffusion and phosphorescence quenching in iridium(III)-centered dendrimers. *Physical Review Letters*, 100(1):017402, 2008. ISSN 00319007. doi: 10.1103/PhysRevLett.100.017402.

[53] A. Salehi, Y. Chen, X. Fu, C. Peng, and F. So. Manipulating Refractive Index in Organic Light Emitting Diodes. *ACS Applied Materials & Interfaces*, 10:9595, 2018. ISSN 1944-8244. URL `http://pubs.acs.org/doi/10.1021/acsami.7b18514`.

[54] A. Schäfer, H. Horn, and R. Ahlrichs. Fully optimized contracted Gaussian basis sets for atoms Li to Kr. *The Journal of Chemical Physics*, 97(4):2571–2577, 1992. ISSN 00219606.

[55] G. D. Scholes. Long range resonance energy transfer in molecular systems. *Annual Review of Physical Chemistry*, 54(1):57–87, 2003. ISSN 0066-426X. doi: 10.1146/annurev.physchem.54.011002.103746. URL `http://www.annualreviews.org/doi/10.1146/annurev.physchem.54.011002.103746`.

[56] G. D. Scholes and K. P. Ghiggino. Rate expressions for excitation transfer I. Radiationless transition theory perspective. *The Journal of Chemical Physics*, 101(2):1251–1261, 1994. ISSN 00219606. doi: 10.1063/1.467817.

[57] G. D. Scholes and K. P. Ghiggino. Electronic interactions and interchromophore excitation transfer. *Journal of Physical Chemistry*, 98(17):4580–4590, 1994. ISSN 00223654. doi: 10.1021/j100068a017.

[58] G. D. Scholes, R. D. Harcourt, and K. P. Ghiggino. Rate expressions for excitation transfer. III. An ab initio study of electronic factors in excitation transfer and exciton resonance interactions. *The Journal of Chemical Physics*, 102(24): 9574–9581, 1995. ISSN 00219606. doi: 10.1063/1.468773.

[59] P. Siders and R. Marcus. Quantum Effects in Electron-Transfer Reactions. *J. Am. Chem. Soc.*, 103(4):741–747, 1981.

[60] K. S. Son, M. Yahiro, T. Imai, H. Yoshizaki, J. Nishide, H. Sasabe, and C. Adachi. Roll-off characteristics of electroluminescence efficiency of organic blue electrophosphorescence diodes. *Japanese Journal of Applied Physics*, 47(9 PART 1):7363–7365, 2008. ISSN 00214922. doi: 10.1143/JJAP.47.7363.

[61] D. Song, S. Zhao, Y. Luo, and H. Aziz. Causes of efficiency roll-off in phosphorescent organic light emitting devices: Triplet-triplet annihilation versus triplet-polaron quenching. *Applied Physics Letters*, 97(24):243304, 2010. ISSN 00036951. doi: 10.1063/1.3527085.

[62] W. Staroske, M. Pfeiffer, K. Leo, and M. Hoffmann. Single-step triplet-triplet annihilation: An intrinsic limit for the high brightness efficiency of phosphorescent organic light emitting diodes. *Physical Review Letters*, 98(19):197402, 2007. ISSN 00319007. doi: 10.1103/PhysRevLett.98.197402.

[63] S. J. Strickler and R. A. Berg. Relationship between absorption intensity and fluorescence lifetime of molecules. *The Journal of Chemical Physics*, 37(4):814–822, 1962. ISSN 00219606. doi: 10.1063/1.1733166.

[64] M. Thompson. Mark Thompson. *MRS Bulletin*, 32(September 2007):2011, 2011. ISSN 1944-8244.

[65] J. Ulstrup and J. Jortner. The effect of intramolecular quantum modes on free energy relationships for electron transfer reactions. *The Journal of Chemical Physics*, 63(10):4358–4368, 1975. ISSN 00219606. doi: 10.1063/1.431152.

[66] H. Van Eersel, P. A. Bobbert, R. A. Janssen, and R. Coehoorn. Monte Carlo study of efficiency roll-off of phosphorescent organic light-emitting diodes: Evidence for dominant role of triplet-polaron quenching. *Applied Physics Letters*, 105(14), 2014. ISSN 00036951.

[67] J. Wehner and B. Baumeier. Intermolecular Singlet and Triplet Exciton Transfer Integrals from Many-Body Green's Functions Theory. *Journal of Chemical Theory and Computation*, 13(4):1584–1594, 2017. ISSN 15499626. doi: 10.1021/acs.jctc.6b00935.

[68] T. Yonehara, K. Goushi, T. Sawabe, I. Takasu, and C. Adachi. Comparison of transient state and steady state exciton-exciton annihilation rates based on Förster-type energy transfer. *Japanese Journal of Applied Physics*, 54(7), 2015. ISSN 13474065.

[69] L. Zhang, H. van Eersel, P. A. Bobbert, and R. Coehoorn. Analysis of the phosphorescent dye concentration dependence of triplet-triplet annihilation in organic host-guest systems. *Chemical Physics Letters*, 662:221–227, 2016. ISSN 00092614. doi: 10.1016/j.cplett.2016.07.048. URL `http://dx.doi.org/10.1016/j.cplett.2016.07.048`.

[70] Y. Zhang and S. R. Forrest. Triplet diffusion leads to triplet-triplet annihilation in organic phosphorescent emitters. *Chemical Physics Letters*, 590:106–110, 2013. ISSN 00092614. doi: 10.1016/j.cplett.2013.10.048. URL `http://dx.doi.org/10.1016/j.cplett.2013.10.048`.

[71] Y. C. Zhou, L. L. Ma, J. Zhou, X. M. Ding, and X. Y. Hou. Effect of a sensing layer on triplet exciton diffusion in organic films. *Physical Review B*, 75(13):132202, 2007. ISSN 10980121. doi: 10.1103/PhysRevB.75.132202.

Chapter 5

Exciton transfer between metal-organic phosphorescent dyes

In Chapter 4 we have investigated exciton diffusion in realistic phosphorescent host-guest systems for OLED application. We applied the Fermi's Golden Rule (FGR) transfer rate to calculate exciton transfer rates. For the calculation of the transfer integrals the short-range Dexter and long-range Förster contributions were included. We found that at guest concentrations common in OLED host-guest systems the Förster contribution to the transfer integral is dominant.

In this chapter we will again use FGR to calculate transfer rates between phosphorescent dyes. However, we will now look at exothermic transfer, e.g. transfer from a blue to a green dye. Understanding such transfers is vital for developing white OLEDs. In these white OLEDs, the transfer between different dyes is employed to generate emission from different colors in order to obtain white light. We apply the FGR to calculate Förster radii for more than 80 different donor-acceptor pairs of phosphorescent emitters. It is found that a small exothermicity partially overcomes the spectral Stokes shift, enhancing the fraction of resonant donor-acceptor pair states and thus enhancing the transfer rate. We show that a second enhancement mechanism sets in and can become significant when the exothermicity becomes larger than the Stokes shift, viz. transfer to multiple higher excited states of the acceptor molecules. Within the large set of systems studied, the Förster radius therefore tends to increase monotonically with increasing exothermicity, from around 1 nm to almost 4 nm.

5.1 Introduction

In modern-day OLEDs, the transfer of excitons plays a crucial role. Fast exciton transfer can enhance exciton quenching and can lead to an increased efficiency roll-off at high luminance levels. In phosphorescent OLEDs, triplet diffusion affects the rate of triplet-polaron quenching (TPQ) and triplet-triplet annihilation (TTA) [1, 46, 44, 45, 60, 36, 30, 11, 5, 57, 15, 59, 26]. However, the transfer of excitons can also be used to enhance the device efficiency and to simplify the device architecture. This is often referred to as exciton management. Studies on phosphorescent OLEDs showed that the generation of an exciton on a green emitter followed by the transfer to a red emitter can enhance the device efficiency and lifetime [27, 3]. An explanation for this observation is that the fast transfer to the red emitter ensures a low exciton population on the green emitter sites, which decreases the likelihood of the exciton quenching processes mentioned above. Exciton transfer is also used in OLEDs containing phosphorescent sensitizer molecules, from which excitons are transfered to fluorescent emitter molecules [14], or in OLEDs in which molecules showing thermally activated delayed fluorescence (TADF) act as sensitizers of fluorescent emitters (hyperfluorescence, [13]). Furthermore, exciton management is used to simplify white OLED device architectures. To obtain white light a multi-layer device is used in which excitons are mostly generated in the blue emissive layer. Subsequently, the excitons are transferred to adjacent green and red emitter layers to ensure emission from all three colors [19, 6, 43, 53, 55, 20, 4]. The process of tuning the layer thicknesses and emitter concentrations in such a device is crucial to ensure the right color balance to generate white light [50, 38, 9, 4, 17]. The use of computational OLED design can dramatically reduce the costs of this process. It has been shown that such computational design is actually feasible given the right mechanistic input parameters [29]. Theoretical studies on exciton transfer often focus on intramolecular Förster transfer in biological systems and polymers [41, 39, 24]. In such cases Förster transfer is in competition with "through-bond" Dexter transfer processes, since there is strong exciton-exciton wave function overlap. In contrast, in OLEDs based on small-molecule materials, intermolecular transfer is the most relevant transfer process. In a previous study we have shown that in host-guest systems often used in OLEDs, with guest concentrations of about 10 mol% or less, Förster transfer is the dominant process [52].

Here, we demonstrate how the Förster transfer rate between different phosphorescent emitters can be calculated, thereby providing a method that will allow rapid screening of new emitter molecules for favorable exciton transfer properties. The dipole-dipole type interaction leads to an R^{-6} distance (R) dependence of the donor-acceptor (D-A) transfer rate, which may be expressed as

$$k_{\mathrm{DA}} = \frac{1}{\tau_{\mathrm{D}}} \left(\frac{R_{\mathrm{F}}}{R} \right)^{6}, \tag{5.1}$$

with τ_D the emissive lifetime of the donor molecule. The Förster radius R_F contains the effects of the donor and acceptor orientations, the acceptor transition dipole moment and the donor-acceptor spectral overlap [12]. The spectral overlap depends on the broadening of all excited states due to the coupling to molecular vibrations and includes the overlap with higher excited states of the acceptor molecule. In *ab initio* calculations of the transfer rate both effects must be included. Previous studies have shown how to include the coupling of the individual intramolecular vibrations (vibrons) to the exciton transfer [42, 2]. However, most of these studies have focused on applications to crystalline molecular semiconductors and polymer systems [2, 47]. To our knowledge, the inclusion of the vibronic couplings in the exothermic transfer for molecules relevant to OLED applications has not been demonstrated. Exciton transfer to energetically higher excited states is usually not important in the case of transfer between like molecules [58, 54], but needs to be included in the case of exothermic transfer when the donor emission energy is significantly higher than the first excited state of the acceptor. Higher excited states can then be the primary acceptor states.

In general, we expect the exothermic exciton transfer rate to be enhanced with respect to that for isoenergetic transfer. The reason for this is twofold, as schematically depicted in Fig. 5.1. Firstly, the donor and acceptor Stokes shift, which in the case of isoenergetic transfer reduces the rate, is in the case of exothermic transfer at least partially overcome by the additional energy available (Fig. 5.1(a)). Secondly, an enhancement is expected when the first excited state of the donor is in resonance with energetically higher excited states of the acceptor (Fig. 5.1(b)). For the phosphorescent iridium-cored emitters studied in this chapter many of these higher excited states are expected to carry more singlet character than the three almost degenerate low-energy triplet type states. They have therefore larger transition dipole moments, leading to a large contribution to the Förster rate.

In the method for calculating the Förster radius that is presented in this chapter, we include the vibrational coupling in a manner as demonstrated in the previous chapter for the case of isoenergetic transfer. In order to properly include the higher excited states, we include now also the spin-orbit interaction. We apply the method to 84 combinations of the following 14 iridium-cored phosphorescent emitters commonly used in OLEDs:

[1] *fac*-Ir(pmp)$_3$: iridium(III)tris-(*N*-phenyl,*N*-methyl-pyridoimidazol-2-yl),

[2] *mer*-Ir(pmp)$_3$: iridium(III)tris-(*N*-phenyl,*N*-methyl-pyridoimidazol-2-yl),

[3] FIrpic: iridium(III)bis[(4,6-difluorophenyl)-pyridinato-N,$C^{2'}$]picolinate,

[4] FIr6: iridium(III)bis(4,6-difluorophenylpyridinato)tetrakis(1-pyrazolyl)borate,

[5] *fac*-Ir(ppy)$_3$: iridium(III)fac-tris(2-phenylpyridine),

[6] Ir(ppy)$_2$(acac): iridium(III)bis(2-phenylpyridine)(acetylacetonate),

[7] $Ir(dpo)_2(acac)$: iridium(III)bis(2,4-diphenyl-oxazolato-1,3-N,C 2')(acetylacetonate),

[8] $Ir(BZQ)_2(acac)$: iridium(III)bis(benzo[h]quinolinato-N,C 2')(acetylacetonate),

[9] $Ir(npy)_2(acac)$: iridium(III)bis[2-(2-naphthyl)-pyridine](acetylacetonate),

[10] $Ir(BT)_2(acac)$: iridium(III)bis(2-phenyl benzothio-zolato-N,C 2')(acetylacetonate),

[11] $Ir(MDQ)_2(acac)$: iridium(III)bis(2-methyldibenzo[f,h]quinoxaline)(acetylacetonate),

[12] $Ir(BTP)_2(acac)$: iridium(III)bis(2-(2'-benzothienyl)pyridinato-N,C 3')(acetylacetonate),

[13] $Ir(piq)_3$: iridium(III)tris(1-phenylisoquinoline),

[14] NIr: iridium(III)bis(1-pyrenyl-isoquinolinato-N,C')(acetylacetonate).

The emitters have been listed in the order of descending triplet energy, from 2.97 eV for *fac*-$Ir(pmp)_3$ down to 1.72 eV for NIr (literature values, see Table 5.1). Our study thus spans the entire optical range, and includes emitters close to the near-ultraviolet and in the near-infrared. The molecular structures are shown in Fig. 5.2(a).

The structure of this chapter is as follows. In Section 5.2, we discuss the development of an expression for the Förster transfer rate from the transition dipole moments and the Franck-Condon weighted density of states (FCWD), including the vibronic couplings, and the method for deducing the FCWD from time-dependent density functional theory (TD-DFT) calculations. In Section 5.3 we present the calculational results, including triplet energies and lifetimes for each emitter, and the Förster transfer radii for each emitter pair considered. Where possible, we compare the calculated values to measured literature data. Section 5.4 contains a summary and the outlook.

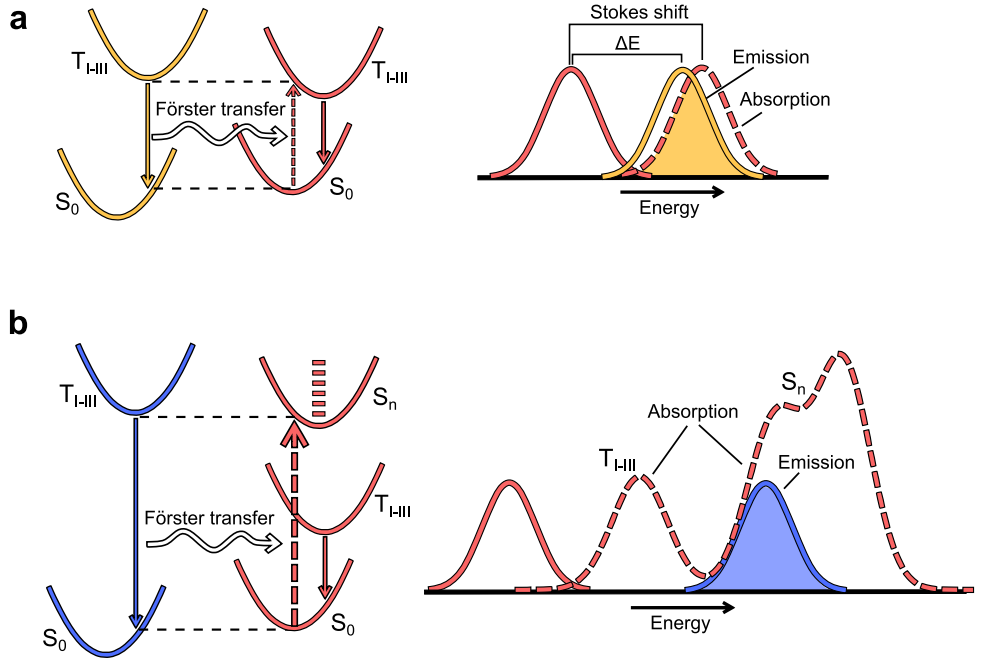

Figure 5.1: Schematic depiction of the exothermic Förster transfer mechanism studied in this chapter. Transfer to emitters with lower emission energy is expected to be enhanced by the fact that: (a) The lowest-energy states for emission and absorption, which are predominantly of triplet character ($T_{I\text{-}III}$), are in resonance due to the Stokes shifts of the donor and acceptor molecules. (b) The excitation can be transferred to energetically higher lying excited acceptor states (S_n), which in the case of the iridium emitters are expected to contain more singlet character.

5.2 Theoretical method

5.2.1 Förster transfer rate

The Förster transfer rate between a pair of donor and acceptor states is given by

$$k_{\mathrm{DA}} = \frac{2\pi}{\hbar} J_{\mathrm{DA}}^2 \rho_{\mathrm{FC}}(\Delta E_{\mathrm{DA}}). \tag{5.2}$$

Here, J_{DA} is the transfer integral, given by

$$J_{\mathrm{DA}} = \frac{1}{4\pi\epsilon_0\epsilon_{\mathrm{r}}} \frac{\kappa \mu_{\mathrm{D}} \mu_{\mathrm{A}}}{R^3}, \tag{5.3}$$

with ϵ_0 the vacuum dielectric permittivity, ϵ_r the relative dielectric constant, κ an orientational factor, and μ_D and μ_A the transition dipole moments of the donor and acceptor states, respectively [41]. In Eq. (2), ρ_FC is the Franck-Condon weighted density of vibrational states (FCWD), which is a sum over all possible combinations of vibronic transitions of the donor molecule and the acceptor molecule. The calculation of ρ_FC will be discussed in Subsection 5.2.3 ΔE_DA is the energy difference between the first excited donor and acceptor states (the "exothermicity").

In principle, exciton transfer can occur from any excited state of the donor to any excited state of the acceptor. The transfer rate between two molecules should therefore be expressed as a sum over all combinations of excited states of the donor molecule, D_i, and excited states of the acceptor molecule, A_j, weighted by the occupational probability of the donor excited state, p_{D_i}:

$$k_\mathrm{DA} = \sum_{i,j} p_{\mathrm{D}_i} k_{\mathrm{D}_i\mathrm{A}_j} = \sum_{i,j} p_{\mathrm{D}_i} \frac{2\pi}{\hbar} J_{ij}^2 \rho_{\mathrm{FC},ij}(\Delta E_{ij}), \tag{5.4}$$

with

$$J_{ij} = \frac{1}{4\pi\epsilon_0\epsilon_\mathrm{r}} \frac{\kappa_{ij}\mu_{\mathrm{D}_i}\mu_{\mathrm{A}_j}}{R^3}, \tag{5.5}$$

and

$$\Delta E_{ij} = E_{\mathrm{D}_i} - E_{\mathrm{A}_j}. \tag{5.6}$$

For the phosphorescent donor molecules discussed in this chapter, we need to consider in practice only the first three excited states (the first triplet manifold). The energetic separation between these states is at room temperature smaller than or close to $k_\mathrm{B}T$, while separation with other states is often much larger than $k_\mathrm{B}T$. The total occupational probability of these first three excited donor states is therefore often very close to 1, so that the i-summation in Eq. (5.4) can be restricted to these states. For Förster transfer between identical molecules, the terms in the j-sum in Eq. (5.4) will quickly become negligibly small because transfer to the higher excited states of the acceptor molecule requires that $\Delta E_{ij} < 0$. Such endothermic transfer is unlikely because the $\rho_{\mathrm{FC},ij}$ factor in Eq. (5.4) scales with $\exp(\Delta E_{ij}/k_\mathrm{B}T)$ for $\Delta E_{ij} < 0$ and the rate therefore decreases exponentially.

Combining Eq. (5.4) with Eq. (5.5), we obtain

$$k_\mathrm{DA} = \frac{2\pi}{\hbar} \frac{1}{(4\pi\epsilon_0\epsilon_\mathrm{r})^2} \frac{\langle\kappa^2\rangle}{R^6} \sum_{i,j} p_{\mathrm{D}_i} \mu_{\mathrm{D}_i}^2 \mu_{\mathrm{A}_j}^2 \rho_{\mathrm{FC},ij}(\Delta E_{ij}). \tag{5.7}$$

The relative dielectric constant ϵ_r will be taken equal to 3, which is close to values for common OLED host materials [28, 31, 40]. The orientational factor κ_{ij} appearing in Eq. (5.5) depends on the respective orientations of the transition dipole moments on the donor and acceptor molecule. In this chapter, we will assume random orientations, leading to $\kappa_{ij}^2 = \langle\kappa^2\rangle = 2/3$. By combining Eqs. (5.1) and (5.7) we obtain the following

expression for the Förster radius:

$$R_{\mathrm{F}} = \left(\frac{2\pi}{\hbar} \frac{\tau_{\mathrm{D}} \langle \kappa^2 \rangle}{(4\pi\epsilon_0\epsilon_{\mathrm{r}})^2} \sum_{i,j} p_{\mathrm{D}_i} \mu_{\mathrm{D}_i}^2 \mu_{\mathrm{A}_j}^2 \rho_{\mathrm{FC},ij}(\Delta E_{ij}) \right)^{1/6} . \tag{5.8}$$

In the case of exothermic Förster transfer from a donor excited state that is energetically significantly higher than the acceptor excited state, for example in the case of transfer from green to red emitter molecules, many of the terms in the sum of Eq. (5.4) involving higher acceptor excited states contribute significantly. That implies that in order to calculate the Förster transfer rate we need to calculate the transition dipole moments of the higher excited states of the acceptor molecule. In the case of iridium-cored emitters the higher excited states have more singlet character because they lie closer in energy to the pure singlet state that would be obtained in the absence of the spin-orbit interaction. As a result, these states have stronger transition dipole moments.

5.2.2 DFT calculations

The excited state energies and transition dipole moments are calculated using TD-DFT including spin-orbit coupling in the zeroth-order regular approximation (ZORA) to the Dirac equation. The calculations for the donor molecules are done in the spin-restricted DFT triplet geometry, while the calculations for the acceptor are done in the DFT ground state geometry. All calculations have been performed with the B3LYP functional, a segmented all-electron relativistically controlled (SARC) basis set for the iridium atom and the 6-31G basis set for the other atoms. For the DFT calculations the scalar relativistic ZORA correction was included. All methods are available in the ORCA package [33, 35, 34].

5.2.3 Vibronic coupling

We calculate the Franck-Condon weighted density of states (FCWD, $\rho_{\mathrm{FC},ij}$), which describes the effect of vibrational transitions on the exciton transfer rate from a state D_i to a state A_j, using the displaced harmonic oscillator model and the parallel mode approximation [2, 32, 8]. In this model, we assume that the normal mode coordinates of the final excitonic state are shifted with respect to the normal mode coordinates in the initial excitonic state.

As a first step, the normal mode displacement vector in mass-weighted coordinates ($\mathbf{K}$) has been calculated as explained in detail in section A.1 of the Appendix. Subsequently, these vectors are used to obtain the donor vibronic coupling parameters (λ_{n_i}) and acceptor vibronic coupling parameters (λ_{m_j}):

$$\lambda_{n_i} = \frac{1}{2} K_{n_i}^2 \omega_{n_i}^2 \quad \text{and} \quad \lambda_{m_j} = \frac{1}{2} K_{m_j}^2 \omega_{m_j}^2 , \tag{5.9}$$

where ω_{n_i} is the vibron frequency of mode n_i of excited state i of the donor and ω_{m_j} is the vibron frequency of mode m_j of excited state j of the acceptor. The FCWD $\rho_{FC,ij}$ involves the coupling of the exciton to the vibron modes of excited state i of the donor and vibron modes of excited state j of the acceptor. We use a time integral to evaluate $\rho_{\mathrm{FC},ij}$ at ΔE_{ij}:

$$\rho_{\mathrm{FC},ij}(\Delta E_{ij}) = \frac{1}{2\pi\hbar}\int_{-\infty}^{\infty} \exp(i\Delta E_{ij}t)\rho_{\mathrm{FC},ij}(t)dt, \tag{5.10}$$

with

$$\rho_{\mathrm{FC},ij}(t) = I_{\mathrm{D}_i}(t)I_{\mathrm{A}_j}(t), \tag{5.11}$$

where we have factorized $\rho_{FC,ij}(t)$ into a donor contribution

$$I_{\mathrm{D}_i}(t) = \exp\left(-i\sum_{n_i}\frac{K_{n_i}^2\omega_{n_i}}{\cot\left[\frac{\omega_{n_i}t}{2}\right] - \cot\left[\frac{\omega_{n_i}(t+i/k_{\mathrm{B}}T)}{2}\right]}\right), \tag{5.12}$$

and an acceptor contribution

$$I_{\mathrm{A}_j}(t) = \exp\left(-i\sum_{m_j}\frac{K_{m_j}^2\omega_{m_j}}{\cot\left[\frac{\omega_{m_j}t}{2}\right] - \cot\left[\frac{\omega_{m_j}(t+i/k_{\mathrm{B}}T)}{2}\right]}\right). \tag{5.13}$$

Equations (5.12) and (5.13) are more compact forms of the equations derived in Chapter 2, based on the work by Souza *et al.* [7]. Using the convolution theorem we can also write Eq. (5.10) as the overlap of the emission spectrum of excited state i of the donor and the absorption spectrum of excited state j of the acceptor:

$$\rho_{\mathrm{FC},ij}(\Delta E_{ij}) = \int_{-\infty}^{\infty} I_{\mathrm{D}_i}(E)I_{\mathrm{A}_j}(E)dE, \tag{5.14}$$

with $\Delta E_{ij} = E_{\mathrm{D}_i} - E_{\mathrm{A}_j}$, where

$$I_{\mathrm{D}_i}(E) = \frac{1}{2\pi\hbar}\int_{-\infty}^{\infty} \exp[i(E_{\mathrm{D}_i} - E)t]I_{\mathrm{D}_i}(t)dt, \tag{5.15}$$

and

$$I_{\mathrm{A}_j}(E) = \frac{1}{2\pi\hbar}\int_{-\infty}^{\infty} \exp\big[i(E - E_{\mathrm{A}_j})t\big]I_{\mathrm{A}_j}(t)dt. \tag{5.16}$$

5.2.4 Excited state energies and transition dipole spectra

The excited state energies of the molecules are calculated with TD-DFT for the ground state molecular geometry. These energies are the "vertical" excitation energies, E^{vert},

and are not corrected for the geometrical relaxation that happens in the excited state. We calculate these relaxation corrections, the reorganization energies

$$\lambda_{\mathrm{D}_i} = \sum_{n_i} \lambda_{n_i} \text{ and } \lambda_{\mathrm{A}_j} = \sum_{m_j} \lambda_{m_j} \tag{5.17}$$

for the donor and acceptor molecules, respectively, using the vibronic couplings and vibron mode energies as obtained in the last subsection. The adiabatic (geometrically relaxed) excitation energies are then given by

$$E^{\mathrm{adia}}_{\mathrm{D}_i} = E^{\mathrm{vert}}_{\mathrm{D}_i} + \lambda_{\mathrm{D}_i} \quad \text{and} \quad E^{\mathrm{adia}}_{\mathrm{A}_j} = E^{\mathrm{vert}}_{\mathrm{A}_j} - \lambda_{\mathrm{A}_j}. \tag{5.18}$$

In the calculation of the Förster transfer rate we only consider the first three triplet energies of the donor (see Subsection 5.2.1). The triplet energy of the donor is taken to be the lowest triplet level of the triplet manifold ($E_{\mathrm{T}} = E_{\mathrm{D}_1}$). No significant change of the final results would be obtained when selecting one of the two other states as the reference level, because the three triplets lie very close together. For the acceptor excited states we consider all excitations up to 3.1 eV, this is 0.35 eV higher than the triplet energy of the *fac*-Ir(pmp)$_3$ which has the highest emission energy at 2.76 eV. Additionally, we consider only excited states with transition dipole moments larger than 1% of the sum over all excited state transition dipole moments. This limits the computational effort with a negligible loss of accuracy.

In order to see how the various excited states of the acceptor contribute to the transfer rate we construct vibrationally broadened squared transition dipole spectra of the donor and the acceptor, defined by

$$\mu^2_{\mathrm{D}}(E) = \sum_i p_{\mathrm{D}_i} \mu^2_{\mathrm{D}_i} I_{\mathrm{D}_i}(E) \quad \text{and} \quad \mu^2_{\mathrm{A}} = \sum_j \mu^2_{\mathrm{A}_j} I_{\mathrm{A}_j}(E). \tag{5.19}$$

Combining Eqs. (5.14) and (5.19) we obtain

$$\sum_{i,j} p_{\mathrm{D}_i} \mu^2_{\mathrm{D}_i} \mu^2_{\mathrm{A}_j} \rho_{\mathrm{FC},ij}(\Delta E_{ij}) = \int_{-\infty}^{\infty} \mu^2_{\mathrm{D}}(E) \mu^2_{\mathrm{A}}(E) dE. \tag{5.20}$$

The integral on the right hand side of this equation is the determining factor in the Förster transfer rate, as can be seen from Eq. (5.7). It involves the strengths of the excited state transition dipole moments, which strongly influence the size of the Förster transfer rate. The broadening of the vibrational excited states, given by $I_{\mathrm{D}_i}(E)$ and $I_{\mathrm{A}_j}(E)$, ensures energetic overlap between the excited states when the donor and acceptor states are not in exact resonance ($\Delta E_{ij} \neq 0$). In general, the variation of the Förster transfer rate with ΔE_{ij} decreases when the vibrational broadening increases.

In Eq. (5.20) we have compressed all important molecular details involving the transfer into the separate donor and acceptor spectra. This allows for convenient

calculation of the Förster rates for many different donor and acceptor combinations. In Section A.2 in the Appendix we provide the squared transition dipole spectra for all of the 14 emitter molecules studied in this chapter. These can then be used to calculate the donor-acceptor transfer rate between any combination of emitter molecules. In the next section we show these spectra and their overlap for a selection of donor-acceptor combinations.

5.3 Results

5.3.1 Triplet energies and lifetimes

The calculated triplet energies are reported in Table 5.1 and are compared with the experimental values from the literature in Fig. 5.2(b). The comparison with the experimental values shows that in most cases the excitation energy is underestimated by about 0.1 - 0.2 eV. We note that the calculations refer to the gas-phase triplet energies, whereas the experimental values are obtained from thin-film studies. Thin-film embedding, in a polarizable environment, reduces the triplet energy. The absolute error of the gas-phase calculations is thus larger than is apparent from the figure. At least part of the error can be explained from the fact that the B3LYP functional underestimates excitation energies [22]. To our knowledge there is no detailed study of the effect on the excitation energies of different DFT functionals using the spin-orbit coupling method employed in this chapter. The systematic underestimation disappears when we look at the donor-acceptor energy difference. This is convenient, because it is this energy difference that determines the magnitude of the Förster transfer rate. The lifetimes of the individual triplet states are calculated using the Strickler-Berg expression [49]:

$$\frac{1}{\tau_i} = \frac{4}{3}\,\frac{\mu_i^2 \epsilon_\mathrm{r}}{4\pi\epsilon_0\hbar}\left(\frac{E_i}{\hbar c}\right)^3 \quad \text{with} \quad i = 1, 2, 3. \tag{5.21}$$

The lifetime of excitons in the low-energy triplet manifold is calculated assuming a Boltzmann distribution over the three triplet states.

5.3.2 Förster radii

From Eqs. (5.8) and (5.20) it follows that the Förster transfer rate is proportional to the overlap of the spectra of the squared donor and acceptor transition dipole moments $\mu_\mathrm{D}^2(E)$ and $\mu_\mathrm{A}^2(E)$, respectively. The transition dipole moment spectra follow from Eq. (5.19). As an example, Figs. 5.3(a) and (b) show the spectral overlap for the green and blue emitters $\mathrm{Ir(ppy)_3}$ and *fac*-$\mathrm{Ir(pmp)_3}$, respectively, combined with $\mathrm{Ir(ppy)_3}$, $\mathrm{Ir(dpo)_2acac}$, $\mathrm{Ir(MDQ)_2acac}$ and NIr as acceptor molecules. These four acceptor molecules follow a trend of decreasing triplet energy. The figure indeed shows that the acceptor spectra are red-shifted.

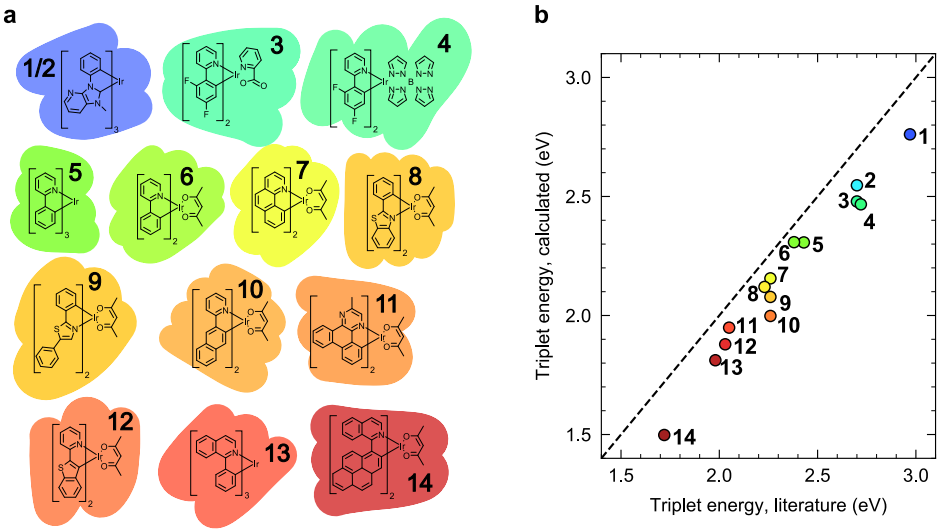

Figure 5.2: (a) Structural formulas of the iridium cored emitters studied in this chapter. From left to right and top to bottom: $Ir(pmp)_3$, FIrpic, FIr6, $Ir(ppy)_3$, $Ir(ppy)_2acac$, $Ir(BZQ)_2acac$, $Ir(BT)_2acac$, $Ir(dpo)_2acac$, $Ir(npy)_2acac$, $Ir(MDQ)_2acac$, $Ir(BTP)_2acac$, $Ir(piq)_3$ and NIr. (b) Calculated triplet energies using the TD-DFT method outlined in the text versus the experimental triplet energies reported in the literature. The symbol colors of indicate the emission colors, which range from the infrared to the deep blue. The dashed line indicates $E_{\mathrm{T}}^{\mathrm{calc}} = E_{\mathrm{T}}^{\mathrm{exp}}$. The numerical values are reported in Table 5.1.

Table 5.1: Calculated triplet energies $E_{\mathrm{T}}^{\mathrm{calc}}$ and lifetimes τ^{calc} as described in the previous sections, compared to the experimental values from the literature, $E_{\mathrm{T}}^{\mathrm{exp}}$ and τ^{exp}. The calculated lifetimes and the experimental lifetimes indicated with an asterisk refer to the radiative lifetime. Otherwise, the experimental lifetimes refer to the effective lifetime, which is in general smaller than the radiative lifetime, due to non-radiative decay.

	$E_{\mathrm{T}}^{\mathrm{calc}}$ (eV)	$E_{\mathrm{T}}^{\mathrm{exp}}$ (eV)	τ^{calc} (μs)	τ^{exp} (μs)
fac-Ir(pmp)$_3$	2.76	2.97[23]	0.81	1.6[23,*]
mer-Ir(pmp)$_3$	2.55	2.70[23]	0.55	1.0[23,*]
FIrpic	2.48	2.70[16]	2.10	1.2[16,*]
FIr6	2.47	2.72[55]	2.10	2.2[55]
Ir(ppy)$_3$	2.31	2.43[26]	1.62	1.2[18,26,*]
Ir(ppy)$_2$acac	2.31	2.38[26]	2.10	1.4[26]
Ir(BZQ)$_2$acac	2.16	2.26[10]	1.43	4.5[10]
Ir(BT)$_2$acac	2.12	2.23[26]	2.49	1.3[26]
Ir(dpo)$_2$acac	2.08	2.26[21]	5.16	3.0[21]
Ir(npy)$_2$acac	2.00	2.26[25]	7.85	9.0[25]
Ir(MDQ)$_2$acac	1.95	2.05[26]	0.90	1.7[26]
Ir(BTP)$_2$acac	1.88	2.03[18]	9.09	10.8[18,*]
Ir(piq)$_3$	1.81	1.98[37]	0.77	1.1[37]
NIr	1.50	1.72[56]	5.24	-

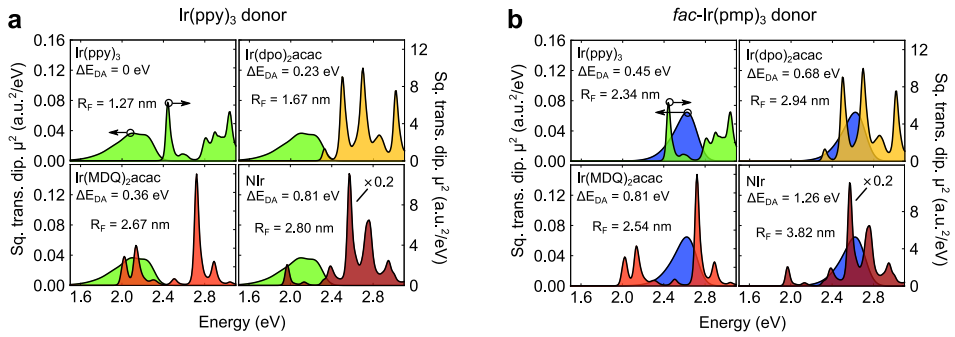

Figure 5.3: Squared transition dipole moment spectra for eight selected donor-acceptor pairs. Panels (a) and (b) show the $Ir(ppy)_3$ and *fac*-$Ir(pmp)_3$ donor spectrum, respectively, with the $Ir(ppy)_3$, $Ir(dpo)_2acac$, $Ir(MDQ)_2acac$ and NIr acceptor spectra. Each panel also gives the Förster radius for the exciton transfer in the donor-acceptor system depicted.

In Fig. 5.3(a), the overlap of the donor and acceptor spectra increases due to an increasing acceptor red-shift. As expected, this leads to a monotonic increase of the Förster radius. However, in Fig. 5.3(b), the Förster radius no longer increases monotonically with increasing exothermicity: the Förster radius for transfer from *fac*-$Ir(pmp)_3$ to $Ir(MDQ)_2(acac)$ is smaller than for transfer to $Ir(dpo)_2(acac)$. From the figure, it can be seen that this is due to unfavorable overlap for the case of transfer to $Ir(MDQ)_2(acac)$. For transfer to the near-infrared emitter NIr, the rate is again enhanced, due to favorable overlap with higher excited states.

A comparison between Figs. 5.3(a) and (b) shows that an increase of exothermicity tends to give rise to an increase of the Förster radius. However, these figures also shows that this is not a general rule, as is evident from the larger Förster radius for the transfer from $Ir(ppy)_3$ to $Ir(MDQ)_2(acac)$ (2.67 nm *versus* 2.54 nm). Again, this is due to the less favorable spectral overlap for the blue-red *fac*-$Ir(pmp)_3$ – $Ir(MDQ)_2(acac)$ donor-acceptor pair.

The Förster radius of 2.67 nm for the $Ir(ppy)_3$ to $Ir(MDQ)_2(acac)$ transfer is shorter than reported by Steinbacher *et al.* [48], who find a value of around 3 – 3.5 nm. However, the experiments done by Steinbacher are performed in PMMA, which has a relative dielectric constant of $\epsilon_r = 2$, instead of the value of $\epsilon_r = 3$ we choose in our calculations. From our calculations, we obtain for $\epsilon_r = 2$ a Förster radius of 3.06 nm, which is within the interval obtained in Ref. 48.

Figure 5.4 shows a scatter plot of the Förster transfer radii for the 84 donor-acceptor pairs investigated in this chapter. The plot shows a significant spread, which is due to the molecule-specific overlap between the donor and acceptor spectra as shown in Fig. 5.3.

The Förster radii close to $\Delta E = 0$, which corresponds to Förster transfer between

like emitter molecules, have values of 0.7 – 1.5 nm, in accordance with values reported by Kawamura *et al.* [18]. The initial increase in Förster radius in the range $\Delta E = 0$ – 0.15 eV, as indicated by (a) in Fig. 5.4, can be explained from the mechanism shown in Fig. 5.1(a). At exothermic transfer larger than approximately 0.15 eV, the excess energy is sufficient to overcome the Stokes shift. The Förster radius then increases in general further, as indicated by (b) in Fig. 5.4, due to overlap of the donor states with energetically higher excited states of the acceptor, as depicted in Fig. 5.1(b). For the largest exothermicity considered in this chapter (*fac*-Ir(pmp)$_3$ to NIr transfer), the Förster radius approaches a value of almost 4 nm. In Fig. 5.7 of the SI, similar graphs are given for systems with Gaussian excitonic disorder, characterized by standard deviations of 0.05 and 0.10 eV. We find that such disorder has only a marginal effect on the Förster radius, except when R_{F} is very small (< 1 nm) as a result of poor spectral overlap. In those cases the disorder increases the spectral overlap, leading to a significant increase in R_{F}.

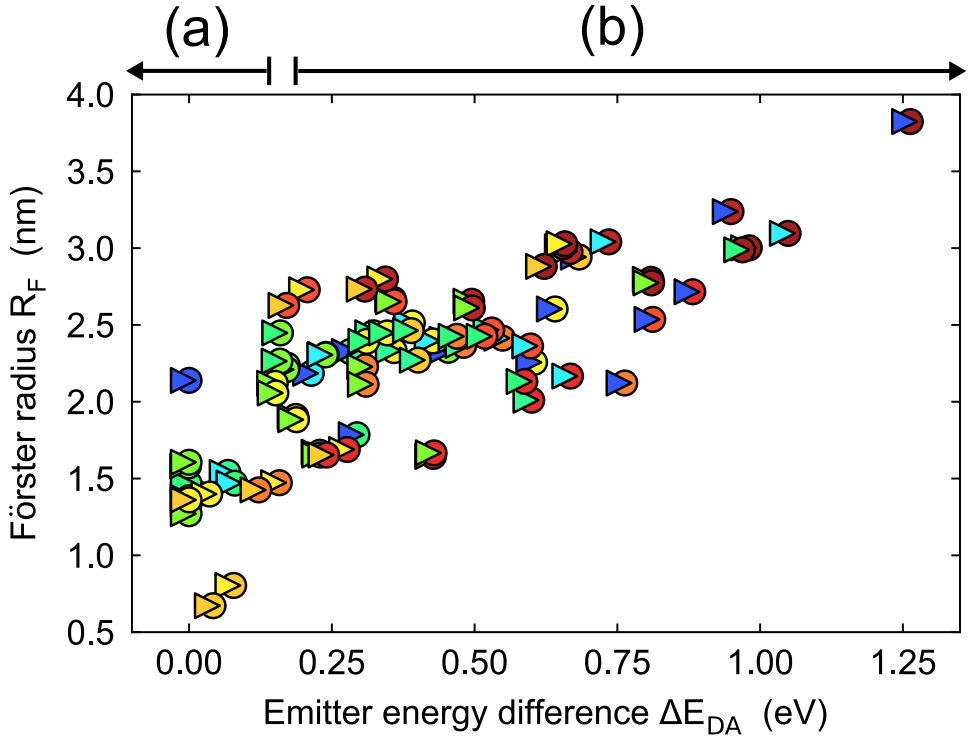

Figure 5.4: Overview of the calculated Förster radius versus donor-acceptor energy difference for the 84 systems included in this study. Every point in the graph represents a transfer process from a donor (triangle) to an acceptor (circle), with emission colors as indicated. The ΔE-regions indicated in the top part of the figure ((a) and (b)) indicate the mechanism (see Fig. 5.1) by which the exothermicity enhances R_{F}. Section A.3 of the Appendix contains a numerical overview of all data points, and Fig. 5.6 gives separate Förster transfer graphs for every donor molecule considered.

In the Förster rate formula Eq. (5.1), the donor lifetime enters separately from the Förster radius. This means that the variation in the Förster radii is only due to the different transition dipole moments of the acceptor excited states. Because the vibronic couplings broaden the spectra, their contribution is expected to smooth out the variation of the Förster radii for different ΔE_{DA}. The magnitude of the transition dipole moments of the excited states is determined by two factors. Firstly, by the magnitude of the pure singlet transition dipole moments of the emitter molecules. Secondly, by the strength of the spin-orbit coupling, which mixes the singlet and

triplet excited states. It is known that excited states with more metal-ligand-charge-transfer (MLCT) character have stronger spin-orbit coupling than those with more ligand-centered (LC) character [51]. In general, it can be seen that higher excited states have larger transition dipole moments. This can be attributed to the increased singlet character of energetically higher-lying excitations.

5.4 Summary and outlook

In this chapter we investigated the exothermic Förster transfer between 14 different phosphorescent emitters commonly used in OLEDs. We have developed a rate expression that includes the coupling of multiple excited states of the donor and acceptor, which is necessary to correctly describe the transfer process. Quantitative predictions of energies, lifetimes and Förster radii for the different emitters and donor-acceptor transfer are given. In accordance with experimental work we find that the exothermic transfer is enhanced with respect to the isoenergetic transfer. This enhancement was explained by two effects. Firstly, the excess energy in the exothermic transfer compensates for the Stokes shift of the donor and acceptor energy levels. Secondly, at sufficient excess energy, the energetically higher excited states of the acceptor are accessible in the transfer, which further enhances the transfer rate.

The rate expression and calculations performed in this chapter can serve as input for device models that include energetic, spatial and orientational disorder. This paves the way for *in silico* design and optimization of, for example, white OLED device structures [19, 6, 43, 53, 55, 20, 4] and TADF sensitizer OLED architectures [13, 14]. For the emitters studied in this chapter, we have provided the squared transition dipole moment spectra. The overlap of these spectra can be numerically integrated to yield Förster radii for all the emitter combinations. These results can then be directly applied in OLED device simulations.

We have shown how the Förster radius for exciton transfer is sensitively determined by the electronic and vibronic interactions that determine the nature of the excitonic states on the emitter molecules. Designing novel phosphorescent emitters for improved exciton management in OLEDs, i.e. for more favorable exciton transfer, will thus require better understanding and tuning of the structural motifs that affect these interactions.

Appendix

A.1 Calculation of vibronic couplings

The normal mode displacement vector in mass-weighted coordinates of the donor molecules ($\mathbf{K}$) is obtained from the Hessian ($\mathbf{H}$) and the energy gradient ($\bar{\mathbf{g}}$), as calculated in the spin-restricted DFT triplet geometry, as follows

$$\mathbf{K} = -\mathbf{H}^{-1}\bar{\mathbf{g}}. \tag{5.22}$$

For the acceptor molecules, the displacement vector $\mathbf{K}^{(0)}$ of the pure singlet and triplet states (without inclusion of spin-orbit coupling) is obtained using TD-DFT as implemented in the ORCA package, which uses the augmented Hessian approach [7]. This approach is found to be more stable for the acceptor excited states than the quasi-Newton method used for the donor molecules. The effect of spin-orbit coupling in the normal mode components K_{n_i} of the displacement vector is included by

$$K_{n_i} = \sum_m c_i^m K_{n_m}^{(0)}, \tag{5.23}$$

where c_i^m are the expansion coefficients of excited state i with spin-orbit coupling in the basis of excited states m without spin-orbit coupling.

A.2 Donor and acceptor spectra

Figure 5.5 shows the normalized squared transition dipole moment spectra of the dye molecules included in this chapter, acting as donor or acceptor.

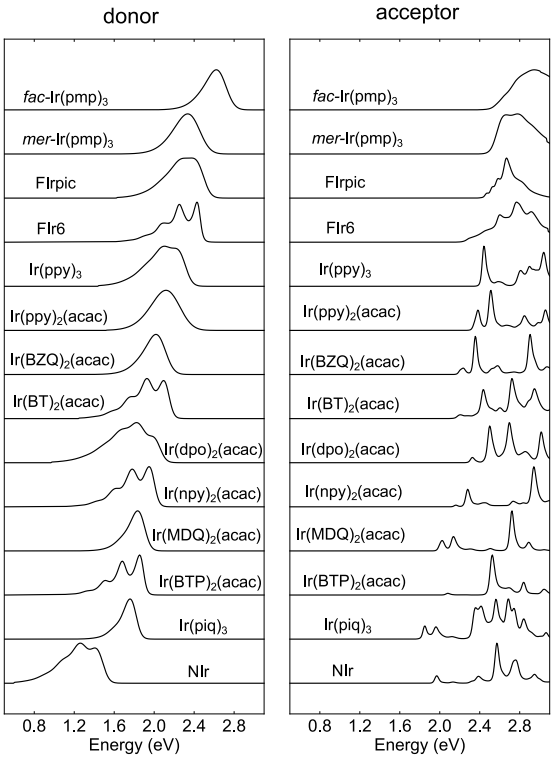

Figure 5.5: Normalized squared transition dipole moment spectra of the dyes, acting as donor (left) and acceptor (right).

A.3 Numerical and graphical Förster radii overview

Table 5.2 contains the calculated Förster radii for donor-acceptor transfer, for all 84 combinations of dyes for which this transfer is possible. The results are graphically shown in Fig. 5.4 in the main text. Figure 5.6 shows the Förster radii of the 84 combinations, plotted separately per dye that can act as donor.

Table 5.2: Förster radii for transfer between dyes, acting as donor (rows) and acceptor (columns). No energetic disorder is assumed and $\kappa_{ij}^2 = \langle\kappa\rangle^2 = 0.67$. The values are displayed graphically in Fig. 5.4 in the main text.

R_F[nm]	*fac*-Ir(pmp)$_3$	*mer*-Ir(pmp)$_3$	FIrpic	FIr6	Ir(ppy)$_3$	Ir(ppy)$_2$acac	Ir(BZQ)$_2$acac	Ir(BT)$_2$acac	Ir(dpo)$_2$acac	Ir(npy)$_2$acac	Ir(MDQ)$_2$acac	Ir(BTP)$_2$acac	Ir(piq)$_3$	NIr
fac-Ir(pmp)$_3$	2.139	2.185	2.327	1.785	2.335	2.406	2.257	2.604	2.942	2.122	2.536	2.716	3.238	3.824
mer-Ir(pmp)$_3$	-	1.334	1.540	1.470	2.308	2.305	2.513	2.396	2.402	2.414	2.363	2.167	3.041	3.096
FIrpic	-	-	1.397	1.409	2.238	2.209	2.449	2.333	2.271	2.367	2.467	2.010	2.978	3.002
FIr6	-	-	-	1.467	2.448	2.264	2.393	2.448	2.463	2.426	2.426	2.132	3.009	2.989
Ir(ppy)$_3$	-	-	-	-	1.271	1.582	2.120	1.904	1.671	2.228	2.666	1.644	2.654	2.797
Ir(ppy)$_2$acac	-	-	-	-	-	1.606	2.057	1.883	1.653	2.114	2.651	1.667	2.611	2.774
Ir(BZQ)$_2$acac	-	-	-	-	-	-	1.376	1.399	0.804	1.473	2.729	1.689	2.799	3.028
Ir(BT)$_2$acac	-	-	-	-	-	-	-	1.361	0.672	1.426	2.627	1.653	2.733	2.881

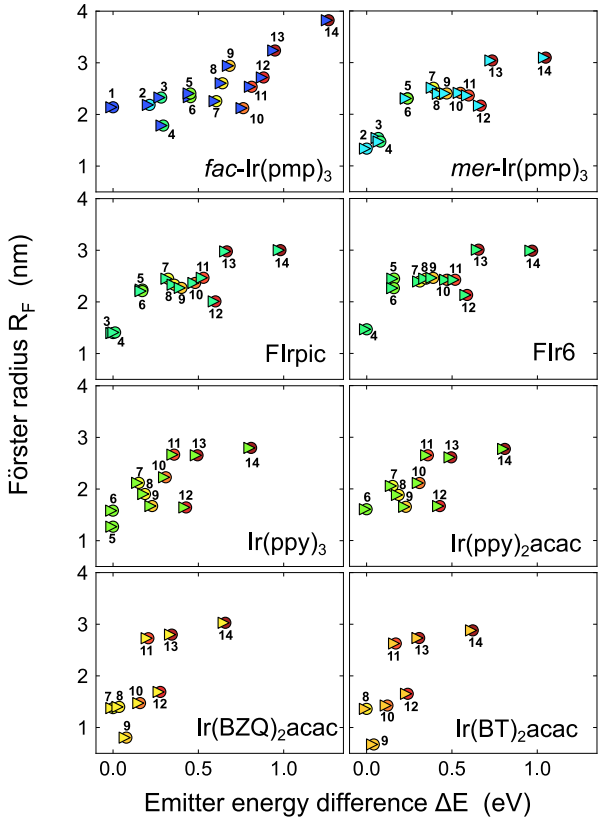

Figure 5.6: Overview of the calculated Förster radius versus donor-acceptor energy difference for the 84 dye combinations, plotted separately for the different dyes that can act as donor. Each point in the graph represents a transfer process from a dye acting as donor (triangle) to a dye acting as acceptor (circle), with emission colours as indicated.

A.4 The effect of energetic disorder

Figure 5.7 shows how the Förster radii are influenced by the energetic disorder. Here, the Förster radii were calculated from the averaged transfer rate for a set of 100 donor-acceptor combinations with energies of donor and acceptor drawn from a Gaussian distribution with disorder parameter $\sigma = 0$ eV (redrawn from Fig. 5.4), $\sigma = 0.05$ eV and $\sigma = 0.10$ eV. With increasing disorder the scatter in the Förster radii tends to decrease. For isoenergetic transfer ($\Delta E \approx 0$) the Förster radius is enhanced. This can be explained by the fact that the Gaussian distribution broadens the spectra and increases spectral overlaps, leading to larger Förster radii. In realistic systems the

energetic disorder is expected to be around 0.05 eV [52]. We see that the effect of the disorder is then weak for a single transfer step.

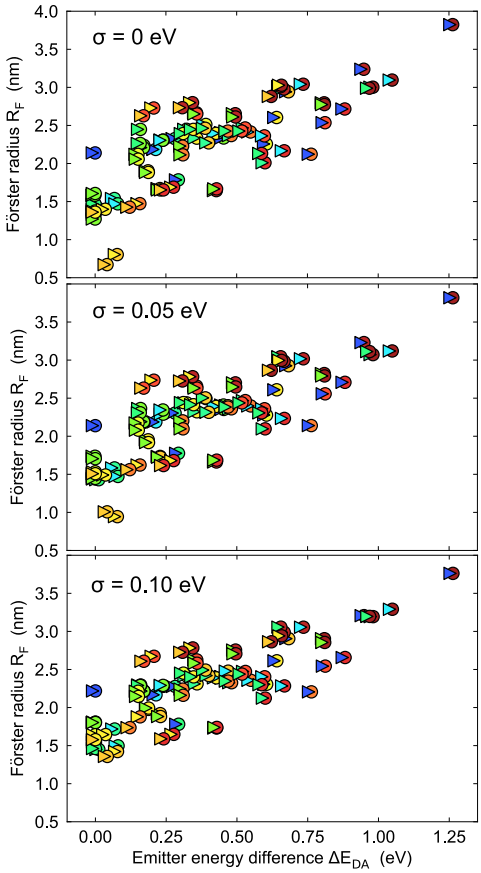

Figure 5.7: Förster radii versus donor-acceptor energy difference, for three values of the width (standard deviation) of a Gaussian distribution of triplet state energies $\sigma = 0$ eV (redrawn from Fig. 5.4), $\sigma = 0.05$ eV and $\sigma = 0.10$ eV. Each point in the graph represents a donor-acceptor pair, where the triangle has the donor emission color and the circle the acceptor emission color.

Bibliography

[1] M. A. Baldo, C. Adachi, and S. R. Forrest. Transient analysis of organic electrophosphorescence. II. Transient analysis of triplet-triplet annihilation. *Phys. Rev. B*, 62(16):10967–10977, 2000. ISSN 01631829. doi: 10.1103/PhysRevB.62.10967.

[2] J. L. Brédas, D. Beljonne, V. Coropceanu, and J. Cornil. Charge-transfer and energy-transfer processes in π-conjugated oligomers and polymers: A molecular picture. *Chem. Rev.*, 104(11):4971–5003, 2004. ISSN 00092665. doi: 10.1021/cr040084k.

[3] Y. L. Chang, D. P. Puzzo, Z. Wang, M. G. Helander, J. Qiu, J. Castrucci, and Z. H. Lu. Improving the efficiency of red phosphorescent organic light emitting diodes by exciton management. *Phys. Status Solidi C*, 9(12):2537–2540, 2012. ISSN 18626351. doi: 10.1002/pssc.201200294.

[4] Y. L. Chang, Y. Song, Z. Wang, M. G. Helander, J. Qiu, L. Chai, Z. Liu, G. D. Scholes, and Z. Lu. Highly efficient warm white organic light-emitting diodes by triplet exciton conversion. *Adv. Funct. Mater.*, 23(6):705–712, 2013. ISSN 1616301X. doi: 10.1002/adfm.201201858.

[5] R. Coehoorn, H. Van Eersel, P. A. Bobbert, and R. A. Janssen. Kinetic Monte Carlo Study of the Sensitivity of OLED Efficiency and Lifetime to Materials Parameters. *Adv. Funct. Mater.*, 25(13):2024–2037, 2015. ISSN 16163028. doi: 10.1002/adfm.201402532.

[6] B. W. D'Andrade, R. J. Holmes, and S. R. Forrest. Efficient Organic Electrophosphorescent White-Light-Emitting Device with a Triple Doped Emissive Layer. *Adv. Mater.*, 16(7):624–628, 2004. ISSN 0935-9648. doi: 10.1002/adma.200306670.

[7] B. De Souza, F. Neese, and R. Izsák. On the theoretical prediction of fluorescence rates from first principles using the path integral approach. *J. Chem. Phys.*, 148 (3), 2018. ISSN 00219606.

[8] X. De Vries, P. Friederich, W. Wenzel, R. Coehoorn, and P. A. Bobbert. Full quantum treatment of charge dynamics in amorphous molecular semiconductors. *Phys. Rev. B*, 97(7):075203, 2018. ISSN 24699969. doi: 10.1103/PhysRevB.97.075203.

[9] C. Diez, T. C. Reusch, S. Seidel, and W. Brütting. Investigation of energy transfer mechanisms between two adjacent phosphorescent emission layers. *J. Appl. Phys.*, 111(11):113102, 2012. ISSN 00218979.

[10] F. Dumur, M. Lepeltier, H. Z. Siboni, D. Gigmes, and H. Aziz. Highly efficient organic light-emitting devices prepared with a phosphorescent heteroleptic iridium (III) complex containing 7,8-benzoquinoline as the cyclometalated ligand. *Adv. Opt. Mater.*, 2(3):262–266, 2014. ISSN 21951071. doi: 10.1002/adom.201300437.

[11] N. C. Erickson and R. J. Holmes. Engineering Efficiency Roll-Off in Organic Light-Emitting Devices. *Adv. Funct. Mater.*, 24(38):6074–6080, 2014. ISSN 16163028. doi: 10.1002/adfm.201401009.

[12] T. Förster. Zwischenmolekulare Energiewanderung und Fluoreszenz. *Ann. der Phys.*, 437:55–75, 1948.

[13] T. Furukawa, H. Nakanotani, M. Inoue, and C. Adachi. Dual enhancement of electroluminescence efficiency and operational stability by rapid upconversion of triplet excitons in OLEDs. *Sci. Rep.*, 5:8429, 2015. ISSN 20452322. doi: 10.1038/srep08429.

[14] P. Heimel, A. Mondal, F. May, W. Kowalsky, C. Lennartz, D. Andrienko, and R. Lovrincic. Unicolored phosphor-sensitized fluorescence for efficient and stable blue OLEDs. *Nat. Commun.*, 9(1):1–8, 2018. ISSN 20411723. doi: 10.1038/s41467-018-07432-2.

[15] K. W. Hershey and R. J. Holmes. Unified analysis of transient and steady-state electrophosphorescence using exciton and polaron dynamics modeling. *J. Appl. Phys.*, 120(19), 2016. ISSN 10897550.

[16] R. J. Holmes, S. R. Forrest, Y.-J. Tung, R. C. Kwong, J. J. Brown, S. Garon, and M. E. Thompson. Blue organic electrophosphorescence using exothermic host–guest energy transfer. *Appl. Phys. Lett.*, 82(15):2422–2424, 2003. ISSN 0003-6951. doi: 10.1063/1.1568146. URL `http://aip.scitation.org/doi/10.1063/1.1568146`.

[17] J. H. Jang, H. U. Kim, S. B. Lee, J. Lee, and D. H. Hwang. Blue-green phosphorescent imidazole-based iridium(III) complex with a broad full width at half maximum for solution-processed organic light-emitting diodes. *Synth. Met.*, 203:180–186, 2015. ISSN 03796779. doi: 10.1016/j.synthmet.2015.02.029. URL `http://dx.doi.org/10.1016/j.synthmet.2015.02.029`.

[18] Y. Kawamura, J. Brooks, J. J. Brown, H. Sasabe, and C. Adachi. Intermolecular interaction and a concentration-Quenching mechanism of phosphorescent Ir(III) complexes in a solid film. *Phys. Rev. Lett.*, 96(1):11–14, 2006. ISSN 10797114. doi: 10.1103/PhysRevLett.96.017404.

[19] J. Kido, M. Kimura, and K. Nagai. Multilayer white light-emitting organic electroluminescent device. *Science.*, 267(5202):1332–1334, 1995. ISSN 00368075. doi: 10.1126/science.267.5202.1332.

[20] Y. H. Kim, K. Wai Cheah, and W. Young Kim. High efficient white organic light-emitting diodes with single emissive layer using phosphorescent red, green, and blue dopants. *Appl. Phys. Lett.*, 103(5), 2013. ISSN 00036951.

[21] S. Lamansky, P. Djurovich, D. Murphy, F. Abdel-Razzaq, H. E. Lee, C. Adachi, P. E. Burrows, S. R. Forrest, and M. E. Thompson. Highly phosphorescent bis-cyclometalated iridium complexes: Synthesis, photophysical characterization, and use in organic light emitting diodes. *J. Am. Chem. Soc.*, 123(18):4304–4312, 2001. ISSN 00027863. doi: 10.1021/ja003693s.

[22] A. D. Laurent and D. Jacquemin. TD-DFT benchmarks: A review. *Int. J. Quantum Chem.*, 113(17):2019–2039, 2013. ISSN 00207608. doi: 10.1002/qua.24438.

[23] J. Lee, H. F. Chen, T. Batagoda, C. Coburn, P. I. Djurovich, M. E. Thompson, and S. R. Forrest. Deep blue phosphorescent organic light-emitting diodes with very high brightness and efficiency. *Nat. Mater.*, 15(1):92–98, 2016. ISSN 14764660. doi: 10.1038/nmat4446.

[24] E. Lerner, T. Cordes, A. Ingargiola, Y. Alhadid, S. Y. Chung, X. Michalet, and S. Weiss. Toward dynamic structural biology: Two decades of single-molecule förster resonance energy transfer. *Science.*, 359(6373):288, 2018. ISSN 10959203.

[25] A. Ligthart. Unpublished work.

[26] A. Ligthart, X. de Vries, L. Zhang, M. C. Pols, P. A. Bobbert, H. van Eersel, and R. Coehoorn. Effect of Triplet Confinement on Triplet–Triplet Annihilation in Organic Phosphorescent Host–Guest Systems. *Adv. Funct. Mater.*, 28:1804618, 2018. ISSN 16163028. doi: 10.1002/adfm.201804618.

[27] F. Lindla, M. Boesing, P. Van Gemmern, D. Bertram, D. Keiper, M. Heuken, H. Kalisch, and R. H. Jansen. Employing exciton transfer molecules to increase the lifetime of phosphorescent red organic light emitting diodes. *Appl. Phys. Lett.*, 98(17):173304, 2011. ISSN 00036951. doi: 10.1063/1.3584033.

[28] Z. T. Liu, C. Y. Kwong, C. H. Cheung, A. B. Djurišić, Y. Chan, and P. C. Chui. The characterization of the optical functions of BCP and CBP thin films by spectroscopic ellipsometry. *Synth. Met.*, 150(2):159–163, 2005. ISSN 03796779. doi: 10.1016/j.synthmet.2005.02.001.

[29] M. Mesta, M. Carvelli, R. J. de Vries, H. van Eersel, J. J. M. van der Holst, M. Schober, M. Furno, B. Lüssem, K. Leo, P. Loebl, R. Coehoorn, and P. A. Bobbert. Molecular-scale simulation of electroluminescence in a multilayer white organic light-emitting diode. *Nat. Mater.*, 12:652, 2013.

[30] C. Murawski, K. Leo, and M. C. Gather. Efficiency roll-off in organic light-emitting diodes. *Adv. Mater.*, 25(47):6801–6827, 2013. ISSN 09359648. doi: 10.1002/adma.201301603.

[31] N. Nabatova-Gabain, Y. Wasai, and T. Tsuboi. Spectroscopic ellipsometry study of Ir(ppy)3organic light emitting diode. *Curr. Appl. Phys.*, 6(5):833–838, 2006. ISSN 15671739. doi: 10.1016/j.cap.2005.01.034.

[32] G. Nan, X. Yang, L. Wang, Z. Shuai, and Y. Zhao. Nuclear tunneling effects of charge transport in rubrene, tetracene, and pentacene. *Phys. Rev. B*, 79(11): 115203, 2009. ISSN 10980121. doi: 10.1103/PhysRevB.79.115203.

[33] F. Neese. Efficient and accurate approximations to the molecular spin-orbit coupling operator and their use in molecular g-tensor calculations. *J. Chem. Phys.*, 122(3):034107, 2005. ISSN 00219606.

[34] F. Neese. Software update: the ORCA program system, version 4.0. *Wiley Interdiscip. Rev. Comput. Mol. Sci.*, 8(1):4–9, 2018. ISSN 17590884. doi: 10.1002/wcms.1327.

[35] D. A. Pantazis, X.-Y. Chen, C. R. Landis, and F. Neese. All-Electron Scalar Relativistic Basis Sets for Third-Row Transition Metal Atoms. *J. Chem. Theory Comput.*, 4(6):908–919, 2008. ISSN 1549-9618. doi: 10.1021/ct800047tPM-26621232.

[36] S. Reineke and M. A. Baldo. Recent progress in the understanding of exciton dynamics within phosphorescent OLEDs. *Phys. Status Solidi A*, 209(12):2341–2353, 2012. ISSN 18626300. doi: 10.1002/pssa.201228292.

[37] S. Reineke, K. Walzer, and K. Leo. Triplet-exciton quenching in organic phosphorescent light-emitting diodes with Ir-based emitters. *Phys. Rev. B*, 75(12): 125328, 2007. ISSN 10980121. doi: 10.1103/PhysRevB.75.125328.

[38] T. C. Rosenow, M. Furno, S. Reineke, S. Olthof, B. Lüssem, and K. Leo. Highly efficient white organic light-emitting diodes based on fluorescent blue emitters. *J. Appl. Phys.*, 108(11):113113, 2010. ISSN 00218979. doi: 10.1063/1.3516481.

[39] C. E. Rowland, J. B. Delehanty, C. L. Dwyer, and I. L. Medintz. Growing applications for bioassembled Förster resonance energy transfer cascades. *Mater. Today*, 20(3):131–141, 2017. ISSN 18734103. doi: 10.1016/j.mattod.2016.09.013. URL `http://dx.doi.org/10.1016/j.mattod.2016.09.013`.

[40] A. Salehi, Y. Chen, X. Fu, C. Peng, and F. So. Manipulating Refractive Index in Organic Light Emitting Diodes. *ACS Appl. Mater. Interfaces*, 10:9595, 2018. ISSN 1944-8244. doi: 10.1021/acsami.7b18514. URL `http://pubs.acs.org/doi/10.1021/acsami.7b18514`.

[41] G. D. Scholes. Long range resonance energy transfer in molecular systems. *Annu. Rev. Phys. Chem.*, 54(1):57–87, 2003. ISSN 0066-426X. URL `http://www.annualreviews.org/doi/10.1146/annurev.physchem.54.011002.103746`.

[42] G. D. Scholes and K. P. Ghiggino. Rate expressions for excitation transfer I. Radiationless transition theory perspective. *J. Chem. Phys.*, 101(2):1251–1261, 1994. ISSN 00219606. doi: 10.1063/1.467817.

[43] G. Schwartz, S. Reineke, T. C. Rosenow, K. Walzer, and K. Leo. Triplet harvesting in hybrid white organic light-emitting diodes. *Adv. Funct. Mater.*, 19(9): 1319–1333, 2009. ISSN 1616301X. doi: 10.1002/adfm.200801503.

[44] K. S. Son, M. Yahiro, T. Imai, H. Yoshizaki, J. Nishide, H. Sasabe, and C. Adachi. Roll-off characteristics of electroluminescence efficiency of organic blue electrophosphorescence diodes. *Jpn. J. Appl. Phys.*, 47(9 PART 1):7363–7365, 2008. ISSN 00214922. doi: 10.1143/JJAP.47.7363.

[45] D. Song, S. Zhao, Y. Luo, and H. Aziz. Causes of efficiency roll-off in phosphorescent organic light emitting devices: Triplet-triplet annihilation versus triplet-polaron quenching. *Appl. Phys. Lett.*, 97(24):1–4, 2010. ISSN 00036951. doi: 10.1063/1.3527085.

[46] W. Staroske, M. Pfeiffer, K. Leo, and M. Hoffmann. Single-step triplet-triplet annihilation: An intrinsic limit for the high brightness efficiency of phosphorescent organic light emitting diodes. *Phys. Rev. Lett.*, 98(19):197402, 2007. ISSN 00319007. doi: 10.1103/PhysRevLett.98.197402.

[47] V. Stehr, R. F. Fink, M. Tafipolski, C. Deibel, and B. Engels. Comparison of different rate constant expressions for the prediction of charge and energy transport in oligoacenes. *Wiley Interdiscip. Rev. Comput. Mol. Sci.*, 6(6):694–720, 2016. ISSN 17590884. doi: 10.1002/wcms.1273.

[48] F. S. Steinbacher, R. Krause, A. Hunze, and A. Winnacker. Triplet exciton transfer mechanism between phosphorescent organic dye molecules. *Phys. Status Solidi A*, 209(2):340–346, 2012. ISSN 18626300. doi: 10.1002/pssa.201127451.

[49] S. J. Strickler and R. A. Berg. Relationship between absorption intensity and fluorescence lifetime of molecules. *J. Chem. Phys.*, 37(4):814–822, 1962. ISSN 00219606.

[50] Y. Sun, N. C. Giebink, H. Kanno, B. Ma, M. E. Thompson, and S. R. Forrest. Management of singlet and triplet excitons for efficient white organic light-emitting devices. *Nature*, 440:908, 2006.

[51] M. Thompson. Mark Thompson. *MRS Bull.*, 32(September 2007):2011, 2011.

[52] X. D. Vries, P. Friederich, R. Coehoorn, and P. A. Bobbert. Triplet exciton diffusion in metal-organic phosphorescent host-guest systems from first principles. *Phys. Rev. B*, 99(20):205201, 2019. ISSN 0031-899X. doi: 10.1103/PhysRevB.99.205201. URL `https://doi.org/10.1103/PhysRevB.99.205201`.

[53] Q. Wang, J. Ding, D. Ma, Y. Cheng, L. Wang, and F. Wang. Manipulating Charges and Excitons within a Single-Host System to Accomplish Efficiency/CRI/Color-Stability Trade-off for High-Performance OWLEDs. *Adv. Mater.*, 21(23):2397–2401, 2009. ISSN 09359648. doi: 10.1002/adma.200803312.

[54] J. Wehner and B. Baumeier. Intermolecular Singlet and Triplet Exciton Transfer Integrals from Many-Body Green's Functions Theory. *J. Chem. Theory Comput.*, 13(4):1584–1594, 2017. ISSN 15499626. doi: 10.1021/acs.jctc.6b00935.

[55] C. Weichsel, S. Reineke, M. Furno, B. Lssem, and K. Leo. Organic light-emitting diodes for lighting: High color quality by controlling energy transfer processes in host-guest-systems. *J. Appl. Phys.*, 111(3), 2012. ISSN 00218979.

[56] E. L. Williams, J. Li, and G. E. Jabbour. Organic light-emitting diodes having exclusive near-infrared electrophosphorescence. *Appl. Phys. Lett.*, 89(8):90–93, 2006. ISSN 00036951. doi: 10.1063/1.2335275.

[57] T. Yonehara, K. Goushi, T. Sawabe, I. Takasu, and C. Adachi. Comparison of transient state and steady state exciton-exciton annihilation rates based on Förster-type energy transfer. *Jpn. J. Appl. Phys.*, 54(7), 2015. ISSN 13474065.

[58] Z. Q. You and C. P. Hsu. Theory and calculation for the electronic coupling in excitation energy transfer. *Int. J. Quantum Chem.*, 114(2):102–115, 2014. ISSN 00207608. doi: 10.1002/qua.24528.

[59] L. Zhang, H. van Eersel, P. A. Bobbert, and R. Coehoorn. Analysis of the phosphorescent dye concentration dependence of triplet-triplet annihilation in organic host-guest systems. *Chem. Phys. Lett.*, 662:221–227, 2016. ISSN 00092614. doi: 10.1016/j.cplett.2016.07.048. URL `http://dx.doi.org/10.1016/j.cplett.2016.07.048`.

[60] Y. Zhang and S. R. Forrest. Triplet diffusion leads to triplet-triplet annihilation in organic phosphorescent emitters. *Chem. Phys. Lett.*, 590:106–110, 2013. ISSN 00092614. doi: 10.1016/j.cplett.2013.10.048. URL `http://dx.doi.org/10.1016/j.cplett.2013.10.048`.

Chapter 6

Conclusions and Outlook

In the last three chapters we have presented and discussed the results of the application of a Fermi's Golden Rule (FGR) rate, which quantum mechanically includes all the intramolecular vibrations, to the charge and exciton transport in disordered organic semiconductors. In this chapter we will briefly summarize the main conclusions of the three previous chapters. Then, we will give an outlook on the further application of the FGR rate on additional processes of common interest to OLED device physics. We look at the charge transfer from host to guest, which plays a role in the formation of excitons in the OLED Emissive Layer (EML). Then we briefly discuss exciton polaron quenching (EPQ), which is one of the important loss mechanisms in OLEDs.

6.1 Main conclusions

In **Chapter 3** we have developed a charge transport model starting from a fully quantum mechanical Fermi's Golden Rule (FGR) rate and including all the energetic, spatial and orientational disorder. The FGR rate includes the electron and hole coupling to all intramolecular vibrations. The rate as a function of site energy difference (ΔE) shows significant deviations from both the Marcus and Miller-Abrahams rates. Further in the chapter we look at the influence of the different rate theories on the charge mobilities and charge carrier relaxation. Three common host materials used in modern day OLEDs are studied. We find very similar charge mobility results for the FGR, Marcus and Miller-Abrahams rates. This can be attributed to the energetic disorder, which washes out the strong variations in the ΔE-dependence of the FGR rate. However, at low temperatures the charge carrier mobility calculated with Marcus theory drops significantly below the mobility calculated with the FGR rate. The mobility as calculated with the Miller-Abrahams theory then coincides quite well with the FGR rate mobility.

In **Chapter 4** we apply the previously developed FGR rate expression to study exciton diffusion in common phosphorescent host guest systems. We replace the charge transfer integrals with exciton transfer integrals containing both short-range Dexter and long-range Förster contributions. Due to the strong vibronic coupling of the triplet transfer, the Marcus theory dramatically underestimates the transfer rates in these systems. We find that at guest concentrations realistic for OLED devices the diffusion lengths are on the order of 2 nm and the Förster transfer integrals dominate the transfer process. However, at systems above 30 mol% guest concentration the Dexter process becomes dominant and diffusion lengths can increase up to 30 nm for neat film systems.

In **Chapter 5** we calculate rates for exothermic energy transfer between phosphorescent emitter molecules. Such transfer is relevant for the development of novel device architectures for white OLEDs. We study 14 different emitter molecules and calculate Förster radii for over 80 different donor acceptor combinations. It is found that the exothermic transfer, for example from green to red emitters, is enhanced with respect to the isoenergetic transfer as studied in Chapter 4. The enhancement is due to two reasons. Firstly, the excess energy in the exothermic transfer compensates for the Stokes shifted energy levels of the donor and acceptor molecules. Secondly, at large excess energies, above 0.2 eV, energetically higher excited of the acceptor molecule start enhancing the transfer rate. These higher excited states are found to have strong transition dipole moments and can therefore quite significantly enhance the transfer. We find that the Förster radii vary from around 1 nm for isoenergetic transfer to almost 4 nm for the most extreme case of exothermic transfer from a blue donor to a near infrared acceptor molecule.

6.2 Outlook

In the last 3 chapters we have presented 3 different contributions to the field of charge and exciton transport modelling. The modelling of charge transport has reached the point where the models are predictive on a device scale starting from the molecular structure [9, 10, 6, 5, 7]. In Chapter 3 we found that the full FGR rate does not improve the charge mobility prediction of the charge transport models with respect to the use of Marcus and Miller-Abrahams rates, at least at room temperature. One area where the FGR rate might offer an important improvement is at large exothermic charge transfer. Such charge transfer occurs mostly in the EML of the OLEDs. There, the energy difference between the HOMO and LUMO of the host and guest molecules can be quite significant, meaning that the transfer from host to guest occurs with a lot of excess energy. In that case, the Marcus rate will have entered the *inverted* regime, where the transfer rate is strongly underestimated with respect to the correct FGR rate. This shortcoming of the Marcus rate expression was already remarked by May [11]. In the next subsection we will further discuss this effect.

For exciton transport the comparison with experimental results is less straightforward since not a lot of experimental work has been done. As we have shown in Chapters 4 and 5, the Förster radii calculated using first-principles methods are comparable to experimental values from the few studies that are available, which is encouraging. Another perspective on exciton transport is that often we are not interested in the exciton transport itself, but rather the loss processes that are induced by the transport like exciton-exciton annihilation (EEA) and exciton polaron quenching (EPQ). Therefore, it is vital to first fully understand these processes. Some experimental work on EEA and EPQ in OLED relevant materials and systems is being done [2, 12, 18, 15, 17, 8], but still many questions remain. Kinetic Monte Carlo models have been developed in the last years to study the EEA and EPQ on the device scale [14, 4, 16]. Such models can only draw qualitative conclusions because the rates for the different EEA and EPQ processes are unknown. The extension of the methods developed in this thesis to EEA and EPQ rates on a molecular level would therefore be of enormous value. We will discuss some ideas on how to calculate the EPQ and EEA rates for the molecules studied in this work.

6.2.1 Host-guest charge transfer and exciton formation

There are two ways in which excitons are formed in the EML. Firstly, excitons can form on the host in the EML, and then transfer to the guest in the EML. For such a transfer to occur it is important that the exciton level of the guest is below the exciton level of the host, so that efficient transfer occurs. Another possibility is exciton formation on the guest. For this, either the HOMO and/or the LUMO has to be chosen in such a way that efficient charge trapping on the guest occurs. There are also other possibilities, like excimer formation between the EML host and the HTL

or ETL followed by transfer. We will not discuss those possibilities here and focus on the exciton formation on the host and exciton formation on the guest.

In many studies it is not at all clear whether exciton formation occurs on the host or on the guest or on both. Endothermic exciton EMLs, with a guest triplet energy level higher than the host triplet energy, have been studied by Adachi *et al* [1] and found to be efficient. In that work the FIrpic emitter ($E_T = 2.62$) was used in a CBP ($E_T = 2.56$) host yielding efficient emission from the FIrpic molecule. In the paper it is argued that the emission occurs from the exciton formation on the host followed by endothermic transfer to the FIrpic emitter. This supported by photoluminescence (PL) experiments. However, in PL experiments only the singlet population of the CBP host is excited, while the CBP triplet state is endothermic with respect to the FIrpic triplet state, the CBP singlet state is not. Therefore, we can not conclude from the PL experiments that excitation transfer also occurs in the electrically driven device where most of the excitations will be triplets. Another possible explanation for the FIrpic triplet population in the device is that the LUMO of FIrpic is just below the LUMO of CBP, which means that electrons can effectively be trapped by the FIrpic molecule. The holes will then be attracted by the negative charge and exciton formation on the FIrpic molecule is possible.

Another work which shows anomalous behaviour with respect to exciton formation is the study by Chang *et al.* [3]. Here, two devices with different emitter molecules were studied. The first device employed the green $Ir(ppy)_2(acac)$ molecule in CBP and the second device employed the red $Ir(MDQ)_2(acac)$ molecule in CBP. The HOMO and LUMO energy levels of CBP, $Ir(ppy)_2(acac)$ and $Ir(MDQ)_2(acac)$ as reported in the study by Chang are shown in Fig. 6.1. In the study it was found that the turn on voltage for the green emitter device was lower than the turn on voltage for the red emitter device. This suggests that in the green device the emitter plays a role in the conduction and trapping of carriers, which allows excitons to directly form on the emitter, while this is not the case for the device with the red emitter.

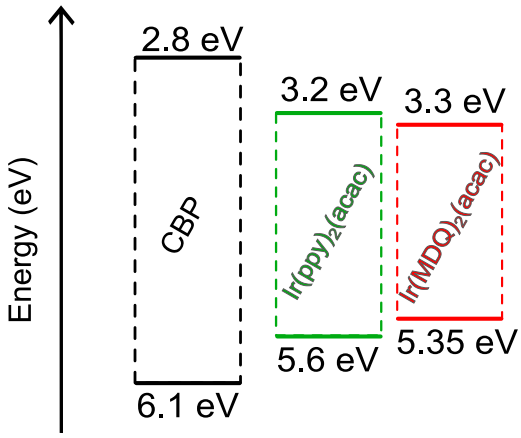

Figure 6.1: HOMO and LUMO energy levels of the CBP, $Ir(ppy)_2(acac)$ and $Ir(MDQ)_2(acac)$ as reported in the study by Chang *et al.* [3]

These studies show that: i) The exciton formation process is not only dependent on the exciton confinement but also on the HOMO and LUMO levels of the host and guest molecules, ii) Even when exciton, HOMO and LUMO levels of the guest molecules are all well confined, the exciton formation process is still dependent on other molecular properties as shown by Chang *et al.* This observation might be explained by the role that the vibrons play in the transfer process at large excess energy.

Within Marcus theory starting from $\Delta E = 0$ The rate will increase with more excess energy. However, when the energy difference becomes to large, the Marcus rate enters the inverted regime in which the rate decreases again. Such behavior is not unique for the Marcus theory, but also applies to the FGR expression developed in the work as can be seen in Chapters 3 and 4.

When exciton formation occurs on the guest molecules, the first step of the formation process is the hole (+) or electron (−) transfer from the host molecule (H) to the guest (G) molecule

$$\begin{aligned} \mathrm{H}^{+} + \mathrm{G}^{\mathrm{n}} &\rightarrow \mathrm{H}^{\mathrm{n}} + \mathrm{G}^{+} \\ \mathrm{H}^{-} + \mathrm{G}^{\mathrm{n}} &\rightarrow \mathrm{H}^{\mathrm{n}} + \mathrm{G}^{-}. \end{aligned} \tag{6.1}$$

If the charge transfer rate between the CBP and the red $Ir(MDQ)_2(acac)$ molecule is indeed much smaller than the transfer rate from CBP to $Ir(ppy)_2(acac)$, that can explain why the green emitter does seem to conduct in the host-guest system while the red emitter does not. In order to quantify this statement, we calculated the CBP

to $Ir(ppy)_2(acac)$ and CBP to $Ir(MDQ)_2(acac)$ charge transfer rates. The curve for the transfer rate as a function of ΔE is shown in Fig. 6.2. If we take the HOMO and LUMO values of CBP, $Ir(ppy)_2(acac)$ and $Ir(MDQ)_2(acac)$ as used in the work by Chang *et al.* we find the rates as indicated by the black arrows pointing to the dots in Fig. 6.2. The values at the dots clearly show that the transfer rate is much smaller than the typical transfer rate for CBP to CBP transfer ($\sim 10^{11}$ s^{-1}). The hole transfer rate for CBP to $Ir(MDQ)_2(acac)$ is even 1.5 orders of magnitude smaller than for CBP to $Ir(ppy)_2(acac)$. Such a small transfer rate might explain the lack of conduction of the guests in the CBP:$Ir(MDQ)_2(acac)$ host-guest systems studied by Chang *et al.*

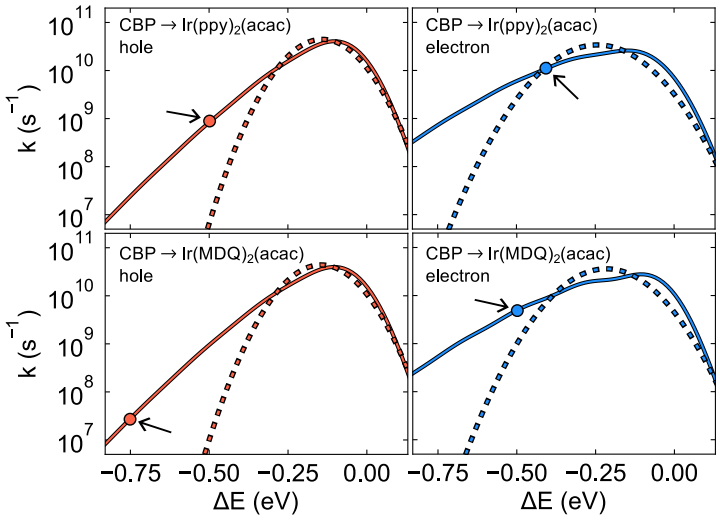

Figure 6.2: Hole (left) and electron (right) transfer rates for the CBP to $Ir(ppy)_2(acac)$ transfer (top) and the CBP to $Ir(MDQ)_2(acac)$ transfer (bottom) as a function of ΔE. The transfer integrals for hole and electron transfer are chosen to be $J = 1$ meV, similar to what was done in Chapter 3. The dots pointed to by black arrows indicate the values at which the transfer occurs according to the HOMO and LUMO values as reported by Chang *et al.*

The inverted regime effect shown in Fig. 6.2 is overestimated by the Marcus rate, while it is underestimated by the Miller-Abrahams rate. The effect might be studied by combining experimental work on onset voltages in OLEDs for different emitters with predictive kinetic Monte Carlo simulations. The inverted regime effect may also influence the charge balance in devices where hole transfer from HTL to EML or electron transfer from ETL to EML is accompanied by large excess energy.

6.2.2 Exciton polaron quenching

1) Device physics

Exciton Polaron Quenching (EPQ) is believed to be the major cause of the roll-off in modern OLEDs. The process is commonly described as follows,

$$\mathrm{P}^- + \mathrm{S}_1 \rightarrow \mathrm{P}^{-^*} + \mathrm{S}_0 \tag{6.2}$$
$$\mathrm{P}^+ + \mathrm{S}_1 \rightarrow \mathrm{P}^{+^*} + \mathrm{S}_0 \tag{6.3}$$

and for triplets,

$$\mathrm{P}^- + \mathrm{T}_1 \rightarrow \mathrm{P}^{-^*} + \mathrm{S}_0 \tag{6.4}$$
$$\mathrm{P}^+ + \mathrm{T}_1 \rightarrow \mathrm{P}^{+^*} + \mathrm{S}_0 \tag{6.5}$$

The polarons (P) on the right hand side are left in an excited state (indicated by the asterisk) and the assumption is that these states are non-emissive and can lead to molecular bond breaking. From this point we can look at two different possible contributions to the polaron quenching process in an OLED. (i) host-host polaron quenching where both the polaron and the exciton are located on the host. In this case the exciton will most likely be a triplet since the singlet states will transfer quite fast to the guest molecules. The polaron quenching process then requires multiple steps and is therefore best desribed by Dexter transfer. (ii) guest-host polaron quenching, here, the exciton is located on the guest molecule and is, in a single step, transfered to the polaron on the host molecule via Förster transfer. The interaction will most likely not be of Dexter type because of the long range character of the Förster interaction and the fact that the exciton is trapped on the guest. (iii) guest-guest polaron quenching, where both exciton and polaron are located on the guest material. The exciton is transfered to the polaron via a single step. This process is perhaps most unlikely because both exciton and polaron are trapped and therefore less likely to meet, however, we can not exclude the process as the Förster radius for such a process could be very large.

In the next section we will shortly discuss the single step polaron quenching process, (ii) and (iii).

2) Exciton polaron quenching rate

Starting from Fermi's Golden Rule we develop a rate expression for the EPQ process. The transfer integral for the process will be calculated from Förster theory so we need to calculate the donor and acceptor squared transition dipole spectra as done in Chapter 5. The EPQ rate will then be given by,

$$k_{\mathrm{EPQ,h}} = \frac{2\pi}{\hbar}\frac{1}{(4\pi\epsilon_0\epsilon_\mathrm{r})^2}\frac{\langle\kappa^2\rangle}{R^6}\int \mu_D^2(E)\mu_{A^+}^2(E)dE, \tag{6.6}$$

for holes and

$$k_{\mathrm{EPQ,e}} = \frac{2\pi}{\hbar} \frac{1}{(4\pi\epsilon_0\epsilon_\mathrm{r})^2} \frac{\langle\kappa^2\rangle}{R^6} \int \mu_D^2(E)\mu_{A^-}^2(E)dE, \tag{6.7}$$

for electrons. The donor spectra (μ_D) for such a transfer are already developed in Chapter 5. For the acceptor spectra (μ_{A^+} and μ_{A^-}) we need to calculate the transition dipole moments and vibronic couplings of molecules in their polaron state. This can be done with TD-DFT calculations on an open-shell reference DFT state. We have performed such calculation for CBP and α-NPD.

The rate for the single step Förster polaron quenching process will be strongly determined by the excited state energies and transition dipole moments of the polaron. A few studies have found that for common OLED materials the hole absorption spectra are more pronounced than the electron absorption spectra. The hole absorption spectra show strong transition from energies of about 1 eV. Such low energies make the transfer from the excited state species strongly exothermic.

To get an idea of the excited state character of charged molecules we calculate the excited states of the charged mCBP molecule. For this calculation, we first relax the geometry of the mCBP molecule in the anion or cation open-shell DFT state. Then we perform TD-DFT calculations on the open-shell DFT reference wavefunction. The results for lowest four hole and electron excitations of the mCBP molecule are displayed in Table 6.1 and Table 6.2. Comparing the two tables, we see that the transition dipole moments of the hole excitations are significantly larger than for the electron excitations. The four lowest hole excitation lie in a window from 1.00 - 1.93 eV, while for the electron excitations there is a huge gap between the first excitation at 0.15 eV and the second excitation at 1.77 eV. From the magnitude of the transition dipole moments and the energetic ordering of the states we can already understand the strong absorption of the cationic species of mCBP with respect to the negligible absorption of the anionic species [13]. The orbital transitions that contribute to the hole excitations are all from low lying occupied molecular orbitals to the HOMO, while the contributions to the electron excitations are all from the LUMO to higher unoccupied orbitals.

If we use this information to describe for example the Förster Triplet-Hole Quenching (THQ) and Triplet-Electron Quenching (TEQ) in typical phosphorescent OLED systems these processes can be viewed as schematically depicted in Fig. 6.3

Table 6.1: Energies, squared transition dipole moments and main orbital transition contribution for hole excitations in the mCBP molecule.

Energy (eV)	μ^2(a.u.^{2})	Orb. trans.
1.00	64.7	HOMO−1 → HOMO
1.69	1.79	HOMO−4 → HOMO
1.70	1.63	HOMO−5 → HOMO
1.93	6.53	HOMO−6 → HOMO

Table 6.2: Energies, squared transition dipole moments and main orbital transition contribution for electron excitations in the mCBP molecule.

Energy (eV)	μ^2(a.u.^{2})	Orb. trans.
0.15	0.28	LUMO → LUMO+1
1.77	1.16	LUMO → LUMO+7
2.07	0.53	LUMO → LUMO+9
2.58	3.82	LUMO → LUMO+11

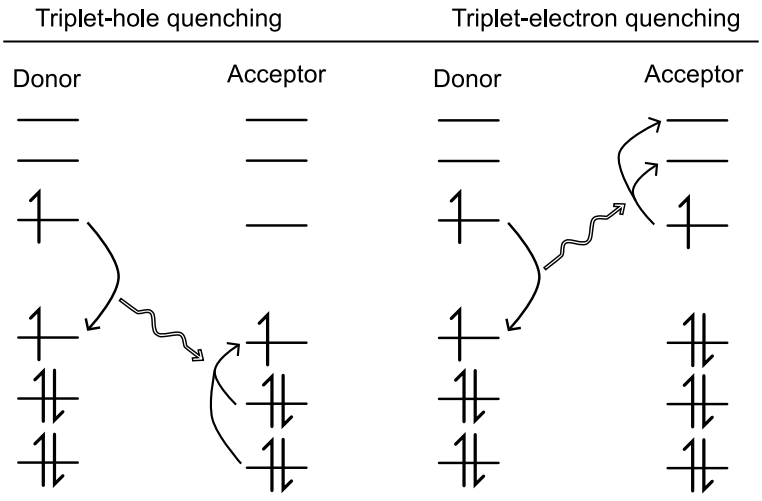

Figure 6.3: Schematic depiction of the Förster mediated THQ and TEQ as expected for the mCBP molecule. All hole excitations involve transitions to the HOMO level of the acceptor, while all electron excitations involve transitions from the LUMO level of the acceptor.

Bibliography

[1] C. Adachi, R. C. Kwong, P. Djurovich, V. Adamovich, M. A. Baldo, M. E. Thompson, and S. R. Forrest. Endothermic energy transfer: A mechanism for generating very efficient high-energy phosphorescent emission in organic materials. *Appl. Phys. Lett.*, 79(13):2082–2084, 2001. ISSN 00036951. doi: 10.1063/1.1400076.

[2] M. A. Baldo, C. Adachi, and S. R. Forrest. Transient analysis of organic electrophosphorescence. II. Transient analysis of triplet-triplet annihilation. *Phys. Rev. B*, 62(16):10967–10977, 2000. ISSN 01631829. doi: 10.1103/PhysRevB.62.10967.

[3] Y. L. Chang, D. P. Puzzo, Z. Wang, M. G. Helander, J. Qiu, J. Castrucci, and Z. H. Lu. Improving the efficiency of red phosphorescent organic light emitting diodes by exciton management. *Phys. Status Solidi Curr. Top. Solid State Phys.*, 9(12):2537–2540, 2012. ISSN 18626351. doi: 10.1002/pssc.201200294.

[4] R. Coehoorn, H. Van Eersel, P. A. Bobbert, and R. A. Janssen. Kinetic Monte Carlo Study of the Sensitivity of OLED Efficiency and Lifetime to Materials Parameters. *Adv. Funct. Mater.*, 25(13):2024–2037, 2015. ISSN 16163028. doi: 10.1002/adfm.201402532.

[5] P. Friederich, V. Meded, A. Poschlad, T. Neumann, V. Rodin, V. Stehr, F. Symalla, D. Danilov, G. Lüdemann, R. F. Fink, I. Kondov, F. von Wrochem, and W. Wenzel. Molecular Origin of the Charge Carrier Mobility in Small Molecule Organic Semiconductors. *Adv. Funct. Mater.*, 26(31):5757–5763, 2016. ISSN 16163028. doi: 10.1002/adfm.201601807.

[6] P. Kordt, J. J. M. van der Holst, M. Al Helwi, W. Kowalsky, F. May, A. Badinski, C. Lennartz, and D. Andrienko. Modeling of Organic Light Emitting Diodes: From Molecular to Device Properties. *Adv. Funct. Mater.*, 25(13):1955–1971, 2015. doi: 10.1002/adfm.201403004. URL `https://onlinelibrary.wiley.com/doi/abs/10.1002/adfm.201403004`.

[7] N. B. Kotadiya, A. Mondal, S. Xiong, P. W. Blom, D. Andrienko, and G. J. A. Wetzelaer. Rigorous Characterization and Predictive Modeling of Hole Transport in Amorphous Organic Semiconductors. *Adv. Electron. Mater.*, 4(12):1–7, 2018. ISSN 2199160X. doi: 10.1002/aelm.201800366.

[8] A. Ligthart, X. de Vries, L. Zhang, M. C. Pols, P. A. Bobbert, H. van Eersel, and R. Coehoorn. Effect of Triplet Confinement on Triplet–Triplet Annihilation in Organic Phosphorescent Host–Guest Systems. *Adv. Funct. Mater.*, 28:1804618, 2018. ISSN 16163028. doi: 10.1002/adfm.201804618.

[9] F. Liu, A. Massé, P. Friederich, F. Symalla, R. Nitsche, W. Wenzel, R. Coehoorn, and P. A. Bobbert. Ab initio modeling of steady-state and time-dependent charge transport in hole-only α -NPD devices. *Appl. Phys. Lett.*, 109(24), 2016. ISSN 00036951. doi: 10.1063/1.4971969.

[10] A. Massé, P. Friederich, F. Symalla, F. Liu, R. Nitsche, R. Coehoorn, W. Wenzel, and P. A. Bobbert. \textit{Ab initio} charge-carrier mobility model for amorphous molecular semiconductors. *Phys. Rev. B*, 93(19):195209, 2016. doi: 10.1103/PhysRevB.93.195209. URL `http://link.aps.org/doi/10.1103/PhysRevB.93.195209`.

[11] F. May. *Charge-transport simulations in organic semiconductors*. Doctoral dissertation, 2012.

[12] S. Reineke, K. Walzer, and K. Leo. Triplet-exciton quenching in organic phosphorescent light-emitting diodes with Ir-based emitters. *Phys. Rev. B*, 75(12): 125328, 2007. ISSN 10980121. doi: 10.1103/PhysRevB.75.125328.

[13] A. S. D. Sandanayaka, K. Yoshida, T. Matsushima, and C. Adachi. Exciton quenching behavior of thermally activated delayed fluorescence molecules by charge carriers. *J. Phys. Chem. C*, 119(14):7631–7636, 2015. ISSN 19327455. doi: 10.1021/acs.jpcc.5b01314.

[14] H. Van Eersel, P. A. Bobbert, R. A. Janssen, and R. Coehoorn. Monte Carlo study of efficiency roll-off of phosphorescent organic light-emitting diodes: Evidence for dominant role of triplet-polaron quenching. *Appl. Phys. Lett.*, 105(14), 2014. ISSN 00036951. doi: 10.1063/1.4897534.

[15] S. Wehrmeister, L. Jäger, T. Wehlus, A. F. Rausch, T. C. Reusch, T. D. Schmidt, and W. Brütting. Combined electrical and optical analysis of the efficiency roll-off in phosphorescent organic light-emitting diodes. *Phys. Rev. Appl.*, 3(2):1–10, 2015. ISSN 23317019. doi: 10.1103/PhysRevApplied.3.024008.

[16] T. Yonehara, K. Goushi, T. Sawabe, I. Takasu, and C. Adachi. Comparison of transient state and steady state exciton-exciton annihilation rates based on Förster-type energy transfer. *Jpn. J. Appl. Phys.*, 54(7), 2015. ISSN 13474065.

[17] L. Zhang, H. van Eersel, P. A. Bobbert, and R. Coehoorn. Analysis of the phosphorescent dye concentration dependence of triplet-triplet annihilation in organic host-guest systems. *Chem. Phys. Lett.*, 662:221–227, 2016. ISSN 00092614. doi: 10.1016/j.cplett.2016.07.048. URL `http://dx.doi.org/10.1016/j.cplett.2016.07.048`.

[18] Y. Zhang and S. R. Forrest. Triplet diffusion leads to triplet-triplet annihilation in organic phosphorescent emitters. *Chem. Phys. Lett.*, 590:106–110, 2013. ISSN 00092614. doi: 10.1016/j.cplett.2013.10.048. URL `http://dx.doi.org/10.1016/j.cplett.2013.10.048`.

List of publications

1. X. de Vries, P. Friederich, W. Wenzel, R. Coehoorn and P.A. Bobbert, *Full quantum treatment of charge dynamics in amorphous molecular semiconductors*, Phys. Rev. B 97, 075203 (2018).

2. X. de Vries, P. Friederich, R. Coehoorn and P. A. Bobbert, *Triplet exciton diffusion in metal-organic phosphorescent host-guest systems from first principles*, Phys. Rev. B 99, 205201 (2019).

3. X. de Vries, R. Coehoorn and P. A. Bobbert, *High-energy acceptor states enhance exciton transfer between metal-organic phosphorescent dyes*, to be submitted.

4. S. P. Schießl, X. de Vries, M. Rother, A. Massé, M. Brohmann, P. A. Bobbert and J. Zaumseil, *Modeling carrier density dependent charge transport in semiconducting carbon nanotube networks*, Phys. Rev. Mater. 1, 1–13 (2017).

5. G. Simone, D. Di Carlo Rasi, X. de Vries, G. H. L. Heintges, S. C. J. Meskers, R. A. J. Janssen and G.H. Gelinck, *Near-infrared tandem organic photodiodes for future application in artificial retinal implants*, Adv. Mater. 30, 1–7 (2018).

6. A. Ligthart, X. de Vries, L. Zhang, M. C. W. M. Pols, P. A. Bobbert, H. van Eersel and R. Coehoorn, *Effect of Triplet Confinement on Triplet–Triplet Annihilation in Organic Phosphorescent Host–Guest Systems*, Adv. Funct. Mater. 28, 1–10 (2018).

7. R. E. M. Willems, C. H. L. Weijtens, X. de Vries, R. Coehoorn and R. A. J. Janssen, *Relating Frontier Orbital Energies from Voltammetry and Photoelectron Spectroscopy to the Open-Circuit Voltage of Organic Solar Cells*, Adv. Energy Mater. 9, (2019).

Summary

The incorporation of organic materials in opto-electronic devices provides almost limitless adaptability of molecular and device structure in order to enhance existing and create novel devices. In order to realize this, predictive models have to be developed starting from first-principle theories to understand the complex charge and exciton dynamics from the molecular scale. Up to now, such models have relied on transfer theories that include the vibrational and excited state properties of the molecules in a simplified way. In this thesis we take new steps in the field of predictive modelling by including many more molecular details in the transfer theories and applying them to realistic predictive models including the disordered nature of the organic materials.

The methods developed in this thesis include the calculation of the necessary components of the charge and exciton transfer rates, like the transfer integrals, energy levels, and vibronic couplings. Additionally, methods for calculating the disorder in the energy levels and transfer integrals are introduced. The charge and exciton transport properties can then be found using 3D Master Equation and Monte Carlo simulations.

The first result of this thesis is a model for the charge transport in three common OLED host materials. The charge transfer rates used in this model are developed starting from Fermi's Golden Rule (FGR) including the vibronic coupling of all the intramolecular vibrations (vibrons) in a quantum mechanical way. This results in transfer rates which are significantly different from the commonly used Marcus and Miller-Abrahams rates. We see that due to the disorder present in these materials the strong differences in the transfer rates average out, and the charge mobilities obtained using the FGR transfer rate are similar to those from the Marcus and Miller-Abrahams rates.

The second result is a model for exciton transport between common phosphorescent emitters. The role of the Dexter and Förster mechanisms for exciton transfer are investigated. We find that at concentrations commonly used in phosphorescent OLEDs the Förster mechanism is mainly responsible for the exciton transfer in these materials. Additionally, we include the vibronic coupling from all the intramolecular vibrations. We find that this is important in correctly predicting the diffusion lengths of the excitons, since the Marcus theory significantly underestimates the exciton diffusion length.

The third and final result is an investigation of exothermic exciton transfer between phosphorescent dyes, e.g. transfer from a blue to a green dye. We apply the

previously developed FGR rate to calculate the Förster radii between more than 80 different donor-acceptor pairs of phosphorescent emitters. Small exothermicity partially overcomes the spectral Stokes shift, enhancing the Förster radius. At large exothermicities the Förster radius is strongly enhanced due to transfer to multiple energetically higher lying excited states of the acceptor molecules.

The findings presented in this thesis improve our understanding of the role of molecular vibrations in the charge and exciton transfer process applied to realistic molecules and systems. Using this understanding we take the first steps in predictively modelling the exciton transfer in the emissive layers of OLED devices. In general, the methods in this thesis can be used to select molecules with favorable properties in order to improve organic opto-electronic devices and explore new device architectures.

Curriculum Vitae

Xander de Vries was born in Tilburg on April 9, 1990. After the completion of secondary school at the VWO level he studied chemistry at the Radboud University in Nijmegen. In his bachelor internship he worked at the Department of Theoretical Chemistry were he performed Hartree-Fock and Density Functional Theory calculations on molecular crystals. In his master, he worked on Kinetic Monte Carlo simulations of interstellar ice formation at the Department of Theoretical Chemistry in Nijmegen. In a second master internship he went the the California Institute of Technology to study interstellar ice grain chemistry using terahertz spectroscopy at the Blake research group. In July 2015, he started his PhD at the Eindhoven University of Technology. He worked together with a consortium of research groups and companies in the EU to study the degradation of OLEDs. During his work he focused on connecting the molecular scale to the device scale to understand the role of molecular vibrations in the charge and exciton transport in OLEDs. He presented his work at many international conferences and workshops, among which the OP2017 conference in Quebec where he received a poster prize.

Dankwoord

Ik wil graag iedereen bedanken die bijgedragen heeft aan dit werk. Laat ik beginnen bij mijn begeleiders Peter en Reinder. **Peter**, je hebt me de laatste 4 jaar enorm veel geleerd. Jouw oog voor detail heeft dit werk naar een hoger niveau gebracht. Je bent een fijne begeleider die me de ruimte heeft gegeven om zelf mijn onderzoek te ontdekken, maar je hebt ook op de juiste momenten bijgestuurd. **Reinder**, ik waardeer de tijd die je de afgelopen jaren met me hebt besteed om de vele puzzels die we onderweg tegenkwamen op te lossen. Ik kon vaak met half uitgedachte vragen en ideeën bij jou komen, om er dan samen een scherpe vraagstelling van te maken. Jouw enthousiasme en doorzettingsvermogen heeft me geleerd hoe je stapje voor stapje ingewikkelde vraagstukken kunt oplossen.

I would also like to thank my defense committee members for taking the time to read my thesis, thank you, prof. Walker, prof. Gómez Rivas, dr. Kokkelmans and Prof. Wenzel.

Pascal and Wolfgang, I would like to thank you for the contributions you made to this work in the past few years. **Pascal**, I really appreciate the time and effort you put into the calculations, these represent a significant part of the results presented in our papers and this thesis. I also appreciate the continuous welcome feedback on the papers that we wrote. Your critical questions definitely improved the clarity of the papers and my thesis. **Wolfgang**, thank you for your suggestions at the many meetings that we had and for your contributions to the papers.

Ik wil graag alle collega's van de M2N groep bedanken voor de gezellige BBQs, sportdagen, groepsuitjes en meerkampen. Naast deze activiteiten heb ik ook plezier gehad van de vaste koffie en lunch momenten; om 10u koffie, 12u lunch en om 15u koffie/thee. Zo'n vast schema klinkt misschien een beetje knullig, maar ik vind het een heerlijk ritueeltje. In de eerst 3 jaar werden deze vaste tijden gehandhaafd door de 90 jarige **Rein Rumphorst**. Iets voor 10u klopte hij dan aan om vervolgens met ongeëvenaarde precisie, tot op de seconde nauwkeurig, aan te geven wanneer de koffie klaar was. Als ik dan te diep verzonken zat in mijn werk dan kwam hij vaak nog voor een tweede ronde langs.

Vaste koffiegenoten waren ook technici Wijnand en Marco. **Wijnand**, bedankt voor al je hulp bij computerproblemen, en het fungeren als uitlaatklep voor mijn frustraties over het computercluster. **Marco**, bedankt voor het organiseren van de BBQs en de gezelligheid aan de koffie- en lunchtafel.

Ik wil ook graag Aart, Niels, Robbert, Christ en Kees bedanken voor de goede gesprekken, discussies, start-up pitches en meligheid aan de koffietafel. De algehele aanwezige koppigheid zorgde voor discussies waarin de aangedragen argumenten naarmate de discussie vorderde steeds minder wetenschappelijke verantwoording bevatte, maar dat was toegestaan aan de koffietafel. **Niels**, bedankt voor je hulp bij werk en niet-werk gerelateerde zaken, je bent een onuitputtelijke bron van (technische) kennis en hebt me het laatste jaar zeker geholpen bij een aantal computerproblemen. **Robbert**, ik waardeerde het iedere keer dat je mij betrok bij je fysische vraagstukken. Je hebt een sterke wetenschappelijke instelling met een goede bullshitradar. Vaak wisten we in onze gesprekken tot de grenzen van onze kennis te komen, daardoor werd het duidelijk welke onderwerpen we nog moesten bestuderen. **Christ**, heel erg bedankt voor je bijdragen bij de group meetings en brainstorms. **Kees**, bedankt voor de goede gesprekken over van alles en nog wat, en de suggesties op het wetenschappelijk vlak.

Daarnaast wil ik onze collega's bij scheikunde bedanken voor de gezelligheid tijdens de groepsuitjes en andere activiteiten. **René** en **Stefan** heel erg bedankt voor jullie feedback tijdens de group meetings. René, bedankt voor dat je me hebt betrokken bij je onderwijstaken, ik vond dat erg leuk.

Ook wil ik **Margot**, onze secretaresse, heel erg bedanken. Hoe jij iedereen in de gaten houd en op de hoogte bent van alles wat speelt in de groep is heel bijzonder. Je kwam vaak langs voor een gezellig praatje, en ik kon ook altijd mijn verhaal bij jou kwijt. Je bent zorgzaam voor alle nieuwe studenten en zorgt dat iedereen betrokken wordt bij de activiteiten.

I would also like to thank the Simbeyond team. **Siebe** and **Harm**, you started right around the time that I did, and I have seen you grow with much interest. It is inspiring to work in the neighborhood of people that turn scientific knowledge into something useful, and are able to bring this to the market. I was able to learn a lot from seeing this process happen during my PhD. **Stefano**, **Marc** and **Christoph**, thank you for the enthusiasm and interesting discussions about the technical details of my work, and thank you for letting me be involved in the technical problems that you work on.

I also thank the old colleagues from who I have learned a lot, **Le**, **Andrea**, **Feilong** and **Vikas**, thank you.

Ook bedankt alle studenten die onze groep de laatste jaren hebben gepasseerd en voor veel gezelligheid hebben gezorgd, **Geert**, **Mike**, **Wesly**, **Sanne**, **Tim**, **Teun** en nog veel meer.

Aart en Giulio, van alle promovendi ken ik jullie al het langst en ik ben daarom ook verheugd dat jullie mijn paranimfen willen zijn. Ik heb enorm genoten van onze conferentiebezoeken, die soms ook wel voelden als culinaire tripjes, alhoewel we de laatste keer alledrie een belangrijke bijdrage hadden aan het wetenschappelijk programma. Ik heb jullie net als mezelf zien groeien in jullie rol als wetenschappers.

Giulio, I really enjoyed the work we did on puzzling through the operating principles of your devices. I was honored to be involved in your project. I enjoyed your

updates on the NBA standings, your cooking talent, and your heated discussions with Aart.

Aart, je bent vanaf het begin een belangrijke sociale bindende factor in onze groep geweest. Op jouw initiatief gingen we vaak naar borrels, activiteiten en werden de kwartaalverslagen op tijd ingeleverd. Het was een plezier om met jou de vele MOSTOPHOS meetings en conferenties te bezoeken. Ook bedankt voor je altijd welkome feedback op mijn werk.

Ik zou ook graag mijn vrienden uit Nijmegen en Tilburg (en omstreken) bedanken. **Tim**, **Maarten**, **Roel**, **Daniel**, **Maurits**, **Jonne** en **Maurice** bedankt voor de interesse in mijn werk en welkome afleiding op de last-minute geplande etentjes en weekenden. **Rick**, **Dorine**, **Pjotr**, **Michiel** en **Ronald**, voor de reünie van ons Turkije avontuur zo nu en dan. **Thomas**, **Joep**, **Hidde**, **Joris** en **Maarten**, voor de entropische weekendjes. **Ludo** en **Michelle**, bedankt voor jullie interesse in mijn werk en de goede gesprekken die we daarover hadden.

Maarten en Joris, ik heb genoten van de 2 jaar waarin we samen het huis op de Leenherenstraat bewoonden. Het was soms een studentikoze bende, maar ook wel fijn om op deze manier de overstap naar het werkende leven te maken.

Tim, **Michael** and **Sophie** thanks for the great time we had during our weekend trips. I really enjoyed the conversations, food and hikes that we shared together.

Pap (**Piet**), mam (**Tineke**), **Ruth** en **Sjoerd**, bedankt voor jullie interesse en steun de afgelopen 4 jaar. De gesprekken met jullie hielpen vaak om zaken te relativeren of om een nieuw perspectief te brengen. **Ans** en **Luuk**, bedankt voor jullie altijd aanwezige interesse in mijn studie en werk.

Lieve **Maayke**, bedankt voor je heerlijke enthousiasme als ik weer eens vermoeid of verslagen thuiskwam. Ik denk dat ik de keren dat ik niet met een glimlach door jou werd begroet op één hand kan tellen. Ik vond het leuk om je af en toe wat te vertellen over waar ik op die dag aan gepuzzeld had, en met wat kritische vragen van jouw kant hielp me dat ook vaak om nog een onopgeloste stuk van de puzzel in te vullen.

Xander